NASA Technical Memorandum 78446

Water-Tunnel Experiments on an Oscillating Airfoil at Re = 21,000

Kenneth W. McAlister and Lawrence W. Carr

MARCH 1978

NASA

NASA Technical Memorandum 78446

Water-Tunnel Experiments on an Oscillating Airfoil at Re = 21,000

Kenneth W. McAlister and Lawrence W. Carr
Aeromechanics Laboratory
U.S. Army R&T Laboratories {AVRADCOM}
Ames Research Center
Moffett Field, California

NASA
National Aeronautics
and Space Administration

Scientific and Technical
Information Office

1978

TABLE OF CONTENTS

SYMBOLS

c	chord of airfoil, m
k	reduced frequency, $\omega c/2U_\infty$
L	characteristic length, m
n	vortex shedding frequency, Hz
Re	Reynolds number, $U_\infty c/\nu$
t	time, sec
U_∞	free-stream velocity, m/sec
x	distance along chord from leading edge, m
α	airfoil incidence
λ	distance between like vortices, m
ν	kinematic viscosity, m^2/sec
Ω	electrical resistance, ohms
ω	rotational frequency, rad/sec

WATER-TUNNEL EXPERIMENTS ON AN OSCILLATING AIRFOIL AT Re = 21,000

Kenneth W. McAlister and Lawrence W. Carr

Ames Research Center
and
Aeromechanics Laboratory
U.S. Army Aviation R&D Command

SUMMARY

Flow visualization experiments were performed in a water tunnel on a modified NACA 0012 airfoil undergoing large-amplitude harmonic oscillations in pitch. The motion of the airfoil was governed by $\alpha = 10° + 10° \sin \omega t$ at $k = 0.25$. Hydrogen bubbles were used to (1) create a conveniently striated and well-preserved set of inviscid flow markers; and (2) to expose the succession of events occurring within the viscous domain during the onset of dynamic stall.

Unsteady effects are shown to have an important influence on the progression of flow reversal along the airfoil surface prior to stall. More importantly, a region of reversed flow underlying a free-shear layer is found to momentarily exist over the entire upper surface without any appreciable disturbance of the viscous-inviscid boundary. A flow protuberance, which is not the classical laminar separation bubble that occurs at higher Reynolds numbers, is observed to develop near the leading edge, while minor vortices evolve from an expanding instability of the free-shear layer over the rear portion of the airfoil. The complete breakdown of this shear layer culminates in the successive formation of two dominant vortices.

INTRODUCTION

It is now well known that a dynamic increase in airfoil incidence, that carries it beyond the static-stall angle, can result in an increase in lift without any detectable change in the lift-curve slope. However, the boundary layer eventually breaks down, and if the overshoot of static stall conditions is sufficiently large, at least one vortex develops along the forward portion of the airfoil. As this vortex moves down the airfoil, the accompanying shift in the center of pressure causes a significant change in the pitching moment while the vortex induces a further increase in lift. The lift reaches a maximum while the vortex is moving over the latter half of the airfoil. Finally, a maximum in pitching moment occurs before the vortex reaches the trailing edge of the airfoil, thus marking the end of the period of stall onset and the beginning of deep stall. The precipitating mechanism of this sequence of events has stimulated much interest, especially among those concerned with the performance of lifting bodies that are required to oscillate in pitch through the stall regime.

While certain details of the stall process may be dependent on the airfoil geometry and the particular flow environment (e.g., pitch rate and Reynolds number), the general characteristics of the stall vortex are believed to be qualitatively invariant. An important step toward a better understanding of dynamic stall would therefore be to examine the collapse of the boundary layer and the initial development of this vortex under conditions amenable to more definitive flow visualizations than are normally possible in air. Although typically limited to lower Reynolds number experiments, a particularly attractive alternative medium is water, since it submits to the production of minute hydrogen bubbles for use as flow markers. Provided the Reynolds number can be made sufficiently low so that a completely laminar flow is produced around the oscillating airfoil, an additional benefit to be realized from this experiment will be the opportunity to compare with calculations (as they become available) based on the Navier-Stokes equations.

The purpose of this study, therefore, was to develop the application and documentation of hydrogen bubble flow visualization for an airfoil undergoing large-amplitude pitch oscillations and to examine the detailed events comprising the onset of dynamic stall.

DESCRIPTION OF FACILITY

The following sections describe the Aeromechanics Laboratory (AVRADCOM) water-tunnel facility and the various supportive apparatus used for producing flow visualizations and for recording these results photographically. Specific construction details are presented more completely in reference 1.

The Water Tunnel

The tunnel is a closed-circuit design. It contains approximately 4000 liters of water, and with the exception of the fiberglass contraction section and the plexiglas test section windows, is constructed from type 304 stainless steel (fig. 1). The tunnel passages are predominantly circular, except for the rectangular test section which measures 0.2 m (width) × 0.3 m (height) × 1.0 m (length). The transition from circular to rectangular cross section takes place in the contraction and diffuser sections adjoining the test section.

The water is driven by a three-bladed impeller powered by a dc motor using a silicon-controlled rectifier. The velocity which can be attained in the test section is continuously variable from 0-6 m/sec. Prior to entering the 10:1 contraction, the flow is straightened by two sets of honeycomb, and the turbulence is reduced by four sections of screening. Two large storage tanks (fig. 1) are used for dissolving fresh chemicals before filling the tunnel and for holding that portion of the water withdrawn from the tunnel when making model changes. Whenever water is pumped back into the tunnel, it must first pass through a filter system designed to remove contaminates down to 5 μm (continuous filtration is also possible while the tunnel is in operation).

Model Oscillation Mechanism

The sinusoidal pitching motion of the airfoil is accomplished by a flywheel, connecting rod, and rack and gear mechanism (fig. 2) which function to transform the circular motion first to reciprocating, and then to airfoil pitch oscillations. The mean angle of oscillation is controlled by the length of the connecting rod while the amplitude is governed by the radial station on the flywheel at which the rod is connected. This combination of adjustments provides for pitching amplitudes up to 20° about a continuously variable mean angle that also ranges from 0°-20°.

The flywheel is driven by a dc motor through a belt and pulley system, and the speed is governed by a silicon-controlled rectifier. Continuously variable oscillation frequencies from 0-10 Hz can be obtained.

Degassing

Under atmospheric conditions, the amount of air dissolved in water is generally found to be about 2% by volume (ref. 2). This air remains in solution until drawn out by cavitation to form a lingering air bubble of detectable size. Typical low-pressure sources responsible for cavitation include the impeller, turning vanes, points of tunnel-wall separation, and the leading edge of a lifting airfoil. The presence of cavitation-induced air bubbles represents a serious limitation on the maximum usable speed in a test program since air bubbles can severely interfere with the viewing of the smaller bubbles which are intentionally generated during flow visualization studies.

The problem can be alleviated, however, by subjecting the water in the tunnel to a vacuum and extracting a majority of the dissolved air. This was accomplished with a series of three polypropylene venturi tubes used as aspirators. An external source of water was passed through each venturi at a rate that produced a 0.6-atm vacuum at each throat. The venturi throats were joined by a common tube that was attached to the plexiglas air dome on top of the tunnel (fig. 1). Degassing was normally only necessary with each initial filling of the tunnel. Once the air had been removed, the water could later be transferred to the holding tanks (while making model changes) and returned to the tunnel with negligible reingestion of air by maintaining a nominal height of water above all transfer points.

Pressurization

The water tunnel was designed to withstand a differential pressure of 1 atm. The tunnel is pressurized using a regulated source of compressed air that is connected by tubing to the air dome on top of the tunnel. This increase of pressure in the water reduces the size of all the bubbles that are formed during a test, whether they are due to cavitation or to the gases which are produced during electrolysis.

Since it is not practical to degas the water completely, a small amount of air will always remain in solution and can pose a problem during high Reynolds number tests. When under pressure, however, the air which coalesces at the points of cavitation to form detectable bubbles will be reduced in volume and will therefore be less visible. The benefits of pressurization are also significant in low Reynolds number tests. Since the density of the gas bubbles that are produced during electrolysis is increased, buoyancy forces are decreased. This is important since it improves the likelihood that the path of an observed bubble will represent that of the fluid element which it displaces.

The effect of increased pressure on bubble buoyancy was qualitatively examined on the basis of flow visualization. This was accomplished by orienting a symmetric airfoil at zero incidence in a field of bubbles representing the predominantly inviscid domain (fig. 3). Although the camera angle slightly favored the upper surface of the airfoil, it is clearly evident that the boundary layers on the upper and lower surfaces are more nearly equal in the pressurized case. Without pressurization, the bubbles moving over the upper surface falsely indicate a thicker viscous domain. Notice that because these bubbles are also more distant from the surface, fewer are entrained into the upper boundary layer and wake, thereby causing the clockwise vortices to be under-supplied, and hence less visible.

Since the flow is more accurately represented by the bubbles when the water is pressurized, the results presented in this study are those obtained with the tunnel pressurized at 1 atm. It should be noted that while the error due to buoyancy cannot be completely removed by increasing the density of the bubbles, the error is considered to be of little significance during visualizations of unsteady flows where dynamic forces are dominant.

Bubble Generation

By placing two electrodes in an electrolytic aqueous solution and applying a dc voltage between them, gaseous bubbles are formed at each electrode. This chemical process (electrolysis) is described by the following reaction formulas:

$$2\ H_2O + 2\ e \rightarrow H_2 + 2\ OH^- \qquad \text{(cathode)}$$

$$2\ H_2O - 2\ e \rightarrow O_2 + 4\ H^+ + 4\ e \qquad \text{(anode)}$$

Since the hydrogen bubbles formed at the cathode during this reaction are smaller than the oxygen bubbles which are simultaneously formed at the anode, the cathode was placed in the field of interest and its size carefully tailored to yield the flow visualization required. While the cathode may take the form of a narrow wire stretched across the flow field, it was found more convenient to maximize the anode surface area since it must erode as electrons are released. Hence, the wire identified as being the anode in figure 4 was later removed, but the suspension bolts were retained as electrodes by electrically connecting them outside of the test section.

The size of the bubbles produced depends on the polarity as well as the width or diameter of the electrode. Bubble size also depends on the electrolytic conductivity of the solution and the electrical potential that is applied between the electrodes (ref. 3). Although common water supplies generally contain enough impurities to provide a current path, the conductivity of the water can be significantly improved with the addition of sodium sulfate (normally less than 2.5% by weight is sufficient). Once a current path is established, the electrical resistance of the participating portion of this solution is reduced by several orders of magnitude (reductions from 20,000 Ω to 20 Ω are not uncommon).

To expose the behavior of the inviscid flow field around the airfoil, a wire (serving as the cathode) was stretched across the test section and orientated normal to the direction of flow. Although both platinum and stainless steel are good chemically-noncorroding materials, stainless steel was selected because of its superior tensile strength. A 0.45-mm stainless steel wire was used in the present experiment in order to obtain a particular frequency of Kármán vortex shedding from the wire. Care must be taken here since both an increase in wire diameter and a reduction in free-stream velocity will increase the error due to buoyancy. It is also recommended that the wire be located at least 70 wire diameters ahead of the model in order that the bubbles have sufficient time to reach free-stream velocity (ref. 3).

Model

An electrically nonconducting model was cast from 5309-MOS fiber resin with a stainless steel spar passing through the quarter-chord axis. The profile was that of the NACA 0012 airfoil with a modified leading edge. This modification consisted of a 0.01-c extension of the leading edge to permit a reduction of the nose radius from 0.016 c to 0.004 c (see insert, fig. 5). The planform of the model measured 10 cm in chord and 21 cm in span.

Electrodes were placed at nine chordwise locations along the upper surface of the model (fig. 5). These electrodes consisted of 0.05-mm-thick platinum sheets aligned with the span of the model and oriented normal to the direction of flow. These sheets were embedded in the model so that a single exposed edge (13 mm long) served as the active part of each electrode. Prior to pouring the resin, a No. 30 insulated wire was soldered to each electrode and the ensemble of wires passed out of the model through the center of the spar. By using another electrode located downstream of the model as the anode, the wiring arrangement described above allowed each model electrode to function as a cathode and be independently activated at an external control panel.

The model was supported on one end by a pin that was pressed into the spar except for a short length which protruded into the front test-section window and acted as a pivot. The opposite end of the model was supported by a pivoting clamp that is attached to the short section of spar extending beyond the model and into the rear test-section window.

Lighting

The bubbles were illuminated by a narrow sheet of light (approximately 13 mm wide and 30 cm long) directed through the upper test-section window (fig. 6). Two baffles were used to control the width of the light as well as to affect a degree of parallelism in the light beam passing into the test section. The path of the light was canted 10° from the plane of the bubbles in order to provide a component of back lighting without compromising the required vertical spread of illumination above the model.

Both continuous and flash sources of light were produced over the needed 30 cm length. Continuous lighting was provided by two lamps totaling 1000 W. These lamps were located outside the optical housing so that the infrared content of the light spectrum could be conveniently removed by a row of 6 mm thick heat-absorbing glass plates. This heat was in turn convected away by a high-velocity stream of air directed at the absorbing glasses. Once inside the optical housing, the light was turned 90° by a mirror which could be retracted when this mode of lighting was no longer required. Continuous lighting was used for general viewing, for high-speed movies and for long exposures (normally 1/60 sec) with a single-frame camera.

When an instantaneous visualization of the flow field was needed at a given phase angle of model oscillation, the mirror was retracted and a 30-cm-long xenon strobe tube was activated. Connected across the tube is a 2000 V (max.) supply, capable of delivering up to 8 kW. A flash is produced each time a 20,000-V pulse is applied to the "tickler" wire that is coiled around the tube. The pulse can either be executed manually or it can be automatically synchronized at a preset phase angle.

Photography

Two types of camera systems were used to document the results of various flow visualizations. They provided the capability of obtaining (1) single exposures for both frozen element and path line studies; and (2) high-speed movies for detailed motion analysis.

The first system consisted of an automatic 70-mm film magazine, a bellows type focusing body, and a high light gathering 240-mm lens (f4.5 min.) coupled with an electronically controlled aperture and shutter (1/60 sec min.). This composite camera was mounted on a rigid 9-cm diameter pipe so that the film plane was located a nominal distance of 152 cm from the center of the test section (fig. 7). This combination of lens and film plane-to-subject distance was found to offer the best compromise between image size, depth of field and perspective distortion. The black and white film used in this camera was a high-speed medium-grain roll film which yields normal density exposures at f8 when processed in a high-contrast developer at 85° F and at a machine rate of 1.5 m/sec.

A photograph was taken with this camera of an equidistant grid that was scribed on a plexiglass plate and placed in the test section where the sheet of bubbles would be illuminated. Measurements of the grid spacing on the resulting film showed that no significant distortion was present. A portion of this grid has been reproduced in figure 5 where it can be seen to intersect the midspan of the model as well as the trailing edge. Since the grid spacing was based on the slightly shorter NACA 0012 profile, the left-most grid line does not intersect the leading edge of the modified airfoil. Note that a significant amount of perspective distortion does occur as the plane of interest approaches the camera lens. This causes the near end of the model to not only extend beyond the leading and trailing edges, but also to overlay the critical region close to the upper surface. This visual obstacle was overcome by simply elevating the camera slightly. Based on this preliminary study, it was concluded that photographs of the flow field could be analyzed directly without applying any correction for perspective distortion.

The second system was a high-speed, precision motion picture camera capable of indexing 16-mm film at 500 frames/sec (using positive pin registration) with ±1.5% speed stability. This camera was mounted on a rotatable arm which allowed the lens axis to be coaxially positioned in front of the lens of the first camera system. The resulting distance between the film plane and the center of the test section was nominally 86 cm. At this focusing range a 50-mm lens was found to cover approximately 21 cm, or 1.5 lengths using the present airfoil. Preliminary tests indicated that a minimum setting of 64 frames/sec would be required for motion analysis of various flow phenomena. Using a 160° shutter (equivalent to 1/140 sec at 64 frames/sec) and requiring that the aperture be opened no larger than f2.8, to maintain a reasonable depth of field, meant that 400 ASA film would have to be used because of its high sensitivity to light. A less sensitive color film was also used, and found to require an aperture setting of f1.4 as well as a one-stop push during development.

Instrumentation

The controls for selecting the tunnel dynamic pressure, the frequency of model oscillation, the mode and level of bubble generation, and the voltage level to be applied to the strobe are fundamental to the operation of the facility. In addition to these, certain electronics have been provided for synchronizing the cameras to the motion of the model.

Two discs are geared to the flywheel axis and are used to close photocell circuits at once/rev and 180/rev intervals. The once/rev closure either automatically produces a pulse at this repetitive interval or is contingent on a preset switch being depressed. In either case, the generated pulse serves to energize the strobe or to release the camera shutter. The phase angle is continuously variable from 0°-360° of azimuth (hereinafter used to denote the value of ωt in degrees) and is selected by rotating a dial attached to the synchronizing disc (fig. 7). The dial setting is transformed to a 3-digit display (and projected through the rear test-section window, see fig. 4) using a voltage divider and an analog-to-digital converter. The intensity of the display is variable to be compatible with various film exposure requirements.

The 180/rev closure provides a pulse which can be sampled over a fixed period of time to obtain the frequency at which the model is oscillating. This signal was also used to generate a numerical display of the model phase angle at an interval of 2° of azimuth. The image of this display was redirected through a series of mirrors so that the cumulative distance to the film plane of the high-speed movie camera placed it within the critical depth of field.

DESCRIPTION OF EXPERIMENT

The purpose of this study was to demonstrate the flow visualization potential of hydrogen bubbles in the water-tunnel facility at a sufficiently low Reynolds number to produce laminar flow on an airfoil. In addition, the detailed features of dynamic stall, as it develops on an airfoil undergoing large amplitude oscillations in pitch, were to be analyzed using various flow documentation techniques.

The minimum speed at which the tunnel can be operated is limited by the increasing error in bubble trajectory caused by buoyancy forces. These forces are directly related to bubble size, which are in turn dependent on the size of the generating electrode. This trend suggested that the smallest possible diameter wire be selected for the free-stream electrode; however, a second factor needed to be considered. The frequency and clarity of the natural vortex shedding from the wire are also dependent on wire size. Under certain conditions, this shedding phenomenon was found to produce a conveniently striated and well-preserved pattern in the sheet of bubbles being generated at the wire. Guided by both considerations, a wire diameter of 0.45 mm and a tunnel speed of 0.2 m/sec were chosen for this test, resulting in a Reynolds number of 21,000 based on airfoil chord.

The airfoil was pitched about its quarter-chord axis at a frequency of 0.16 Hz (nondimensional frequency $\omega c/2U_\infty = 0.25$, corresponding to the environment existing during retreating-blade stall on helicopter rotors). The choice of this frequency permits qualitative comparisons with recent wind-tunnel results on a similar airfoil (ref. 4) as well as with related water-tunnel studies by Werlé (ref. 5) and theoretical calculations by Mehta (ref. 6) for the NACA 0012 airfoil.

Since the static-stall angle for the airfoil under study was 10°, a pitch schedule described by $\alpha = 10° + 10° \sin \omega t$ was imposed. The large 10° pitch amplitude was chosen because it assures the formation of a fully developed stall vortex (one that occurs during the pitchup) rather than one that is forced at the top of the cycle by a change in the direction of pitch. This mean angle and amplitude schedule corresponds to the oscillatory values attained in the impulsive start studies of Werlé and Mehta.

Two types of hydrogen bubble flow patterns have been produced in this test: (1) bubbles generated at the electrodes on the model surface; these are then transported downstream by fluid within the boundary layer and wake (thus primarily exposing the viscous domain); and (2) bubbles generated as a sheet from an upstream electrode; these then pass around the airfoil without penetrating the boundary layer at the stagnation point and without any appreciable entrainment until reaching the wake (thus primarily exposing the inviscid domain). Photographs showing the viscous domain were taken with continuous lighting and a shutter speed of 1/60 sec, while those showing the inviscid flow field were taken with a strobe light and open shutter. The camera lens was set at f8 for all exposures. The dc potential applied to the free-stream electrode was 19 V. The potential applied to the model electrodes was either 27 V, when all stations were activated, or 8 V when activated separately. The resulting current in these three cases was 1.3 A, 0.2 A, and 0.04 A, respectively.

DISCUSSION OF RESULTS

Fixed Incidence

Even with the airfoil held at a fixed incidence, the flow field, strictly speaking, was not observed to be completely steady. At zero incidence, for example, the vorticity that was shed into the wake from the upper and lower surfaces ordered itself into a periodic vortex pattern (fig. 8). This pattern is strongly reminiscent of Kármán vortex shedding, thus suggesting that the boundary layer was laminar on the airfoil. The vortices that are shed into the wake appear to move close to the free-stream velocity and at a shedding frequency of 7 pairs/sec.

The progression of the point of separation was studied by observing the bubbles that were produced at the individual chord locations. These bubbles show that flow separation progresses smoothly forward as the airfoil incidence is increased (fig. 9). The fact that the flow began to separate at such low values of incidence is judged to be further evidence that the boundary layer was laminar.

The reason for emphasizing that the entire boundary layer was laminar is that it precludes, by definition, the possibility that a classical high Reynolds number laminar separation bubble was present. This type of bubble is said to exist when a laminar boundary layer separates (usually near the leading edge), undergoes transition, and then reattaches to the surface as a turbulent boundary layer. Since the flow behaved as though all of the boundary layer were laminar, it was concluded that a separation bubble (one that closes through turbulent reattachment) does not occur for this airfoil under the conditions of this test. The absence of this type of bubble can also be inferred from the work of Gault (ref. 7), where it is reported that a necessary condition for the formation of such a bubble is a minimum Reynolds number (based on the local displacement thickness) of 500. In the present experiment, a conservative estimate built upon the appearance of the boundary layer over the first 5% of the chord (fig. 8) gives a value that is an order of magnitude smaller than this critical Reynolds number.

Dynamic Behavior

The laminar state of the boundary-layer flow field argued above for the steady case can also be shown to persist in the dynamic case ($\alpha = 10° + 10° \sin \omega t$ and $k = 0.25$). By comparing the wake patterns in figure 10 that were observed under both steady and dynamic conditions (shown during pitchup) at three incidence angles ($\alpha = 3°$, $4°$, and $5°$), it is readily clear that the laminar vortex pattern which appears in the steady case also occurs in the wake of an oscillating airfoil. In addition, it is important to note that the steady and dynamic wakes are strikingly similar in that the distance between consecutive vortices of the same sense appears to be unchanged ($\lambda/c = 0.28$), yet dissimilar in that the counter-clockwise vortices in the dynamic cases are predominant. This biased strengthening of the existing vortex pattern shows that the dynamic increase in lift can be detected in the wake structure prior to stall when the flow on the airfoil is laminar. A qualitatively similar distortion of the vortex pattern found in the wake of a laminar airfoil experiencing an impulsive increase in incidence has also been reported by Brown (ref. 8).

As a final affirmation of the laminar state of the boundary layer, note the bubbles generated at the various chord locations (figs. 10, electrodes 3-8). In the dynamic cases, these bubbles not only map out generally well-behaved paths over the airfoil, but also continue to move in an organized fashion well into the wake. In the steady cases, the bubbles are again observed to be quite ordered, continuing beyond the point of separation and into the formation of the first vortex. As the incidence increases, vortices appear to be forming at progressively earlier stations on the airfoil, as well as degenerating more rapidly. This decay in apparent vortex structure (note especially fig. 10(c) downstream of 75% chord) is either caused by turbulence or is due to the growing importance of three-dimensional effects within the expanding region of separated flow.

In addition to these interesting overall features of the flow field, it is perhaps most significant to note the influence of airfoil oscillation on the direction of boundary-layer flow near the surface. At each incidence, the first electrode selected in the steady sequence (figs. 10) identifies the location of incipient flow reversal, while the succeeding three electrodes show the movement of fluid past those stations in a fully separated region. In contrast to these flow patterns, the corresponding sequence of dynamic scenes not only indicate a thinner boundary layer, but also show that flow reversal at these stations has not yet taken place.

The most remarkable point about dynamic flow reversal (examined in detail later) is that it occurs without any detectable change in boundary-layer thickness. To ascertain the precise progression of flow reversal on the oscillating airfoil, an analysis was made of a high-speed motion film. This study revealed that flow reversal was delayed over the entire airfoil (fig. 9), and that a maximum delay of 7° incidence occurred at 40% chord. Similar to the steady case, flow reversal proceeds from the trailing edge toward the leading edge; however, the dynamic progression of flow reversal is even more nonlinear, exhibiting a relatively slow rate of advance over the midsection of the airfoil.

Complete Cycle

Before discussing the details of dynamic stall, it is useful to examine the predominant flow characteristics as they develop during a complete cycle of airfoil oscillation. To accomplish this, the flow field was photographed at 24 equidistant increments of azimuth using hydrogen bubbles generated at both the free-stream electrode and at electrodes located on the model (figs. 11). The upper photograph (showing the predominantly inviscid flow field) was recorded using a strobe light; the lower photograph was recorded at 1/60 sec. Some caution is recommended when interpreting the relationship between various photographs in this sequence. Due to small flow irregularities entering the test section, the initiation of certain detailed events was observed to vary from one cycle to another, especially once the boundary-layer flow began to separate on the airfoil. Since each exposure in the series was obtained during a different cycle of oscillation, only the more dominant features, which were clearly invariant in their order of succession, will be emphasized in this section.

The series begins with the airfoil passing through minimum incidence $\omega t = 270°$ ($\alpha = 0°$). At this point, the boundary layer appears to be generally smooth and the wake region fairly regular over the initial half-chord length behind the airfoil. The flow field is not symmetrical because of unsteady lag effects from the downstroke. As the incidence increases to the static-stall angle $\omega t = 0°$ ($\alpha = 10°$), the boundary layer gradually thickens, and the orderliness of the vorticity in the wake now extends well beyond a chord length behind the airfoil.

By the time $\omega t = 15°$ ($\alpha = 12.6°$), a distinct flow protuberance appears near the leading edge and the outer viscous boundary becomes sinuous over the rear portion of the airfoil. The term protuberance is used to help the reader distinguish between the bubblelike distortion observed in the present experiment and the classical laminar separation bubble that is found at higher Reynolds numbers. At $\omega t = 30°$ ($\alpha = 15°$), a major distortion in the viscous-inviscid boundary occurs over most of the airfoil, strongly suggesting that a conventional boundary layer is no longer present (fig. 11(i)). It should be noted that the wake region is entirely organized, and will remain so for another 30° of azimuth (one chord length of free-stream travel). During this interval of time (between $\omega t = 30°$ and 60°), at least 2 vortexlike flow patterns develop; one near the midchord and the second near the leading edge of the airfoil. The midchord vortex moves down the airfoil at about 75% of the free-stream velocity; the leading-edge vortex, however, initially progresses more slowly while appearing to build in strength. By the time the midchord vortex has moved off the airfoil and into the wake ($\omega t = 60°$, $\alpha = 18.7°$), the leading-edge vortex has become clearly recognizable and can be seen to have moved about 25% of the way down the airfoil, leaving behind a significant accumulation of less active fluid. In the time of its residence as the sole vortex over the airfoil for the next 30° of azimuth, it moves along the surface at about 40% of the free-stream velocity. During this time, the bubble density in the vortex diminishes significantly. To some extent, this decrease in bubble density may be due to an increase in the size of the vortex along with a simultaneous decrease in the entrainment of new bubbles along its perimeter. More importantly, there is the possibility that three-dimensional effects have increased to the point of causing many of the bubbles to be convected out of the plane of illumination. In any case, the only statement that can be made with confidence about the vortex at this time is that at $\omega t = 105°$ ($\alpha = 19.7°$, downstroke), there is a strong upward movement away from the surface of the airfoil at about the 70% chord location.

By extrapolating along the last known trajectory of the vortex, there is evidence at $\omega t = 165°$ ($\alpha = 12.6°$) that this vortex has induced a three-dimensional character in the free stream just aft of the trailing edge and less than a chord length above the airfoil (fig. 11(r)). At $\omega t = 180°$ ($\alpha = 10°$), the nearly complete absence of bubbles in this region indicates that a strong spanwise component of flow is present (fig. 11(s)). Although the evidence contained in these photographs is admittedly limited, a careful analysis of the high-speed movies as well as a direct observation of this behavior during the experiment both reveal that a definite spanwise component does exist and that it accompanies an intense distortion of the shed vortex.

Since the aspect ratio of the model was small (less than 2), it is not known to what extent this vortex has become contaminated by the side walls. Regardless of its origin, the flow is known to be highly three-dimensional at this point; therefore, it is not recommended that serious comparisons with two-dimensional calculations be attempted during the period $\omega t = 150°\text{-}210°$.

The one remaining characteristic to be noted as the cycle of oscillation is completed is that the flow begins to reattach itself to the front of the airfoil upon returning to the static-stall angle (at $\omega t = 180°$). Reattachment then progresses quite rapidly toward the trailing edge as it displaces fully separated, but weak, regions of fluid remaining on the airfoil ($\omega t = 195°\text{-}240°$).

This completes the general discussion of the various gross events associated with large amplitude airfoil stall. It is interesting that at a much higher Reynolds number (Re = 2.5×10^6), a similar leading-edge vortex was observed (ref. 4). It also was observed to move slowly at first, appearing to be gathering strength, then increase in speed and finally move away from the surface as it approached the trailing edge. However, a midchord vortex was not observed for any airfoil configuration or reduced frequency during that experiment. At a lower Reynolds number (Re = 10,000), a 75%-chord vortex (in addition to the leading-edge vortex) was observed by Werlé as well as calculated by Mehta. It can therefore be speculated that when the midchord vortex (or one located farther aft) occurs, it is an outgrowth of the dynamic breakdown of the free-shear layer, while the leading-edge vortex (common to each case) is a universal symptom of dynamic stall.

With regard to the Kármán vortex street that is observed in many of the photographs presented, it is interesting that the Strouhal number, nL/U, calculated for this flow is 0.43 when the airfoil thickness is used as the characteristic length (the corresponding value for a circular cylinder is 0.2). Following the notion of Roshko (ref. 9) that a more generally formulated Strouhal number should reflect wake parameters, Paterson (ref. 10) has suggested that the proper characteristic length for streamlined bodies is the wake thickness at the trailing edge. Since (1) the vortex shedding frequency and the vortex street geometry appear to be the same in both the static (fig. 3) and dynamic (fig. 11(f)) cases; and (2) the width of the wake at the trailing edge of the airfoil appears to be approximately constant, the merit of this suggestion seems to be supported by the present results. Therefore, based on trailing-edge wake thickness, the resulting Strouhal number is approximately 0.46. While the usefulness of this formulation should be regarded as tenuous, the high value calculated (relative to that for the circular cylinder) is at least in keeping with the trend that higher shedding frequencies result from less bluff geometries.

Stall Onset

Now that the complete cycle of stall-related events have been placed in perspective, the detailed mechanisms comprising the onset of dynamic stall can be examined more effectively. It is during this critical phase that unsteady forces are known to cause a drastic and rapid adjustment of the fluid in the boundary layer that is unlike any flow development occurring in a steady environment.

This important period of the cycle, which includes the origin and growth of the dynamic stall vortex, is presented in detail in figures 12 at 4° intervals of azimuth. The sequence begins as the airfoil pitches through the static-stall angle ($\omega t = 0°$) and contains photographs taken of the flow field using (1) the free-stream electrode, (2) all of the model electrodes simultaneously; and (3) each of the 9 model electrodes individually activated. As discussed earlier, each exposure was made during a separate cycle of airfoil oscillation; therefore, some caution is advisable when relating any two scenes, even ones at the same phase angle.

When reviewing this sequence of photographs, it is interesting to follow the development of the viscous-inviscid boundary as the point of flow reversal moves toward the leading edge of the airfoil. It is remarkable that at $\omega t = 12°$, a free-shear layer, having a narrow region of reversed flow underneath, has occurred over the entire surface without any appreciable change in the viscous-inviscid boundary. As the airfoil incidence continues to increase during the next 50° of azimuth, the free-shear layer above the surface becomes unstable and a series of complex events are observed to unfold before the leading-edge vortex is fully developed.

As an aid to establishing the chronological order of these events, a study was made of the high-speed movies of several cycles of oscillation, during which each electrode was separately activated. Beginning at mean incidence ($\omega t = 0°$), these results show (fig. 13) that by the time the boundary-layer flow has reversed over the rear half of the airfoil, a portion of the resulting free-shear layer has become unstable (resembling the wavy character in fig. 12(a), electrode #3). These instabilities appear to mature into discrete traveling vortices of apparently short duration and of no obvious consequence. Once the flow has reversed up to the leading edge, a protuberance emerges over the first 6% of the surface as if to accommodate the sudden influx of fluid. The closure portion of the protuberance boundary, at this stage, is conjectured to be the result of the local unsteady pressure distribution which still supports an attached shear layer.

By $\omega t = 16°$, nearly the entire shear layer is either sinuous or broken up into minor vortices. During the next 10° of azimuth, the majority of the viscous region becomes discretized by the development of numerous clockwise vortices (note especially fig. 12(h)). The distance between these vortices appears to be half that between the clockwise vortices in the wake. An important exception to this regimented behavior is in the area of the protuberance. The flow in this region continues to have the same general shape, except that the downstream boundary is intermittently disrupted by the escape of small vortical bodies of fluid. As the larger, more identifiable vortices continue to move over the downstream surface of the airfoil, the upstream-most vortex appears to overtake and coalesce with the remaining ones (e.g., see figs. 12(i,j)), thus creating the first major (enduring) vortex to occur during the stall process. It was during the early part of this coalescence that a vortex could be clearly distinguished at midchord when all of the electrodes were active (upper part of fig. 12(h)); thus the midchord vortex that was identified in the previous section (the first major vortex to occur) actually originates near the quarter chord in an ensemble of vortices resulting from the shear wave instability.

This flow pattern progresses for another 25° of azimuth (to $\omega t = 50°$) with no detectable change in character. However, as the first major vortex leaves the trailing edge of the airfoil, the somewhat random production and shedding of small vortices from the leading-edge protuberance domain evolves into a distinctly unified vortical pattern (note figs. 14). This becomes the second major vortex to occur, and its movement along and away from the airfoil surface completes the stall onset. During its residence on the airfoil, fluid from the leading-edge region continuously supplies this vortex along the viscous-inviscid boundary (e.g., see figs. 14, electrode #1). As can be seen from the locus of arrows indicating the local directions of flow (fig. 13) that accompany the first and second major vortex boundaries, a moving stagnation point exists on the surface between these two vortices. By interpolation, the initial location of this stagnation point is between 10% and 15% chord. Thus, most of the vorticity in the leading-edge vortex comes from the forward portion of the airfoil, and it appears that only a minority of the airfoil surface actually comes into contact with any of the fluid contributing to the inception of the second major vortex. It is not until later that the downstream locations are observed to be progressively entrained by the vortex as it passes along the airfoil.

CONCLUSIONS

Based on flow visualization experiments performed on a modified NACA 0012 airfoil in a water tunnel at $k = 0.25$, $Re_c = 21{,}000$, and $\alpha = 10° + 10° \sin \omega t$, the following conclusions can be made.

1. Hydrogen bubbles can be successfully employed as flow tracers to expose, independently, the predominantly viscous or inviscid domains.

2. The boundary layer on the airfoil is laminar through stall and there is no evidence of the presence of the classical high Reynolds number laminar separation bubble in either the steady or dynamic case.

3. Starting as a gradual progression of reversed flow moving toward the leading edge of the airfoil, a free-shear layer is found to momentarily exist over the entire upper surface without any appreciable disturbance of the viscous-inviscid boundary.

4. After the airfoil has exceeded the static-stall angle, a flow protuberance appears near the leading edge and minor vortices begin to evolve from an expanding instability of the free-shear layer over the rear portion of the airfoil.

5. The complete breakdown of the shear layer culminates in the successive formation of two major vortices: the first vortex originates around 25% chord, becomes quite distinguishable at midchord, and then moves off the airfoil; the second vortex, its origin nearer the leading edge, becomes clearly identifiable around 25% chord. While the first vortex appears to be the direct result of a shear wave instability, the second vortex seems to accrue from the unification of numerous vortical movements

already developing within the latter half of the leading-edge protuberance. This second vortex is the one that is also observed at higher Reynolds numbers.

Ames Research Center
National Aeronautics and Space Administration
and
Aeromechanics Laboratory
U. S. Army Aviation R & D Command
Moffett Field, Calif. 94035, Oct. 25, 1977

REFERENCES

1. Olsen, J. H.; and Liu, H. T.: The Construction and Operation of a Water Tunnel in Application to Flow Visualization Studies of an Oscillating Airfoil. NASA CR-114696, May 1973.

2. Knapp, R. T.; Daily, J. W.; and Hammitt, F. G.: Cavitation. McGraw-Hill Book Co., 1970.

3. Merzkirch, Wolfgang: Flow Visualization. Academic Press, 1974.

4. Carr, Lawrence W.; McAlister, Kenneth W.; and McCroskey, William J.: Analysis of the Development of Dynamic Stall Based on Oscillating Airfoil Experiments. NASA TN D-8382, 1977.

5. Werlé, H.: Visualisation Hydrodynamique de l'Écoulement Autour d'une Pale Oscillante. ONERA Rapport Technique 56/1369 AN, 1976.

6. Mehta, Unmeel B.: Dynamic Stall of an Oscillating Airfoil. AGARD Conference Proceedings CP-227, Symposium on Unsteady Aerodynamics, Ottawa, Canada. Paper 23, 1977.

7. Gault, Donald E.: An Experimental Investigation of Regions of Separated Laminar Flow. NACA TN 3505, 1955.

8. Brown, F. N. M.: See the Wind Blow, University of Notre Dame, 27, 1971.

9. Roshko, Anatol: On the Wake and Drag of Bluff Bodies. J. Aeronaut. Sci., vol. 22, no. 2, 1955, pp. 124-132.

10. Paterson, Robert W.; Vogt, Paul G.; Fink, Martin R.; and Munch, C. Lee: Vortex Noise of Isolated Airfoils. J. Aircraft, vol. 10, no. 5, 1973, pp. 296-302.

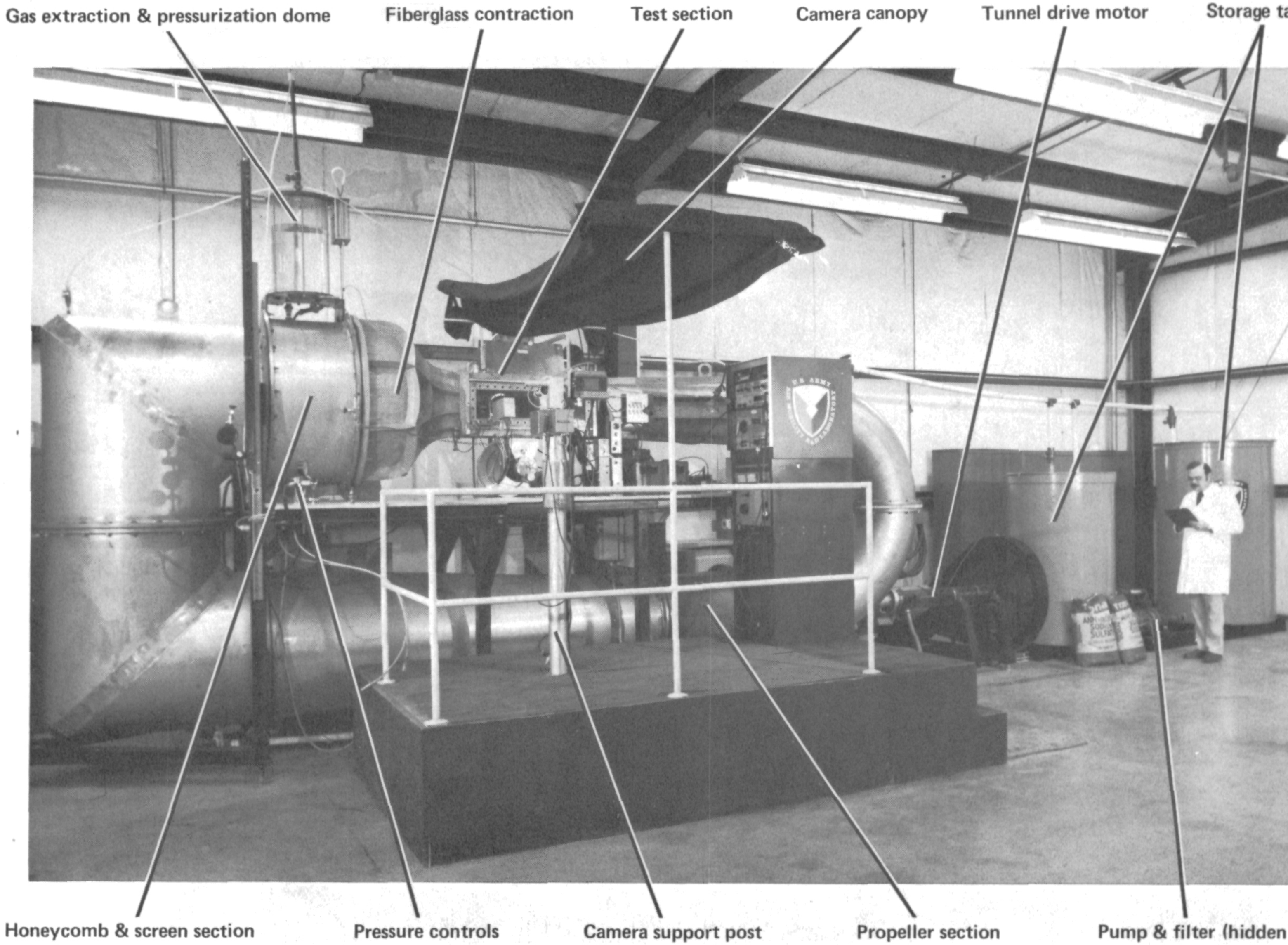

Figure 1.- Aeromechanics Laboratory (AVRADCOM) 0.2 m X 0.3 m Water Tunnel.

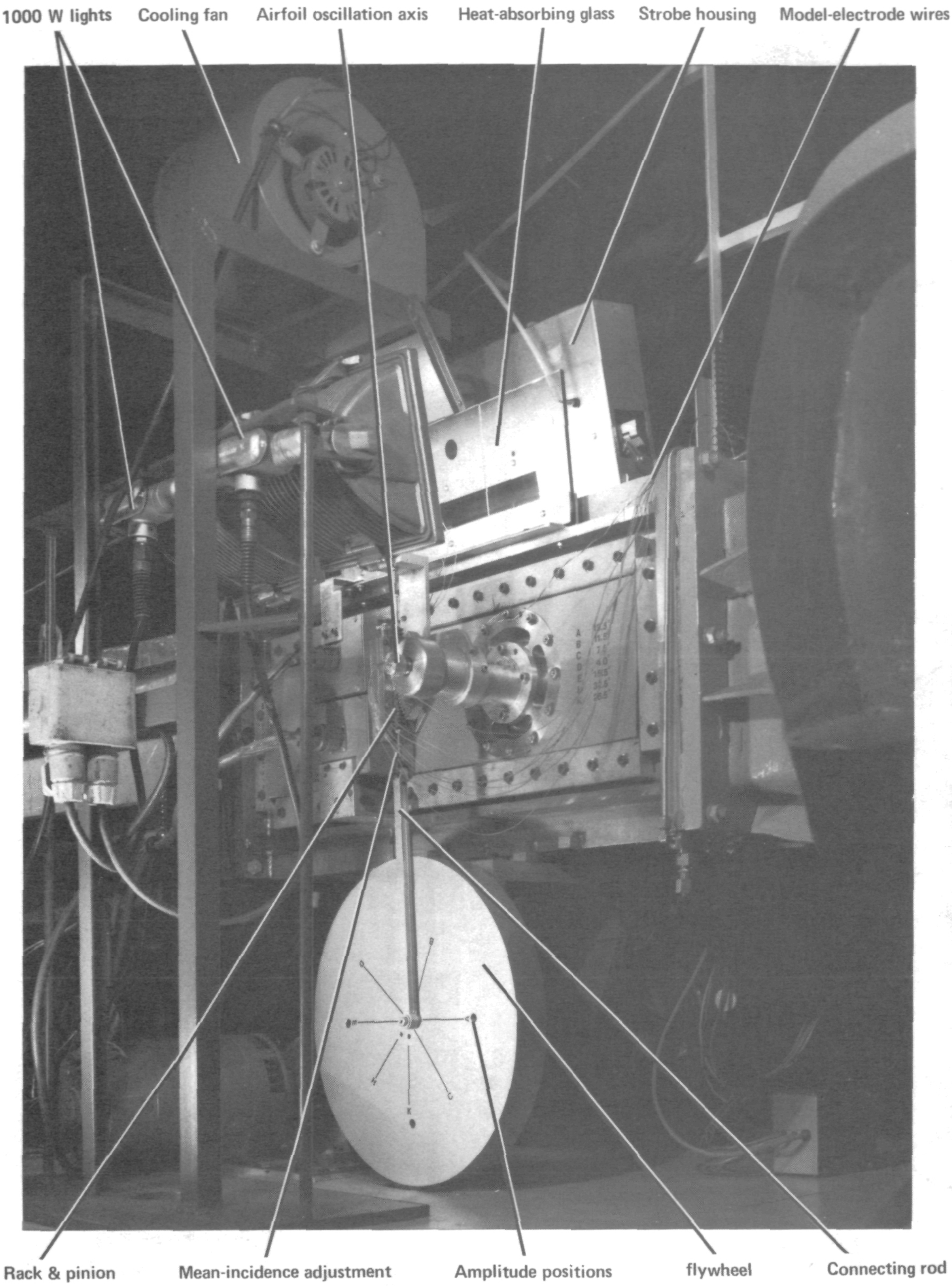

Figure 2.- Rear view of test section.

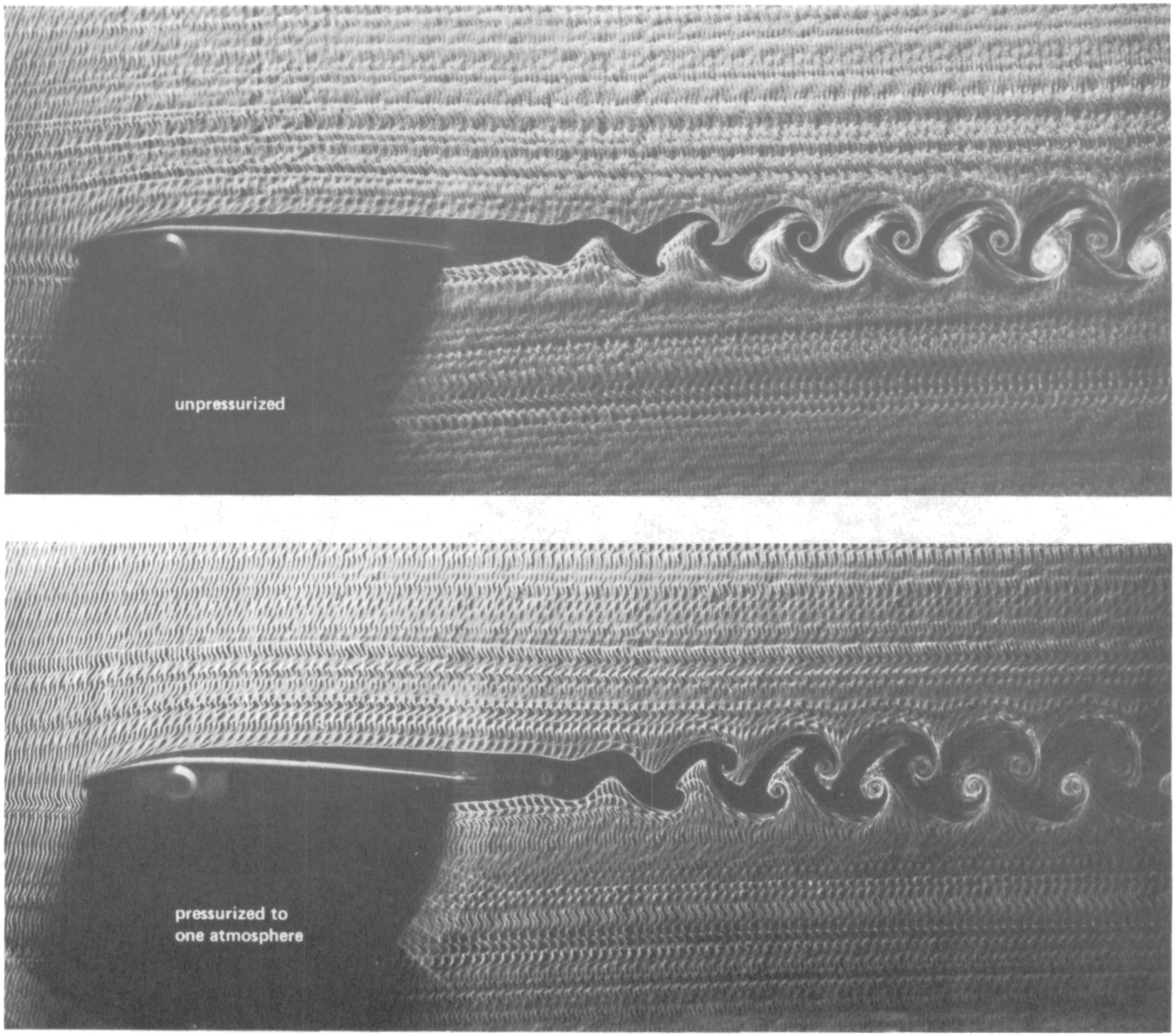

Figure 3.- Effect of pressurization on free-stream-generated bubbles.

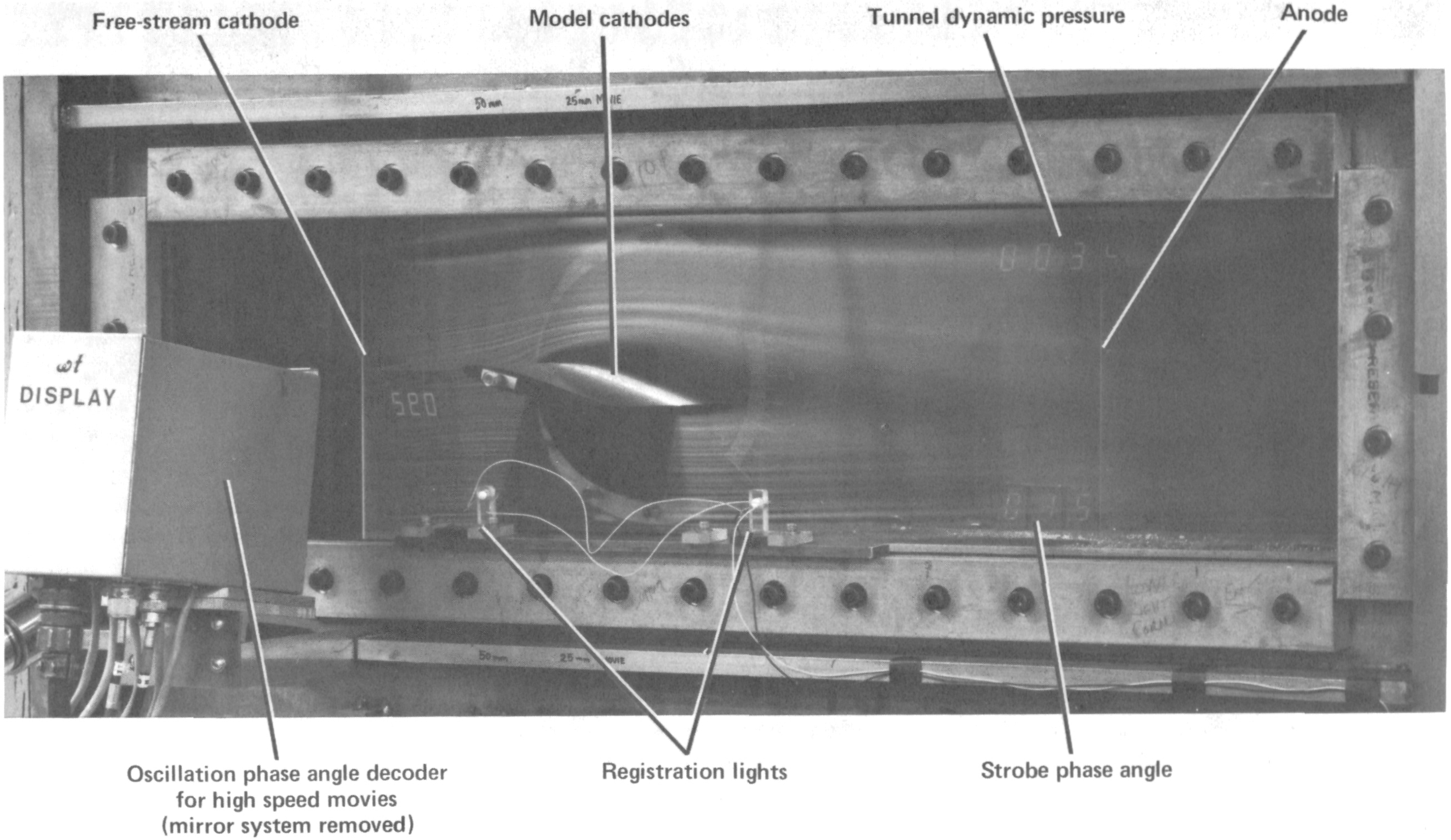

Figure 4.- Front view of test section.

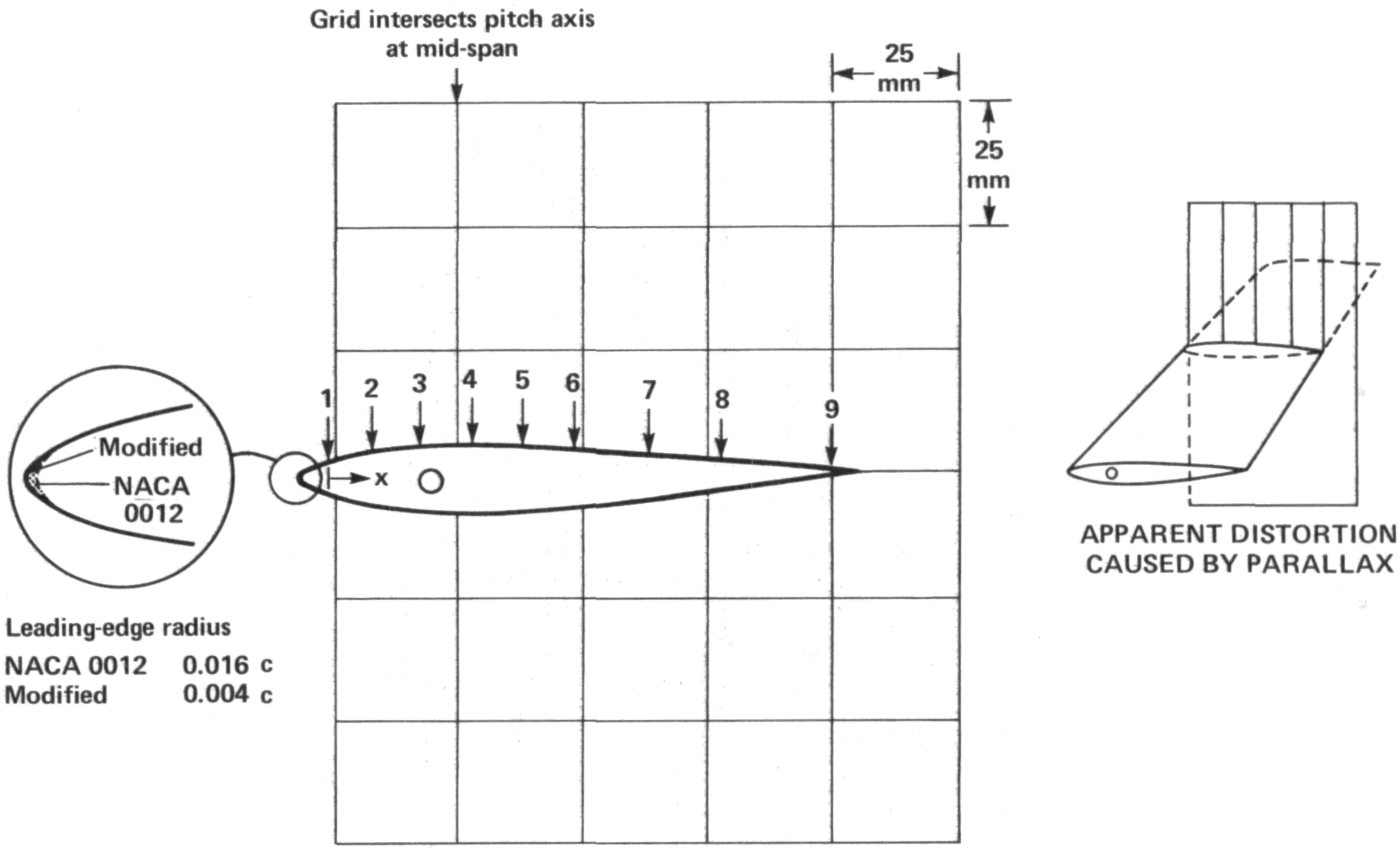

Electrode locations (x/c)

#1	0.0	#4	0.29	#7	0.63
#2	0.09	#5	0.39	#8	0.77
#3	0.18	#6	0.48	#9	1.0

Figure 5.- Model profile and electrode locations.

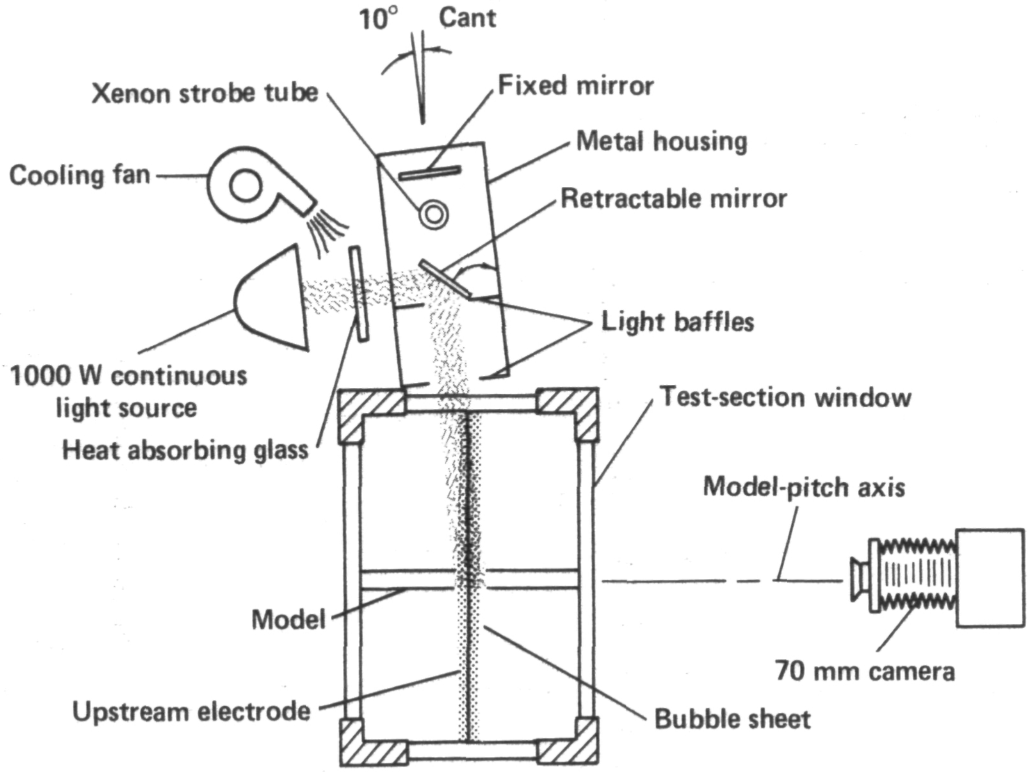

Figure 6.- Orientation of apparatus (as viewed from upstream) required to illuminate bubbles.

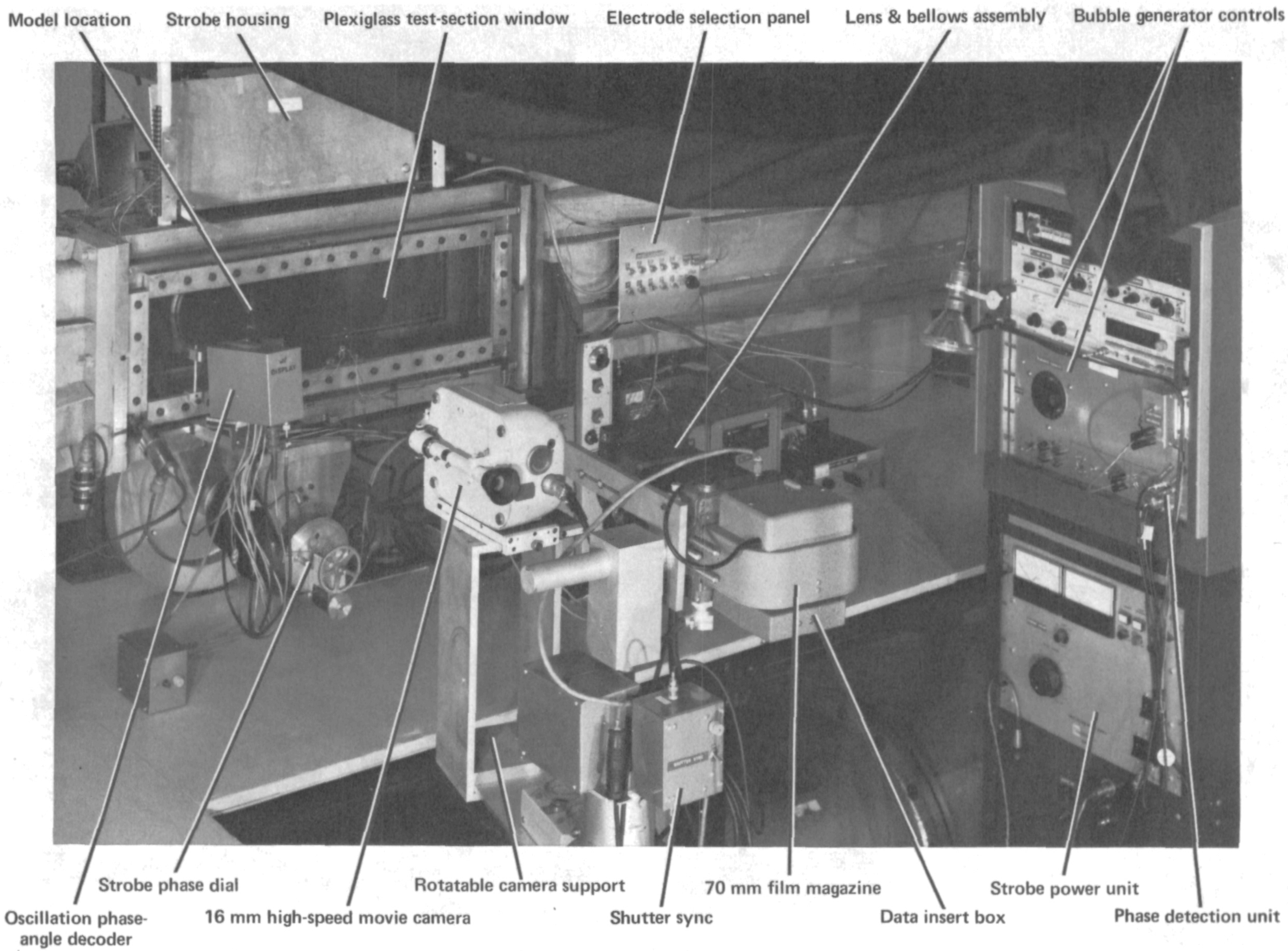

Figure 7.- Instrumentation layout.

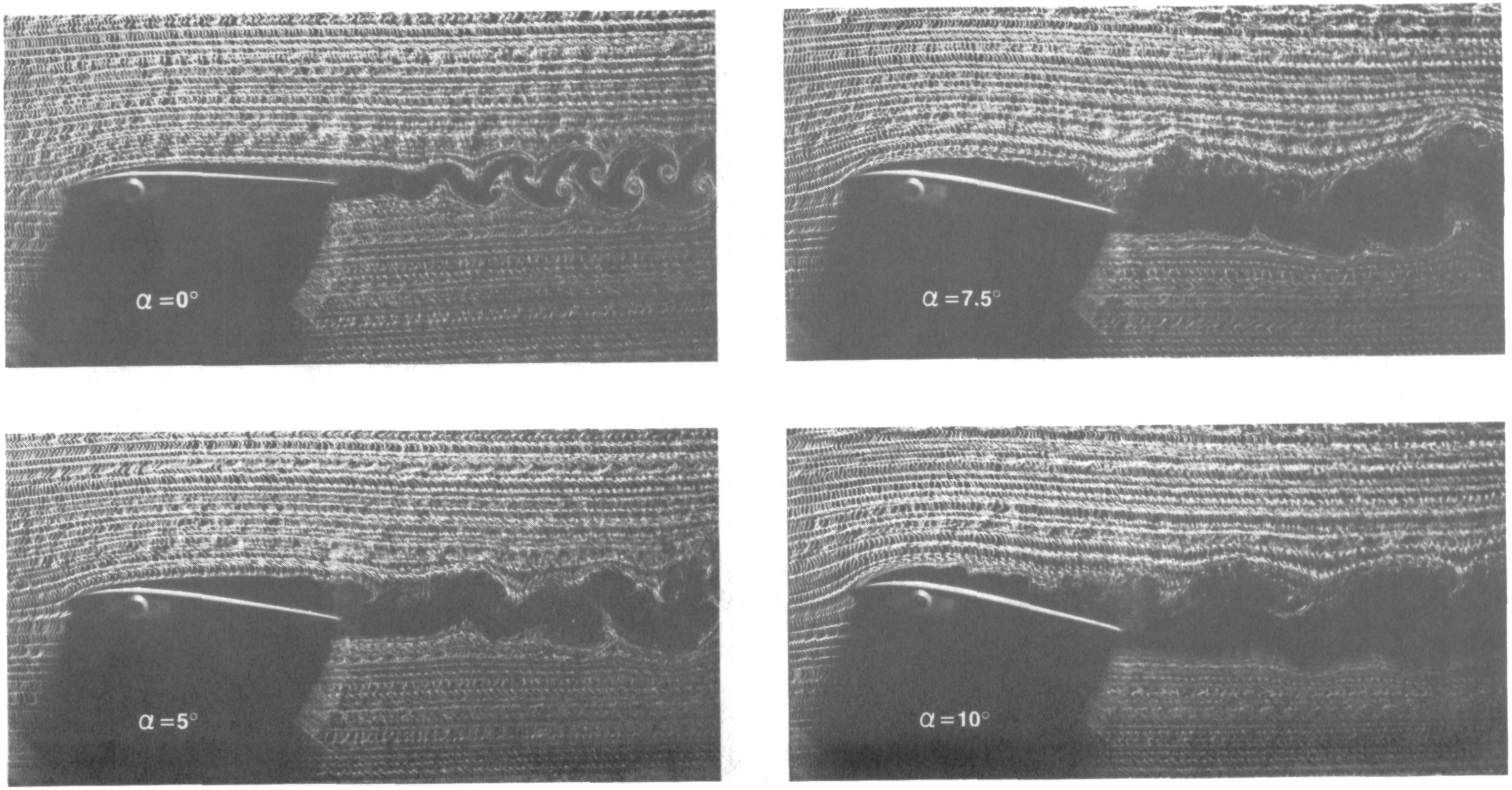

Figure 8.- Free-stream flow pattern with the airfoil fixed at various angles of attack.

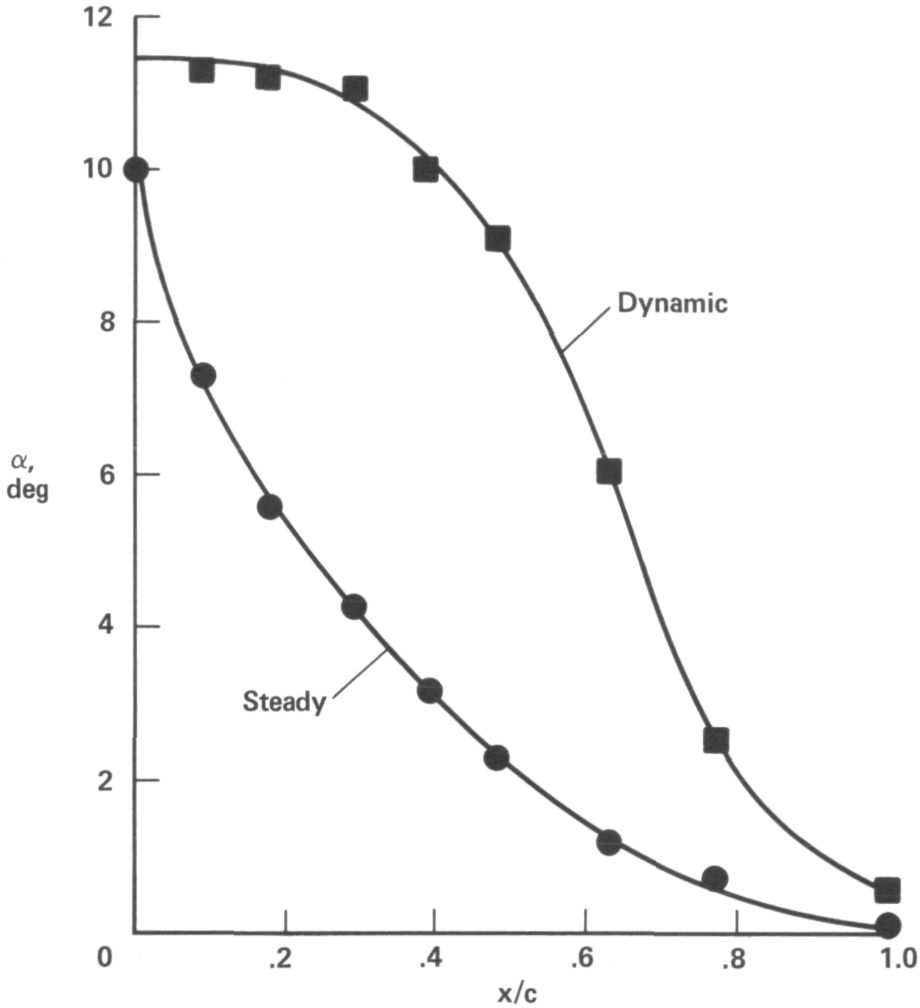

Figure 9.- Onset of reversed flow.

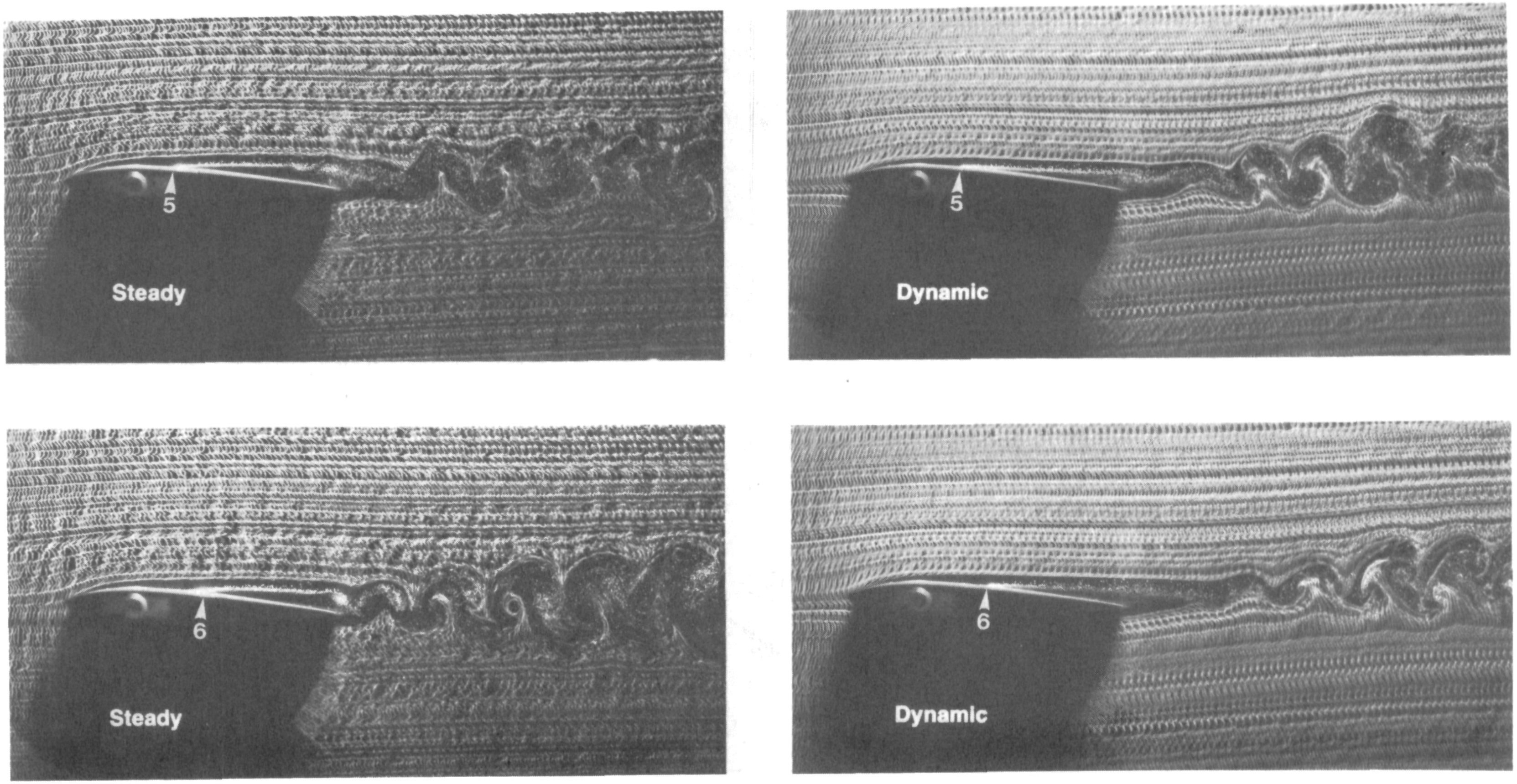

(a) $\alpha = 3°$

Figure 10.- Effect of airfoil oscillation on the direction of boundary layer flow at various chord locations.

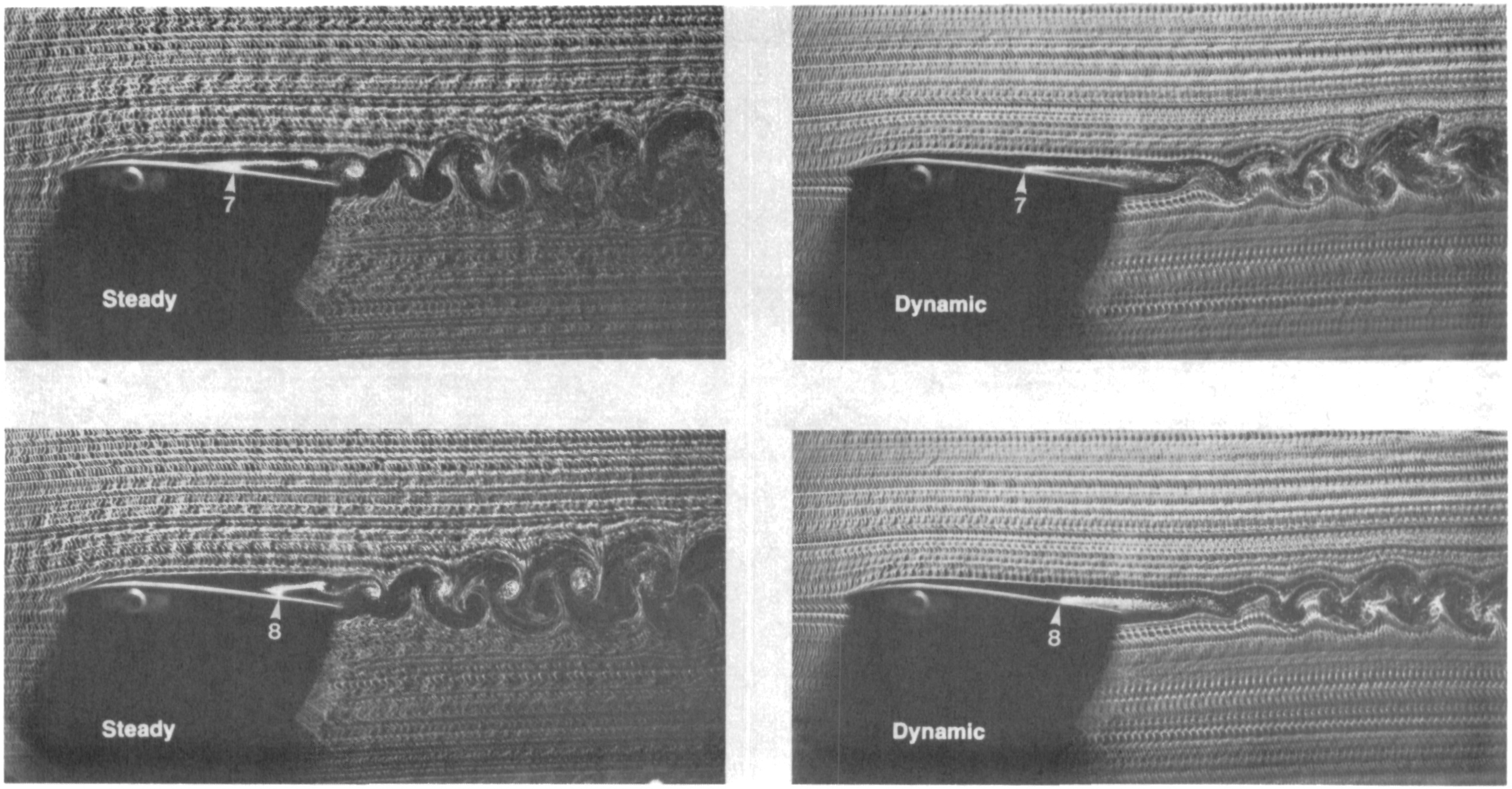

(a) Concluded.

Figure 10.- Continued.

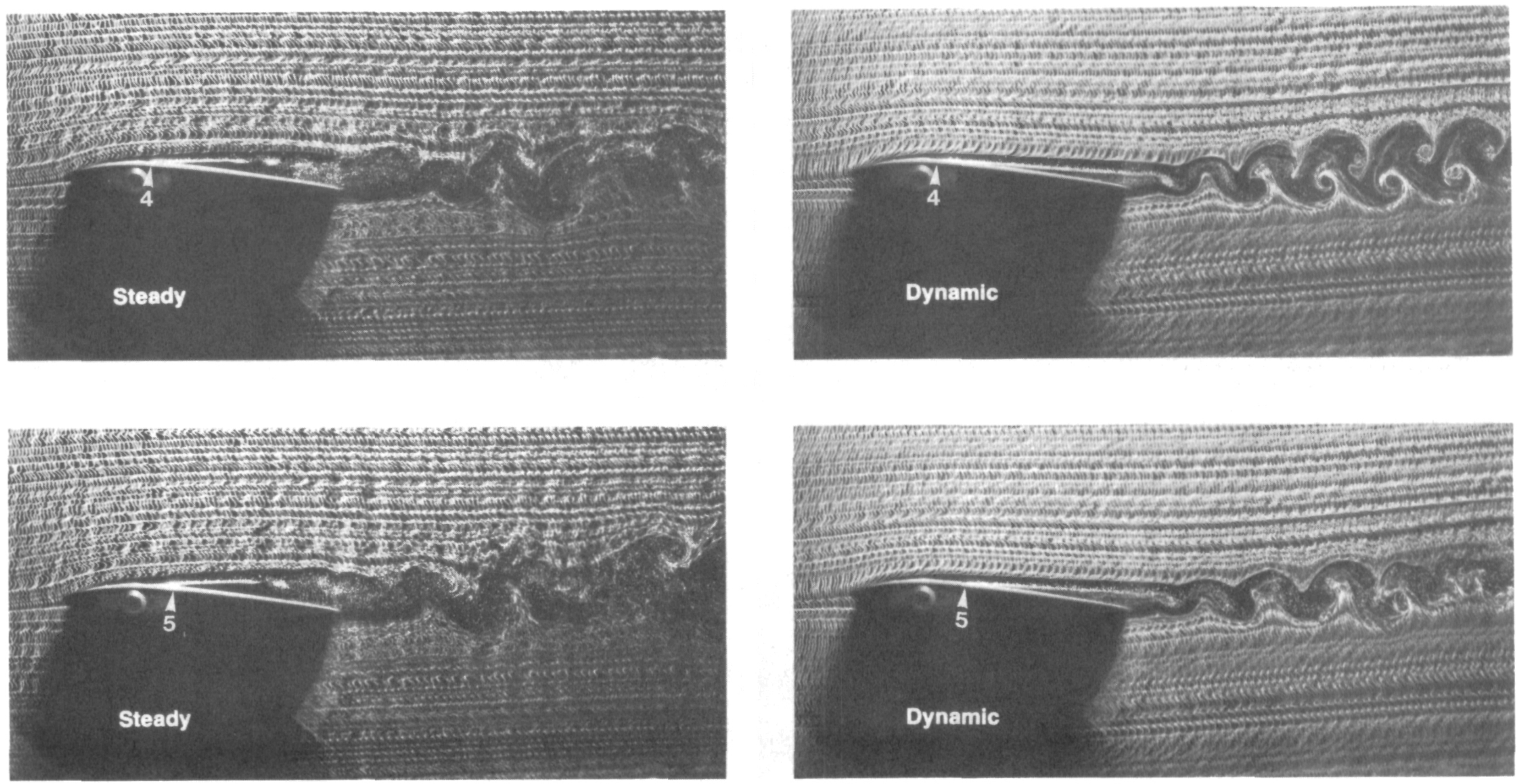

(b) $\alpha = 4°$

Figure 10.- Continued.

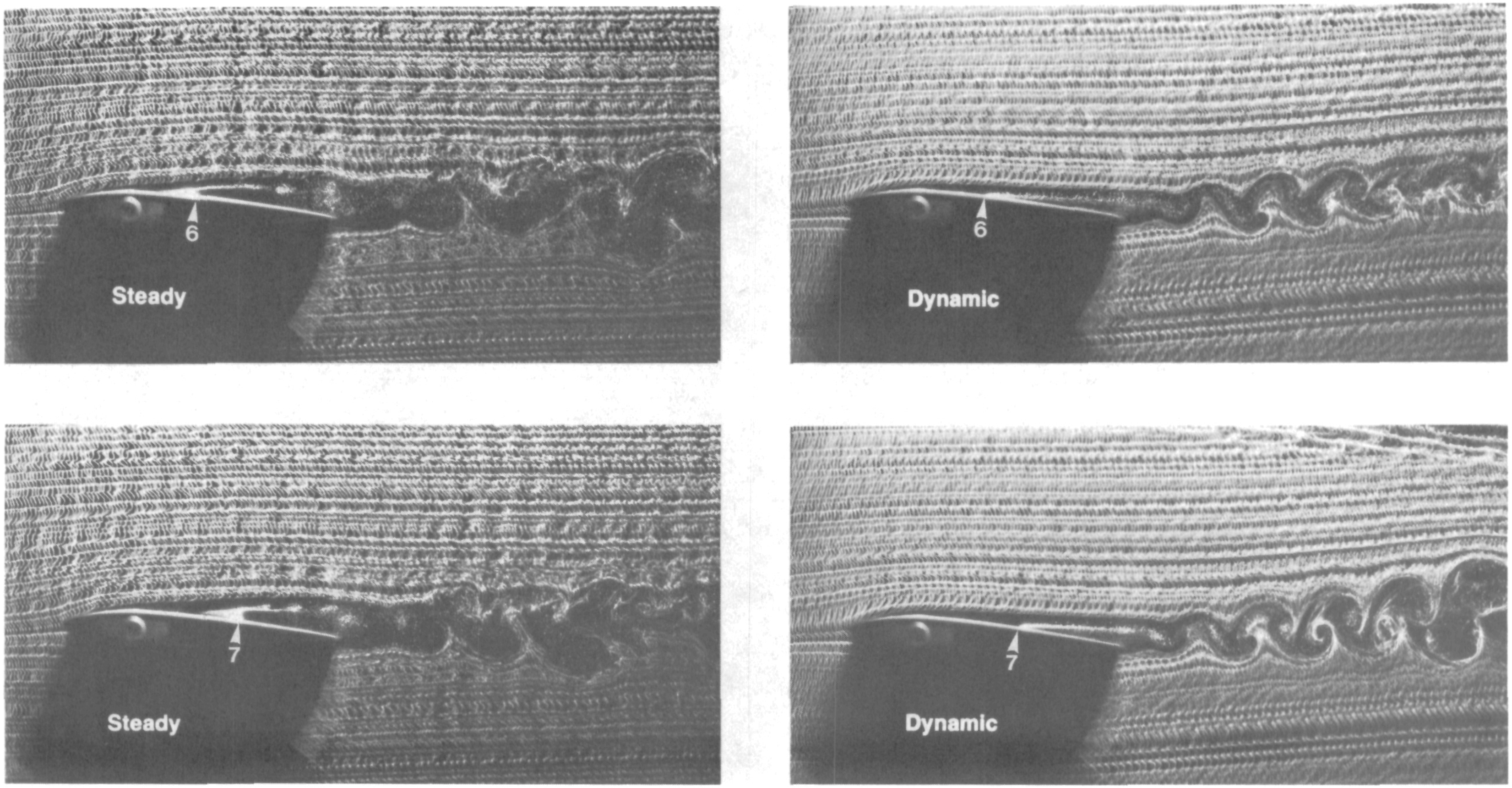

(b) Concluded.

Figure 10. - Continued.

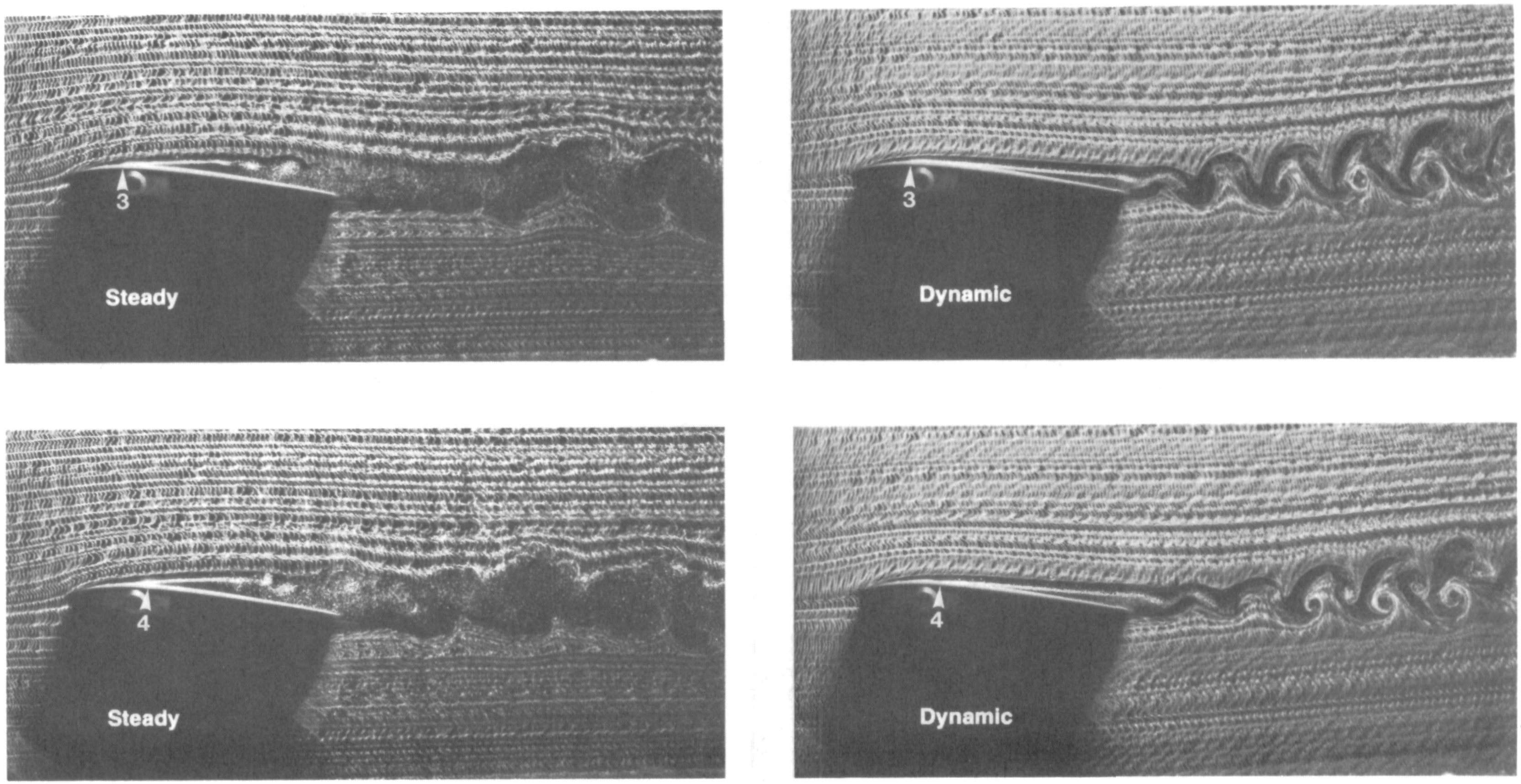

(c) $\alpha = 5°$

Figure 10.- Continued.

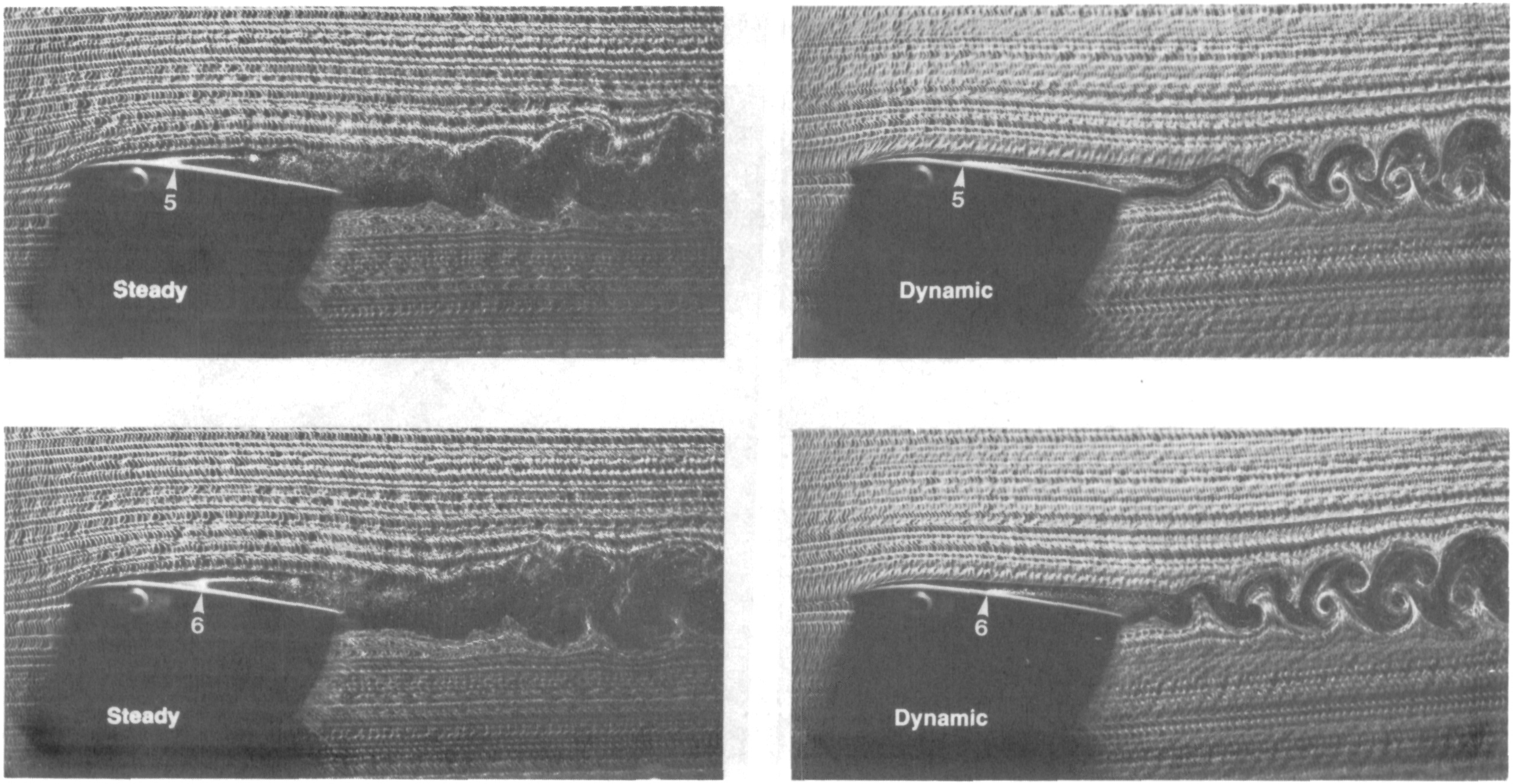

(c) Concluded.

Figure 10.- Concluded.

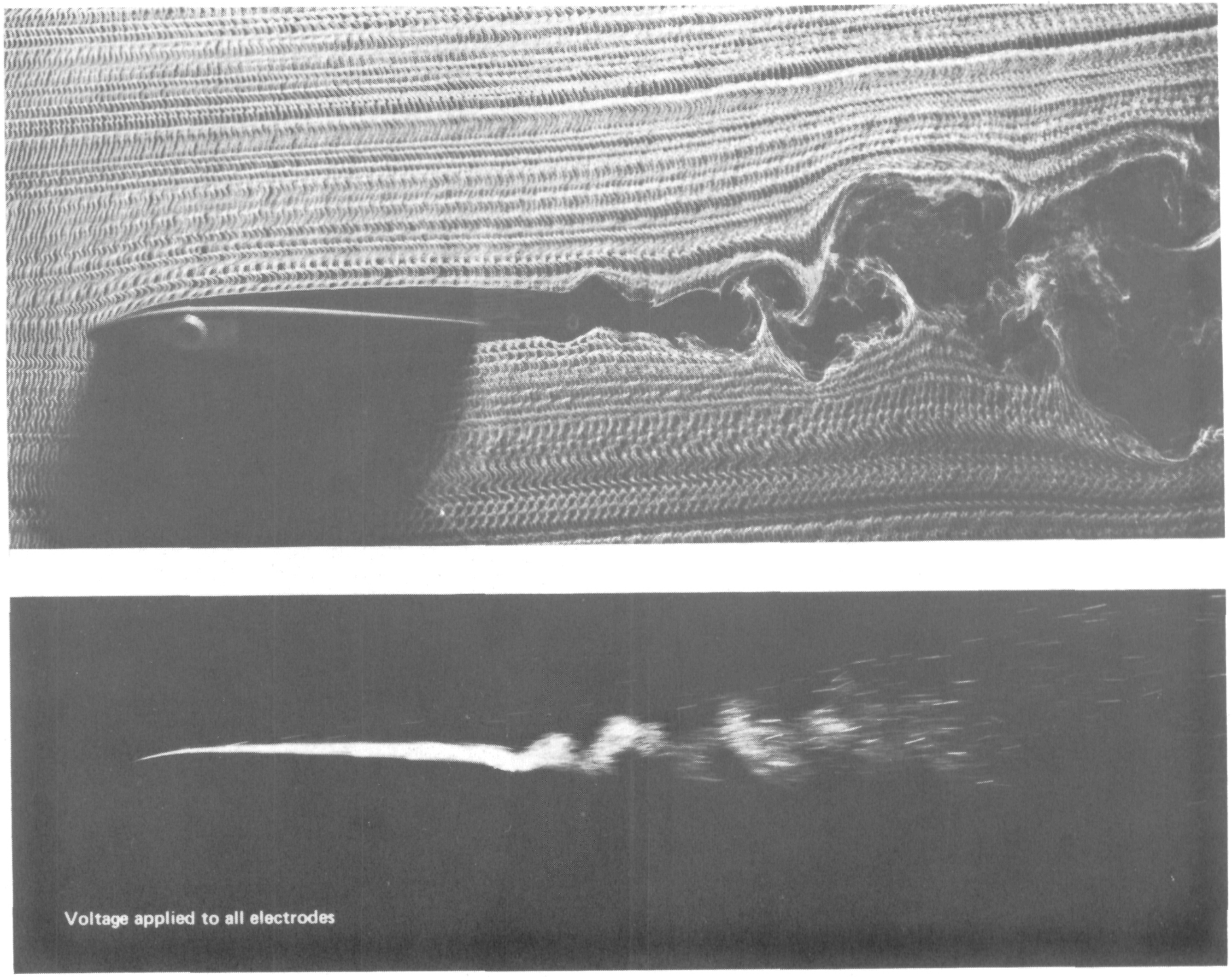

(a) ωt = 270° (α = 0°)

Figure 11.- Flow patterns from free-stream- and model-generated bubbles every 15° of azimuth during a cycle of airfoil oscillation.

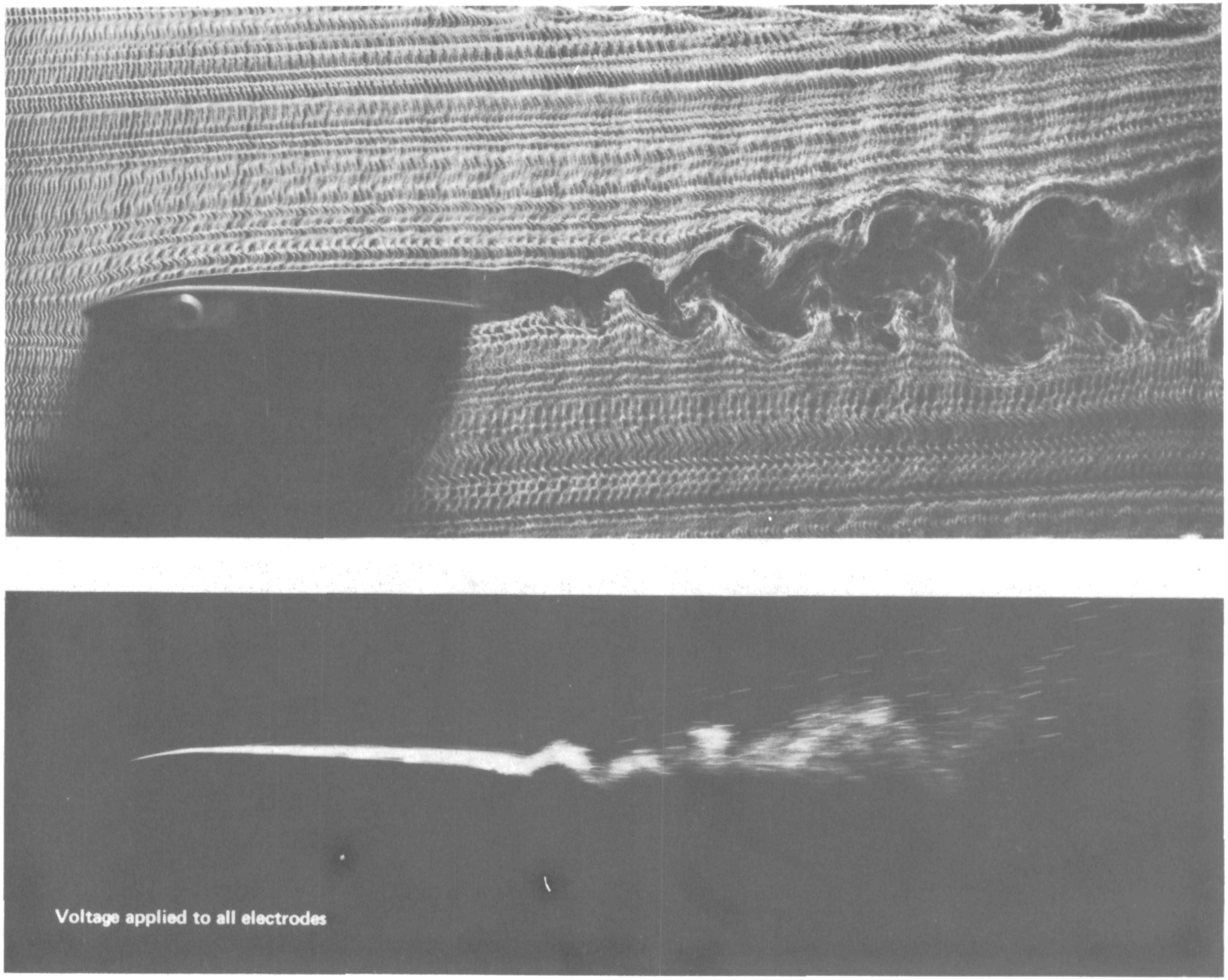

(b) ωt = 285° (α = 0.3°)

Figure 11.- Continued.

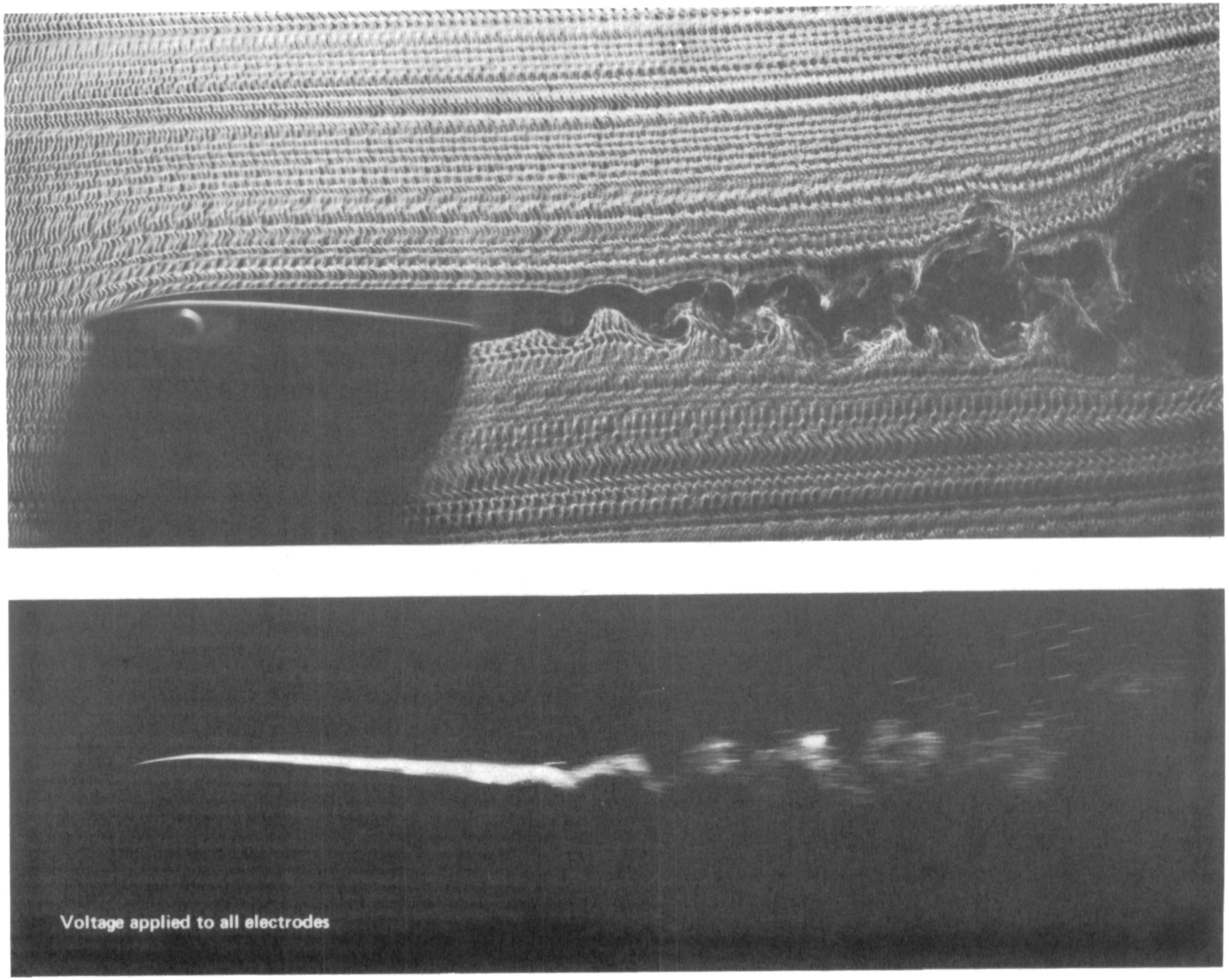

(c) $\omega t = 300°$ ($\alpha = 1.3°$)

Figure 11.- Continued.

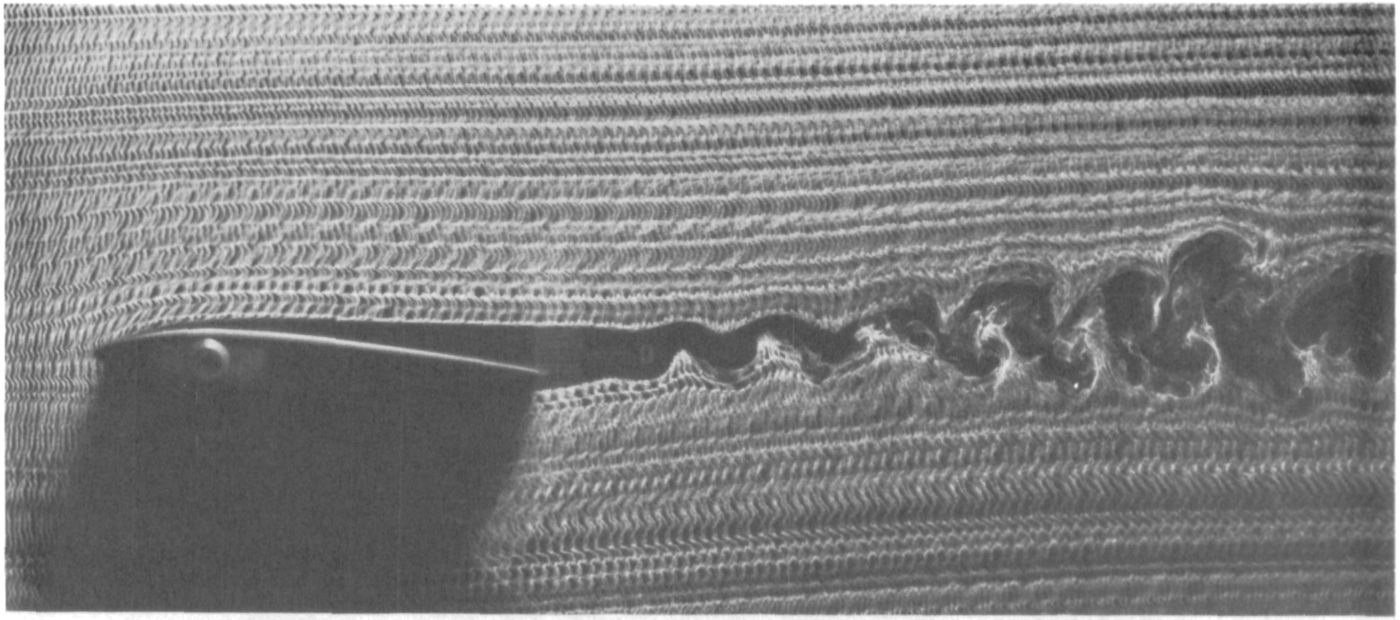

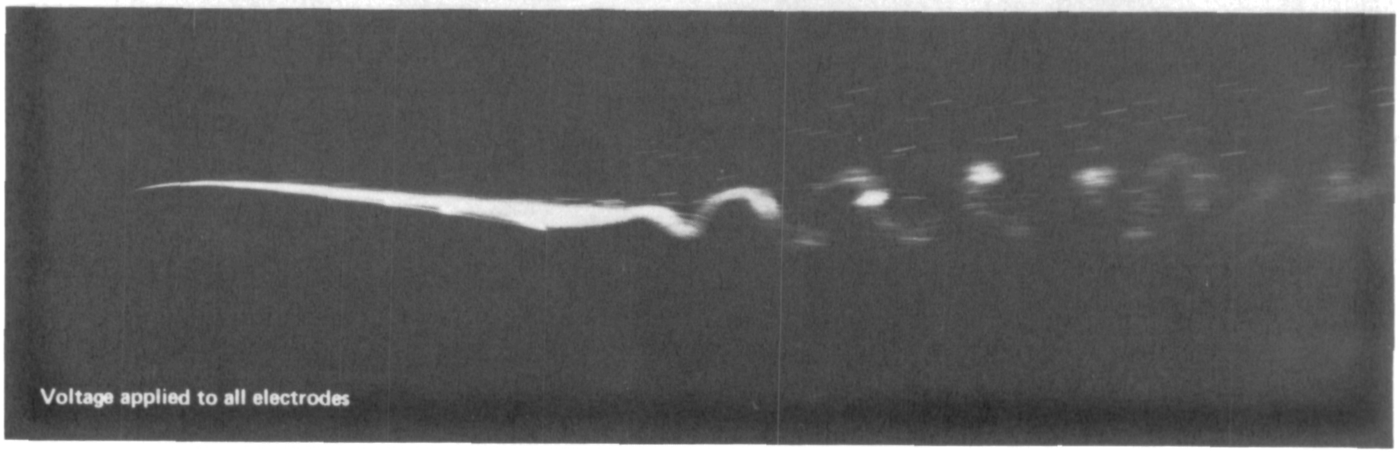

(d) $\omega t = 315°$ ($\alpha = 2.9°$)

Figure 11.- Continued.

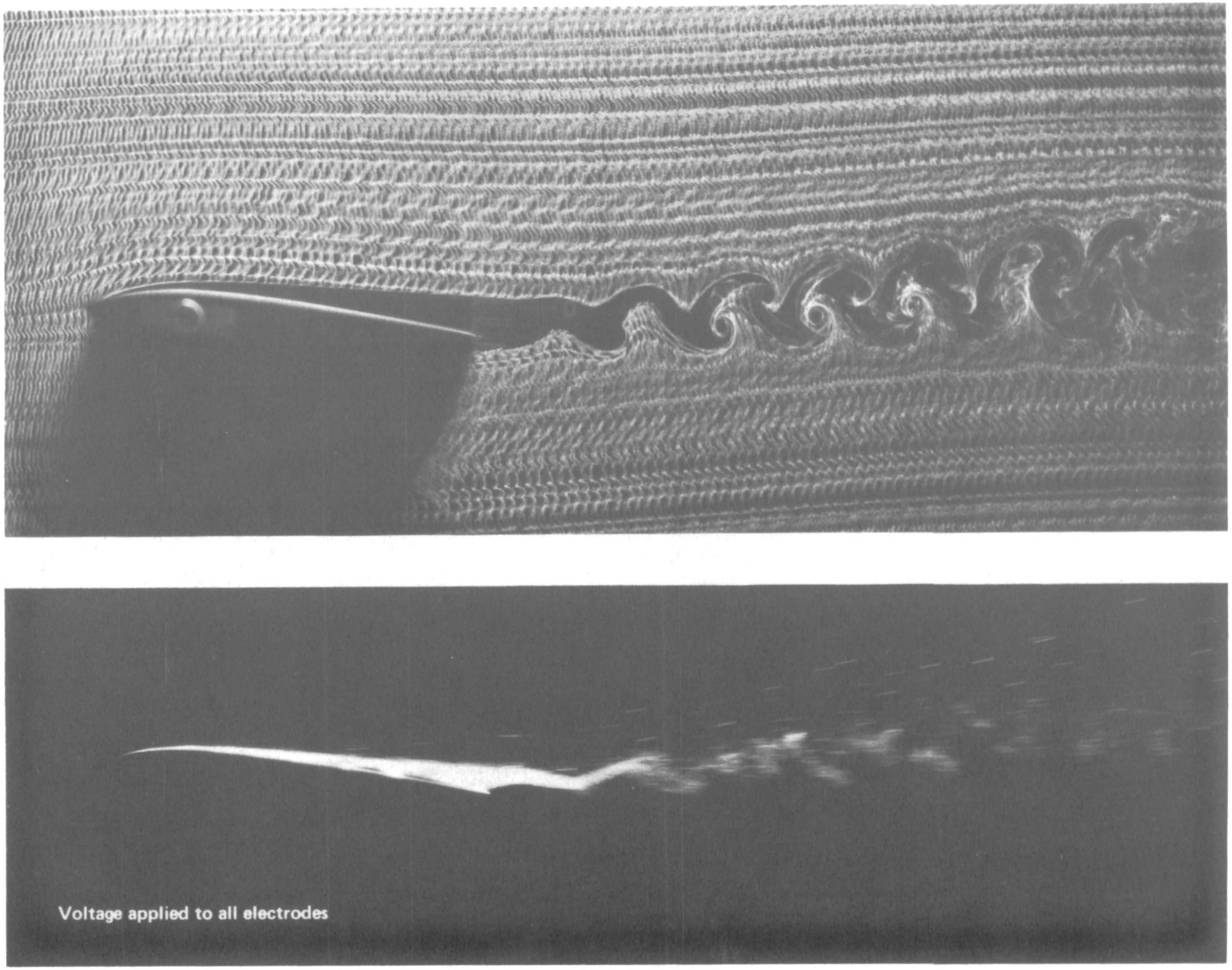

(e) $\omega t = 330°$ ($\alpha = 5.0°$)

Figure 11.- Continued.

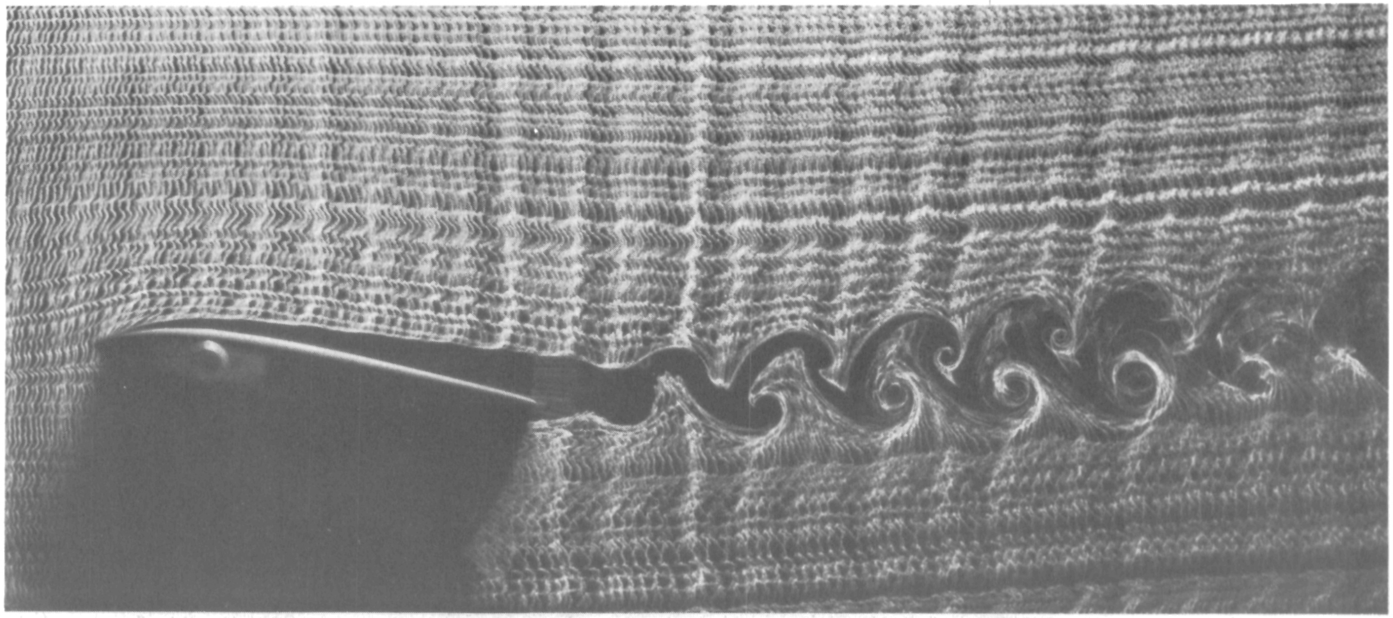

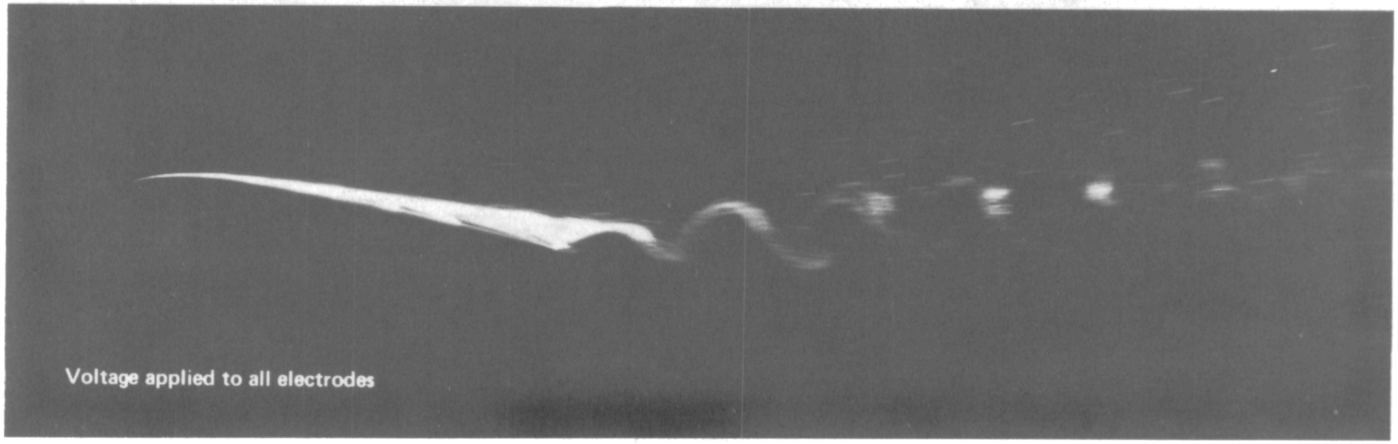

(f) $\omega t = 345°$ ($\alpha = 7.4°$)

Figure 11.- Continued.

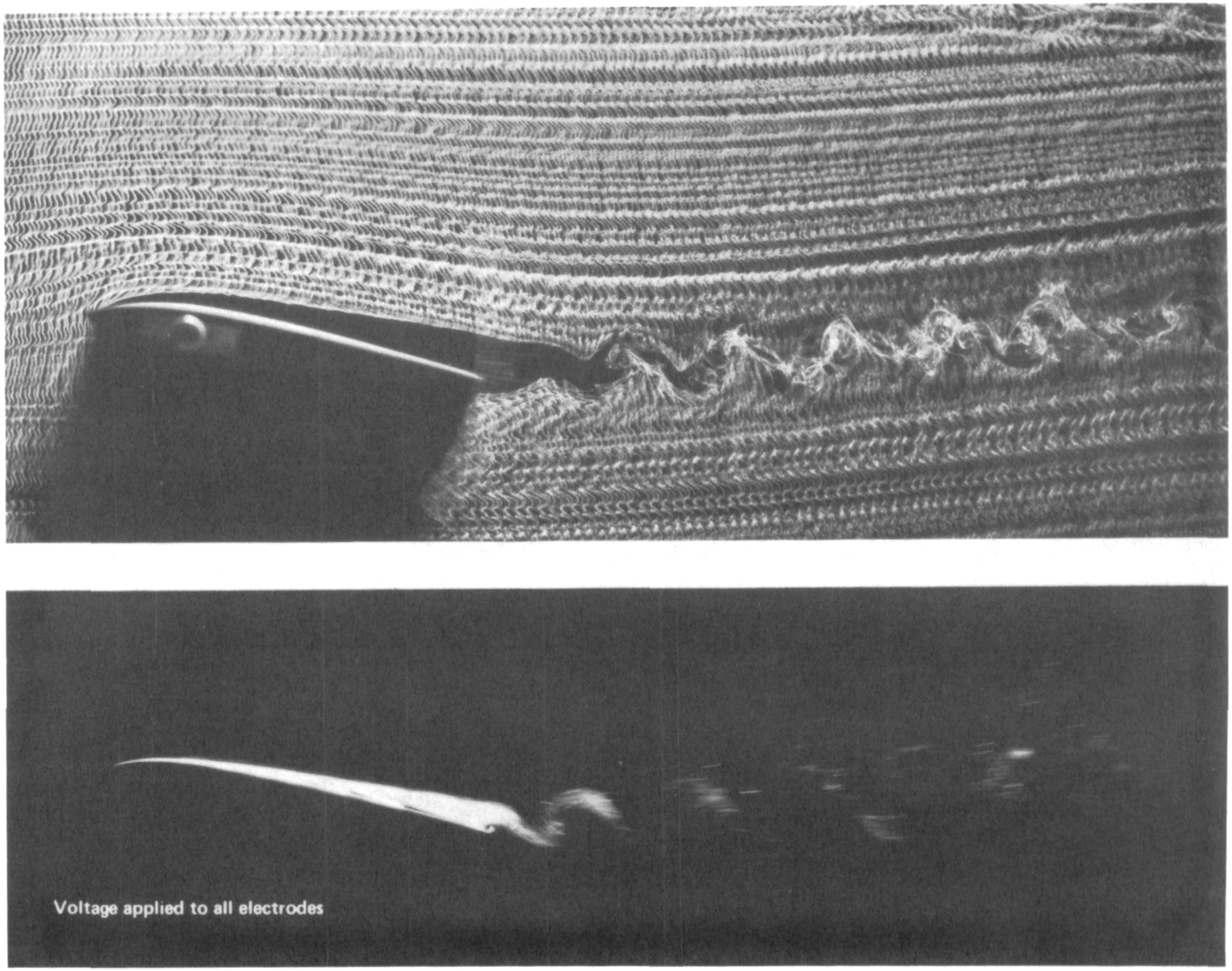

(g) $\omega t = 0°$ ($\alpha = 10.0°$)

Figure 11.- Continued.

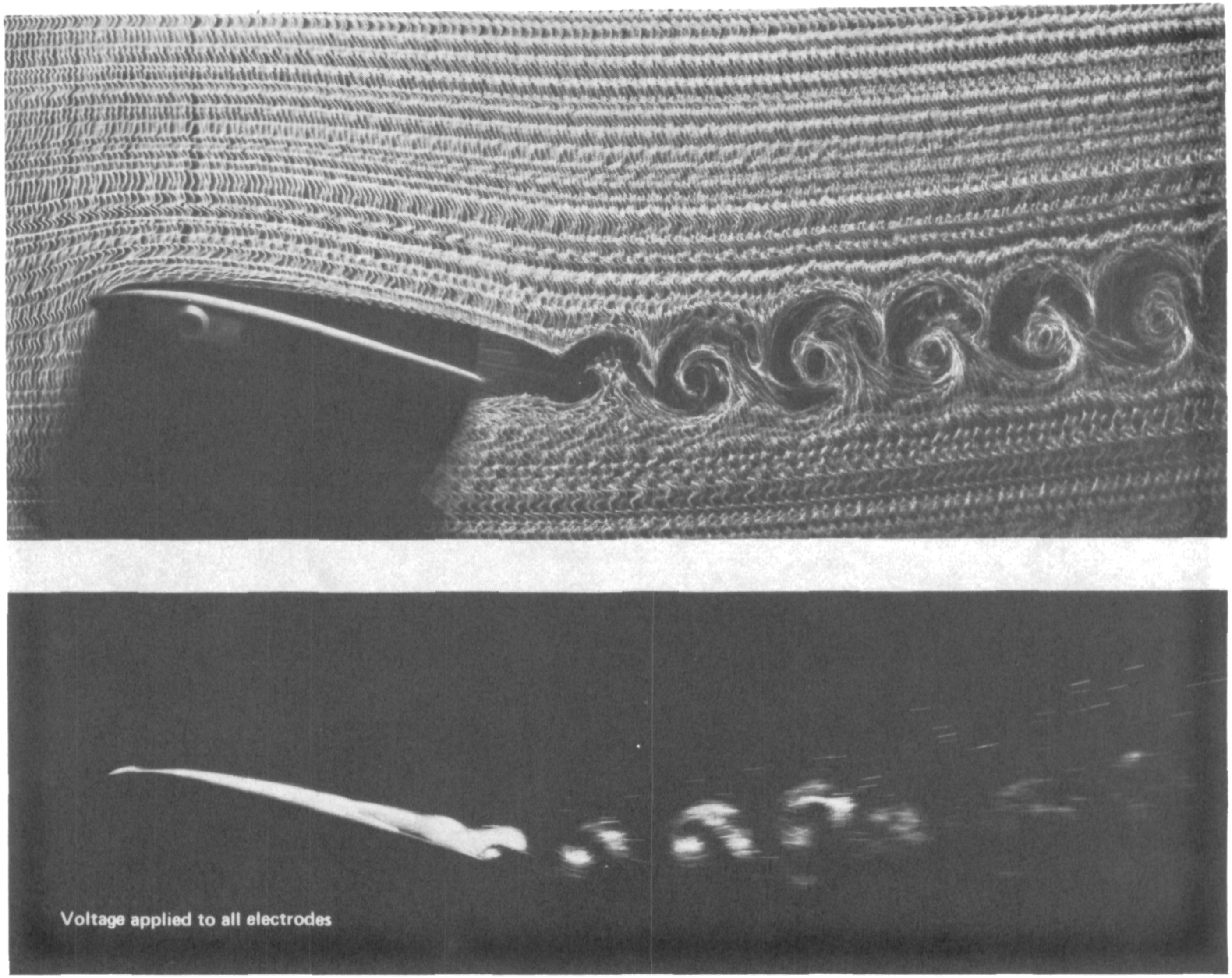

(h) $\omega t = 15°$ ($\alpha = 12.6°$)

Figure 11.- Continued.

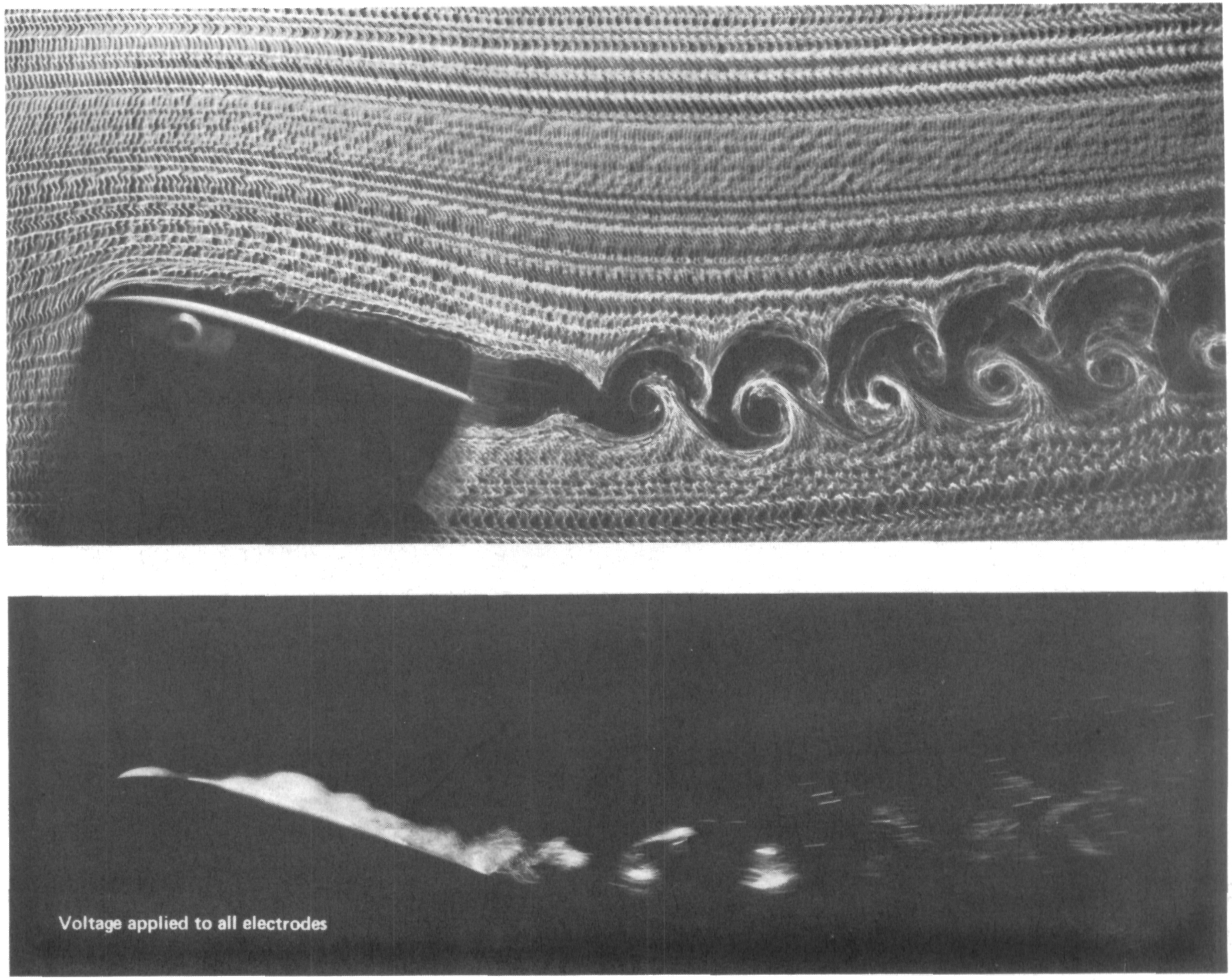

(i) $\omega t = 30°$ ($\alpha = 15.0°$)

Figure 11.- Continued.

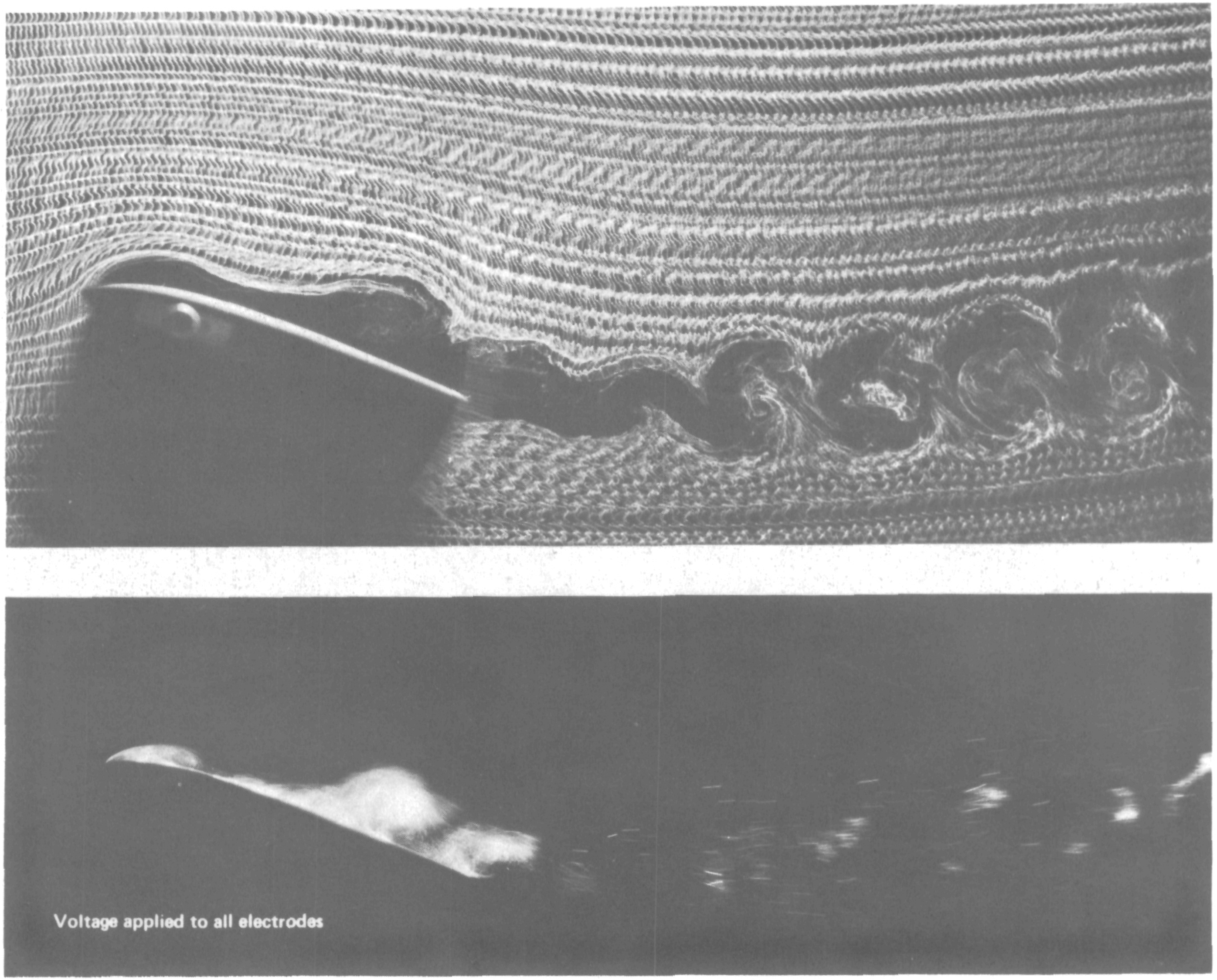

(j) $\omega t = 45°$ ($\alpha = 17.1°$)

Figure 11.- Continued.

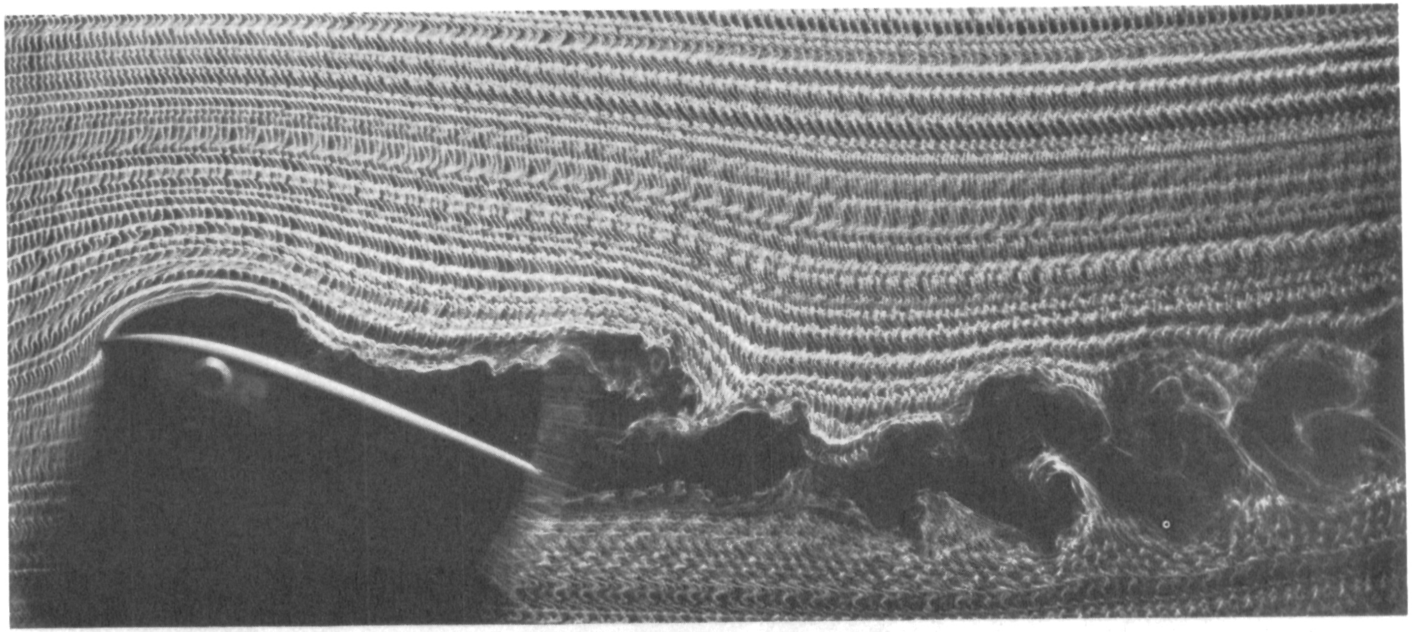

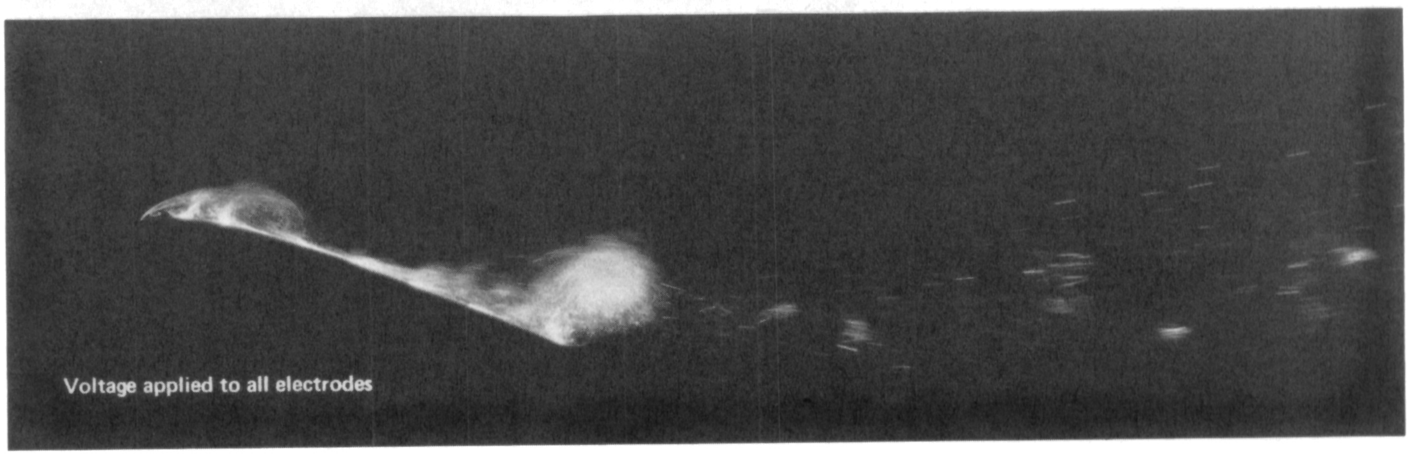

(k) $\omega t = 60°$ ($\alpha = 18.7°$)

Figure 11.- Continued.

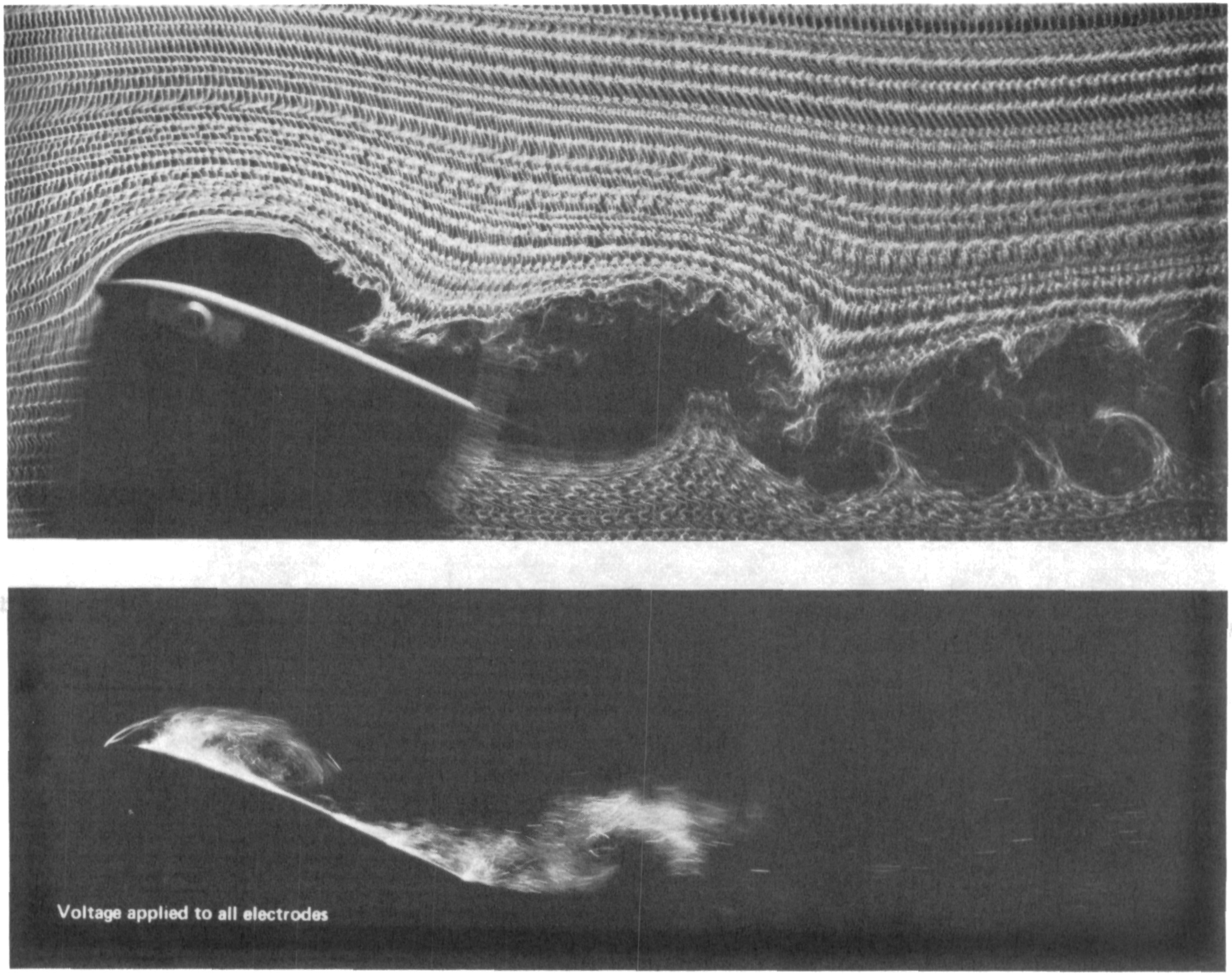

(1) $\omega t = 75°$ ($\alpha = 19.7°$)

Figure 11.- Continued.

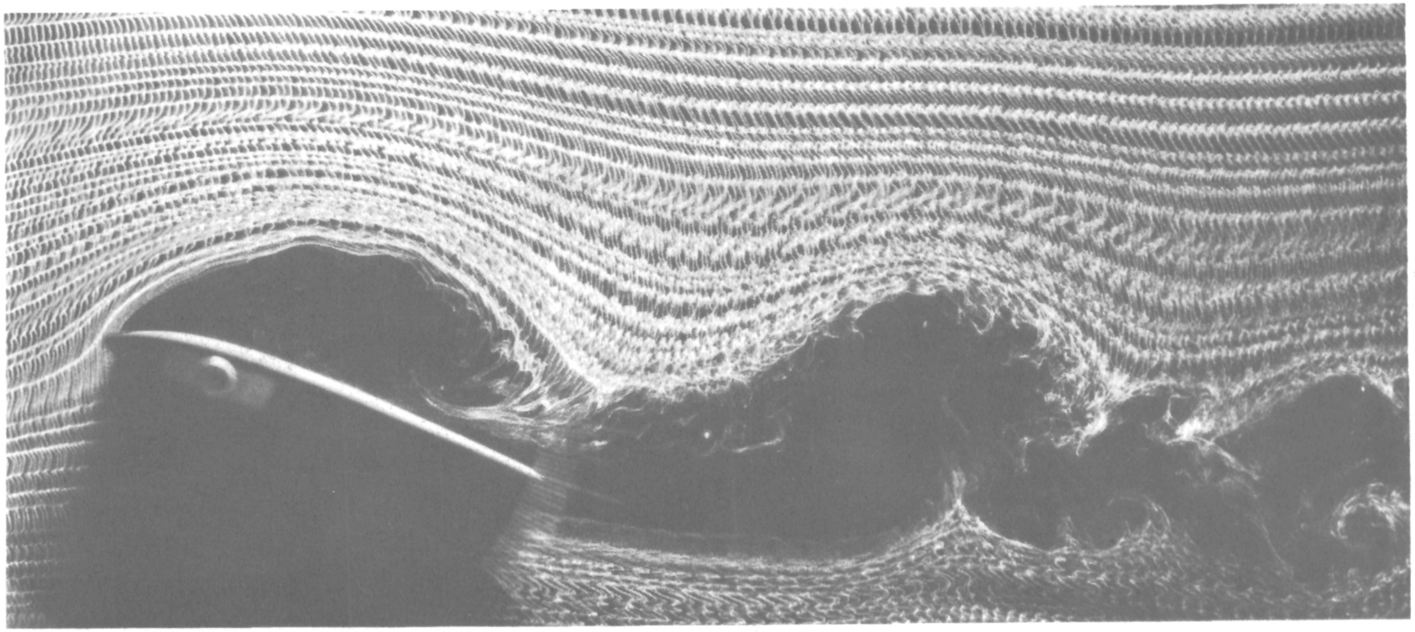

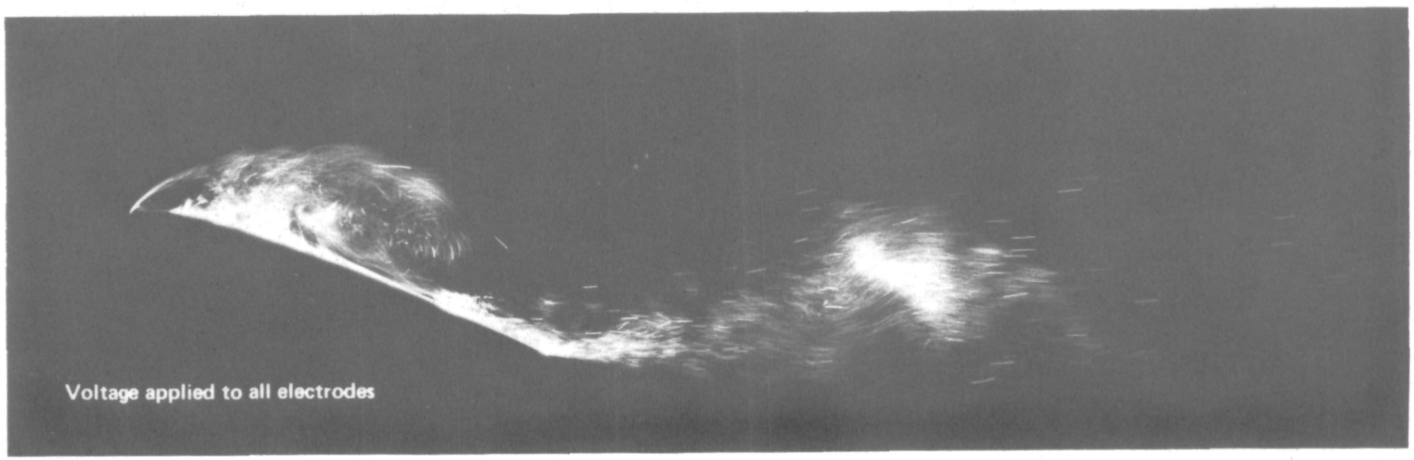

(m) $\omega t = 90°$ ($\alpha = 20.0°$)

Figure 11.- Continued.

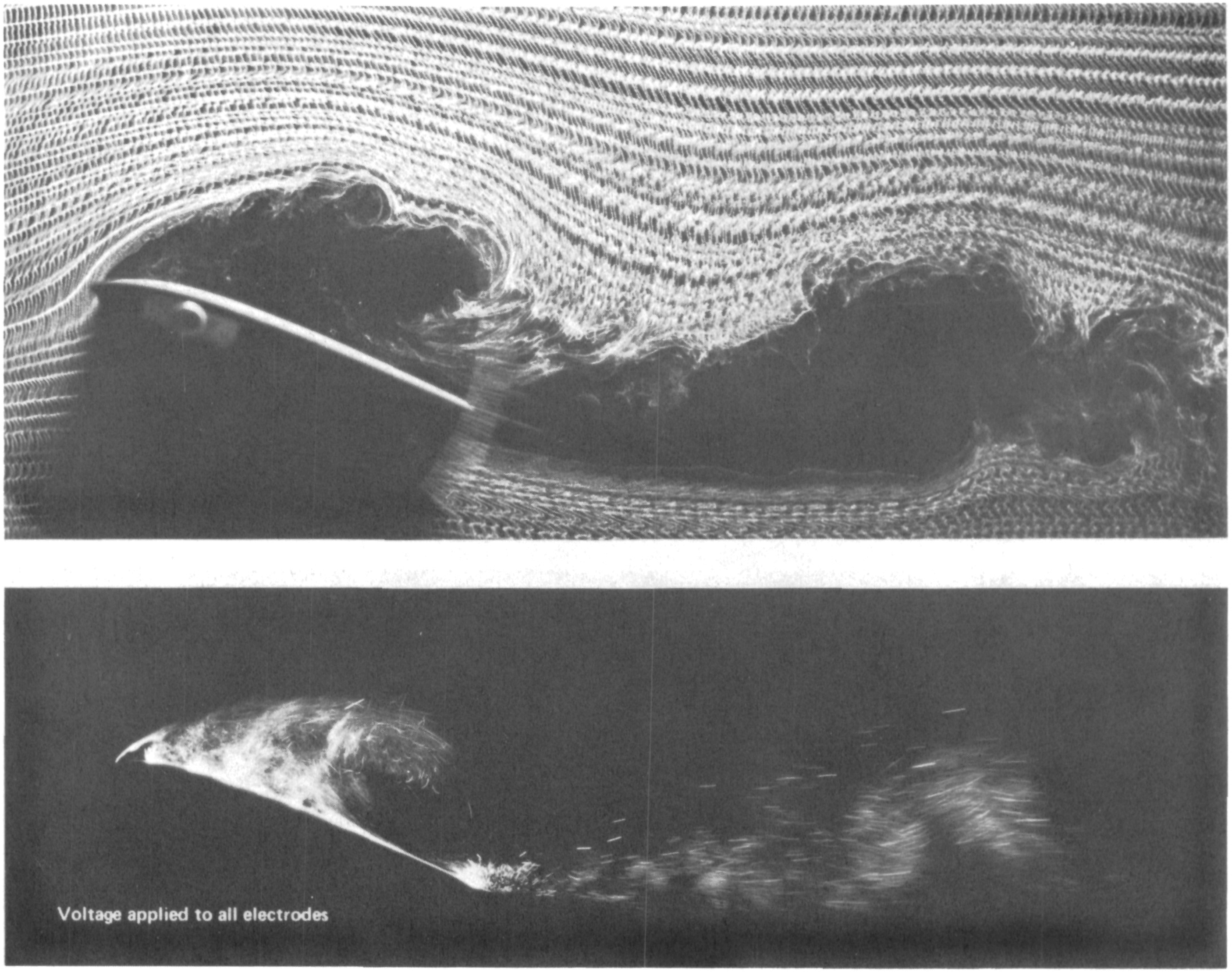

(n) $\omega t = 105°$ ($\alpha = 19.7°$)

Figure 11.- Continued.

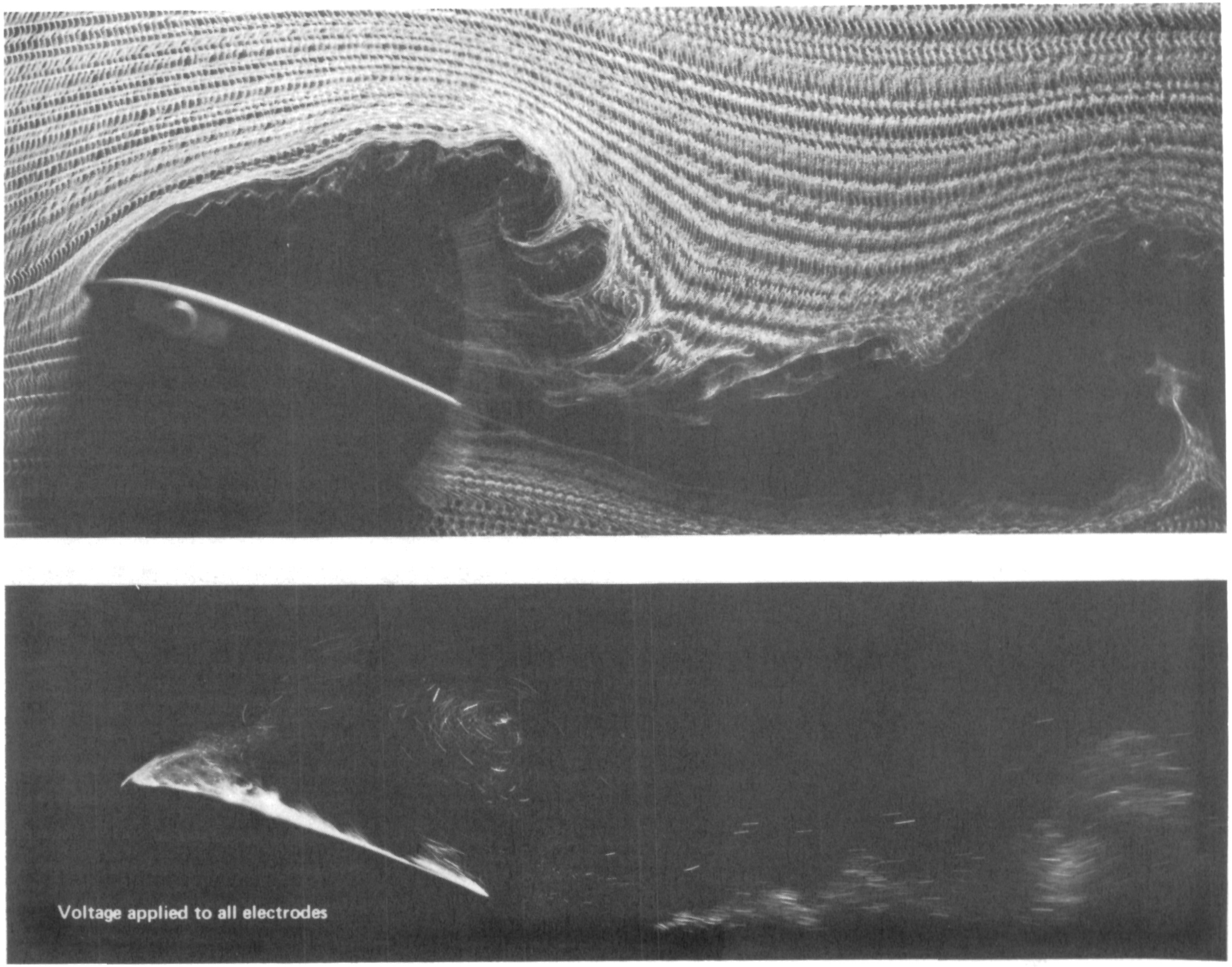

(o) $\omega t = 120°$ ($\alpha = 18.7°$)

Figure 11.- Continued.

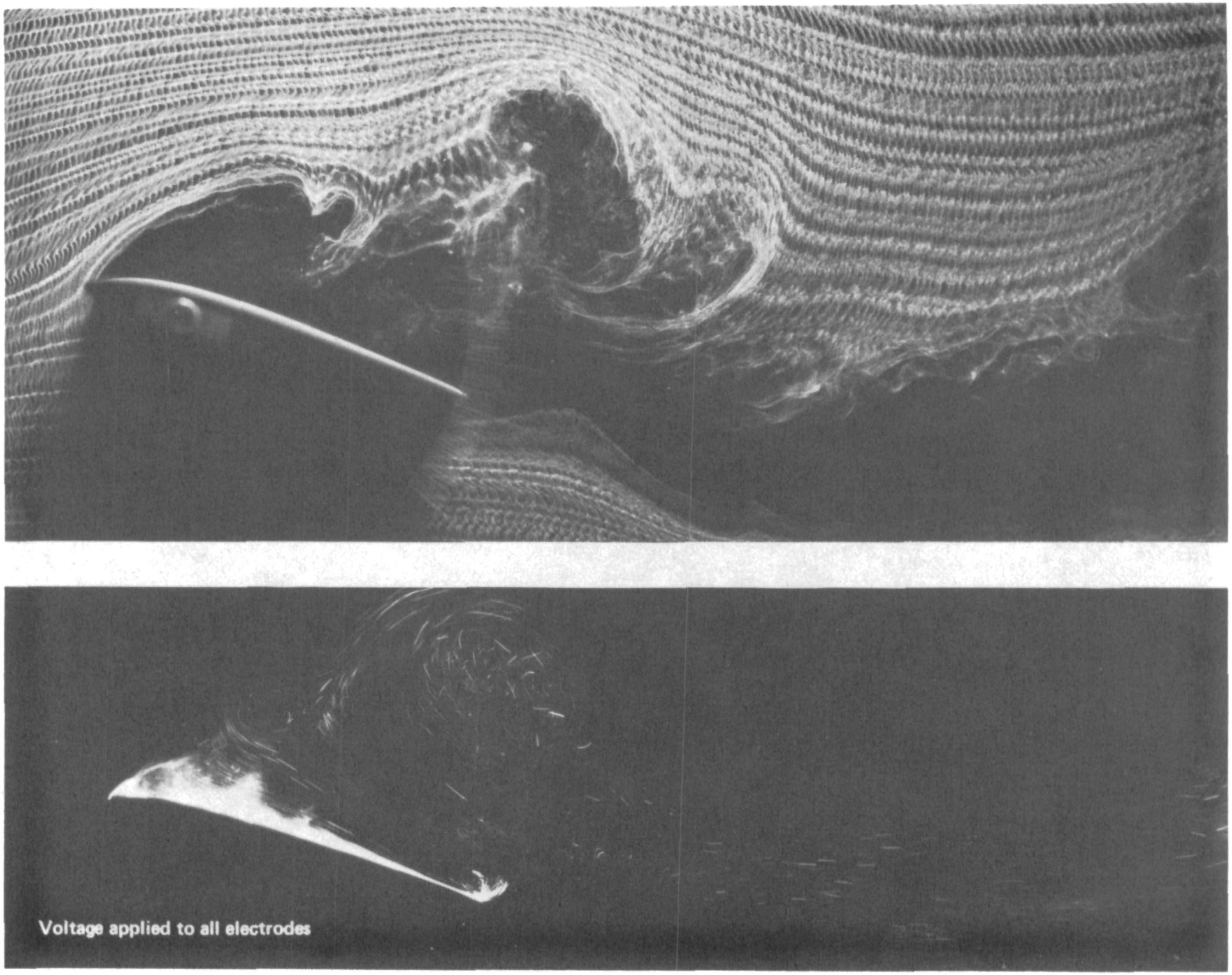

(p) $\omega t = 135°$ ($\alpha = 17.1°$)

Figure 11.- Continued.

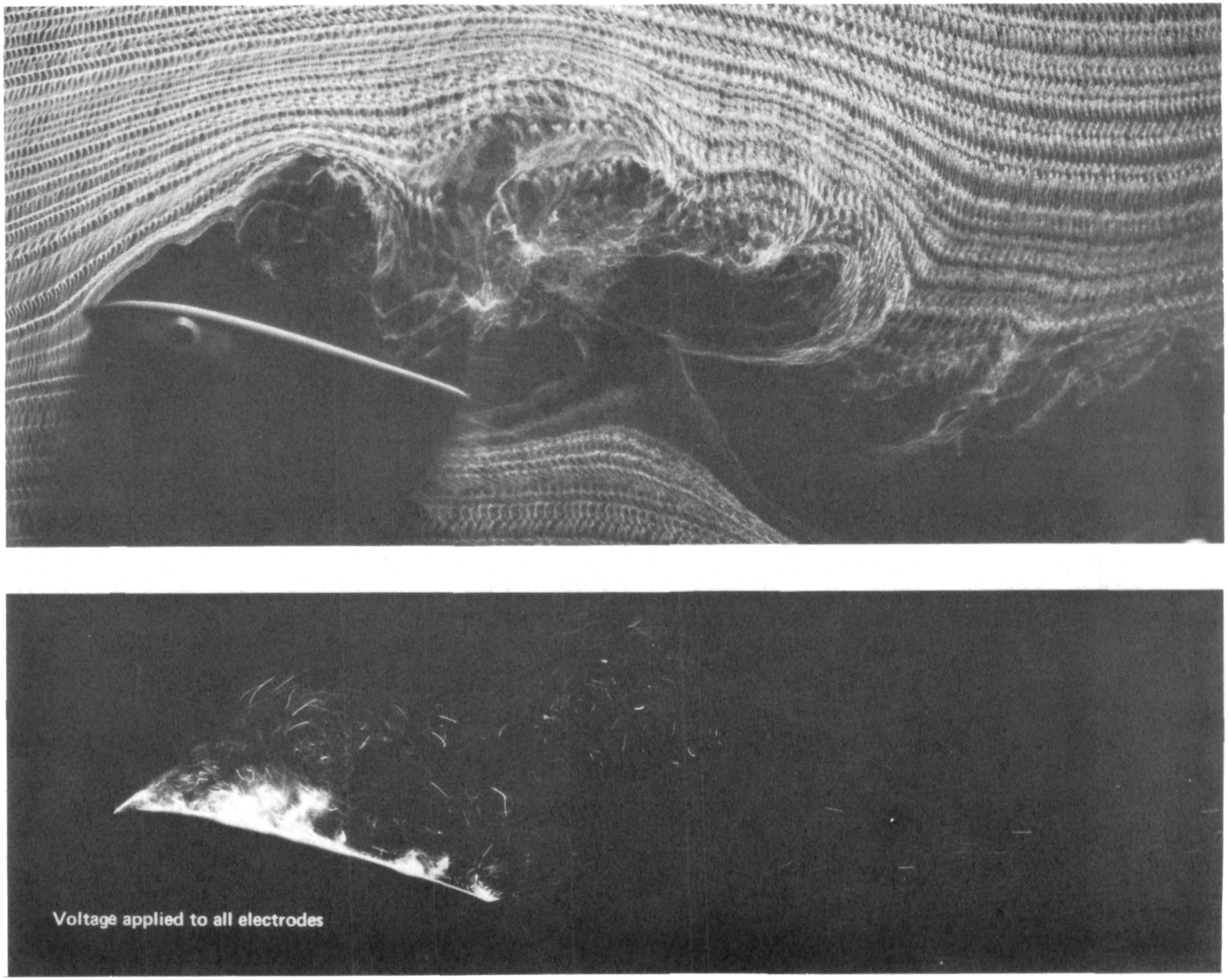

(q) ωt = 150° (α = 15.0°)

Figure 11.- Continued.

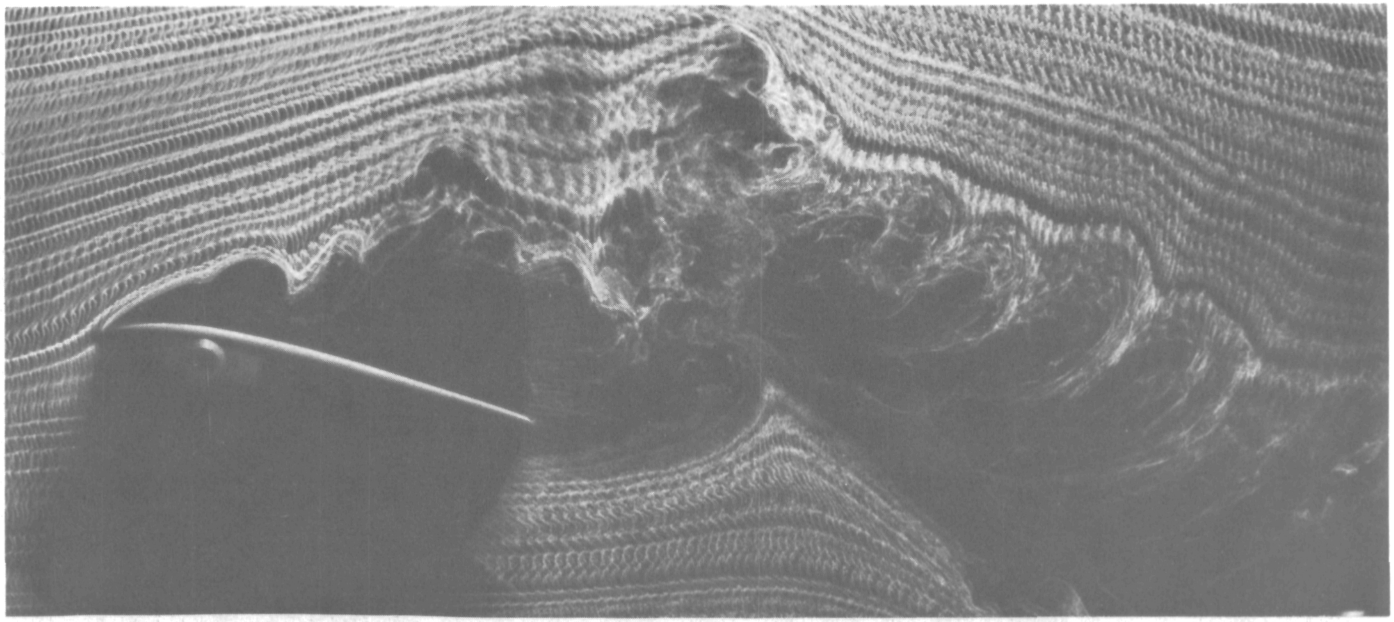

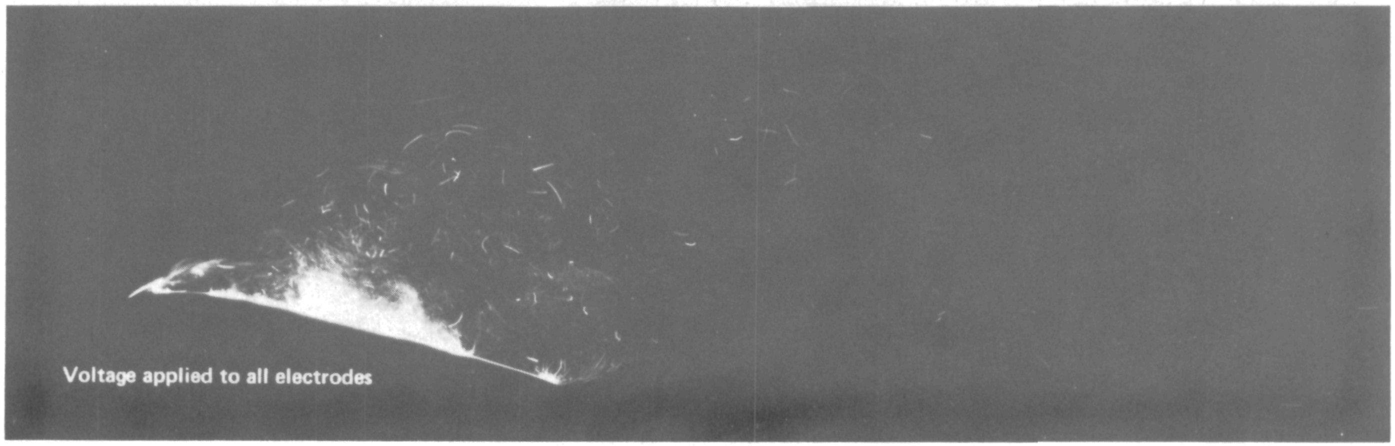

(r) $\omega t = 165°$ ($\alpha = 12.6°$)

Figure 11.- Continued.

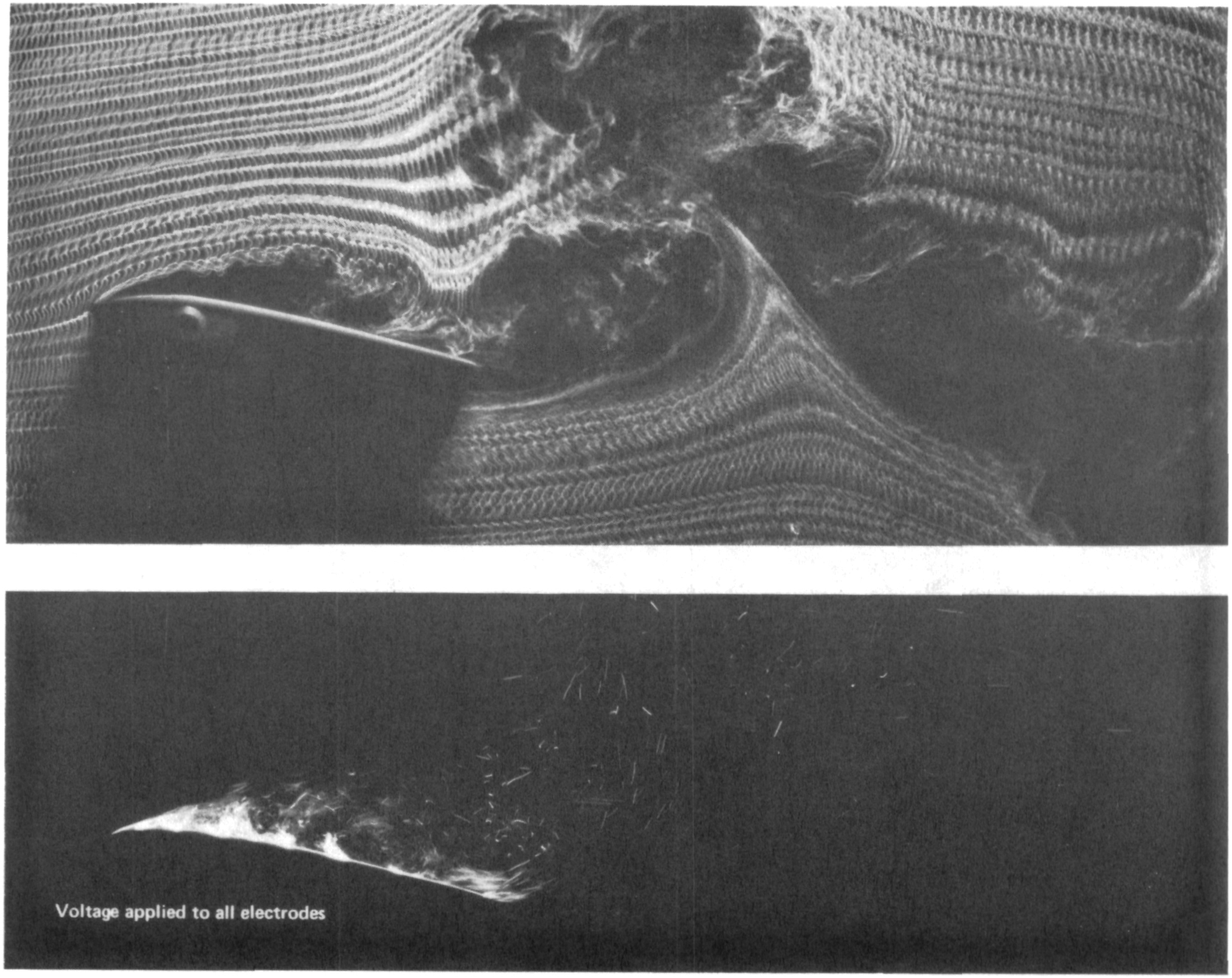

(s) $\omega t = 180°$ ($\alpha = 10.0°$)

Figure 11.- Continued.

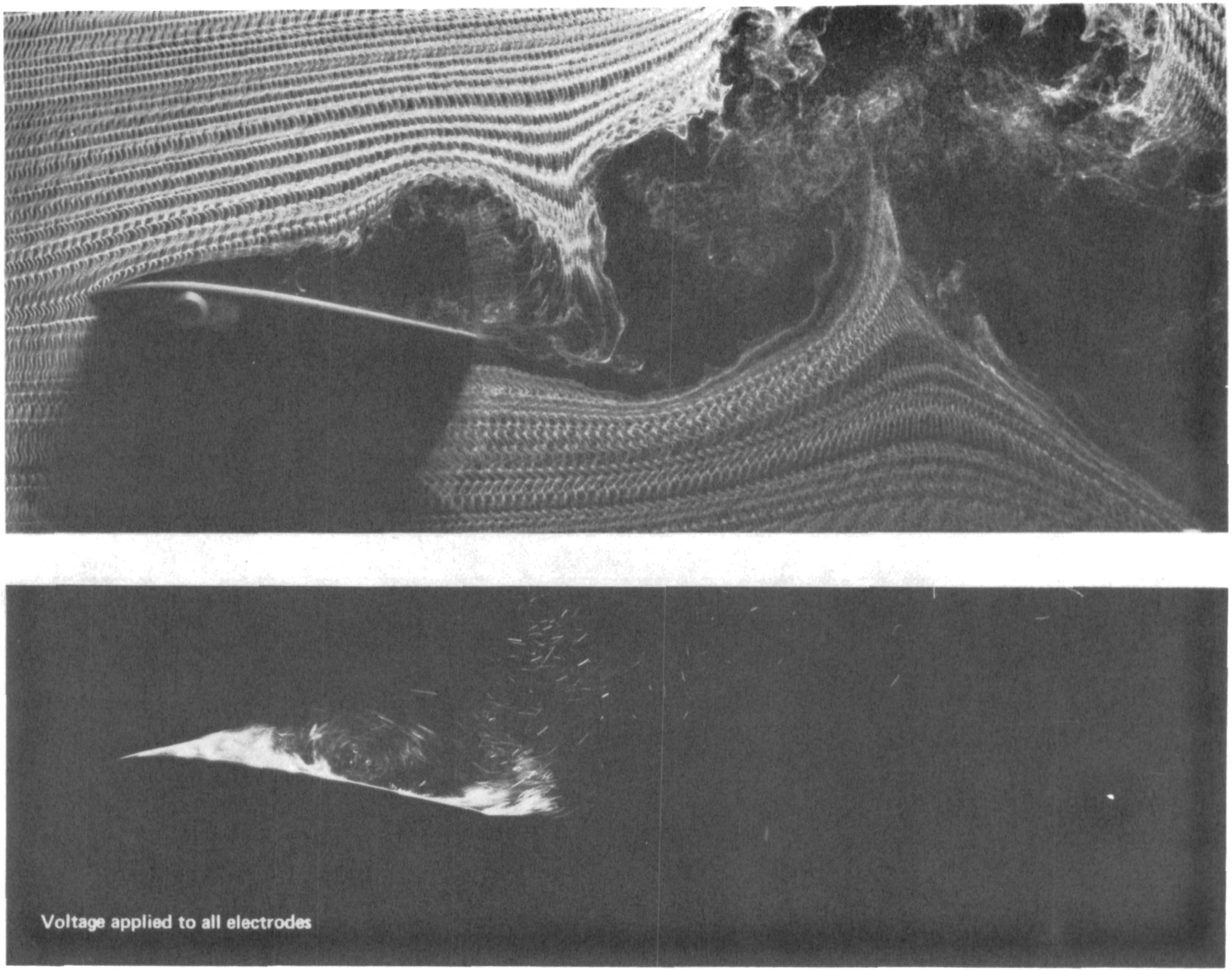

(t) $\omega t = 195°$ ($\alpha = 7.4°$)

Figure 11.- Continued.

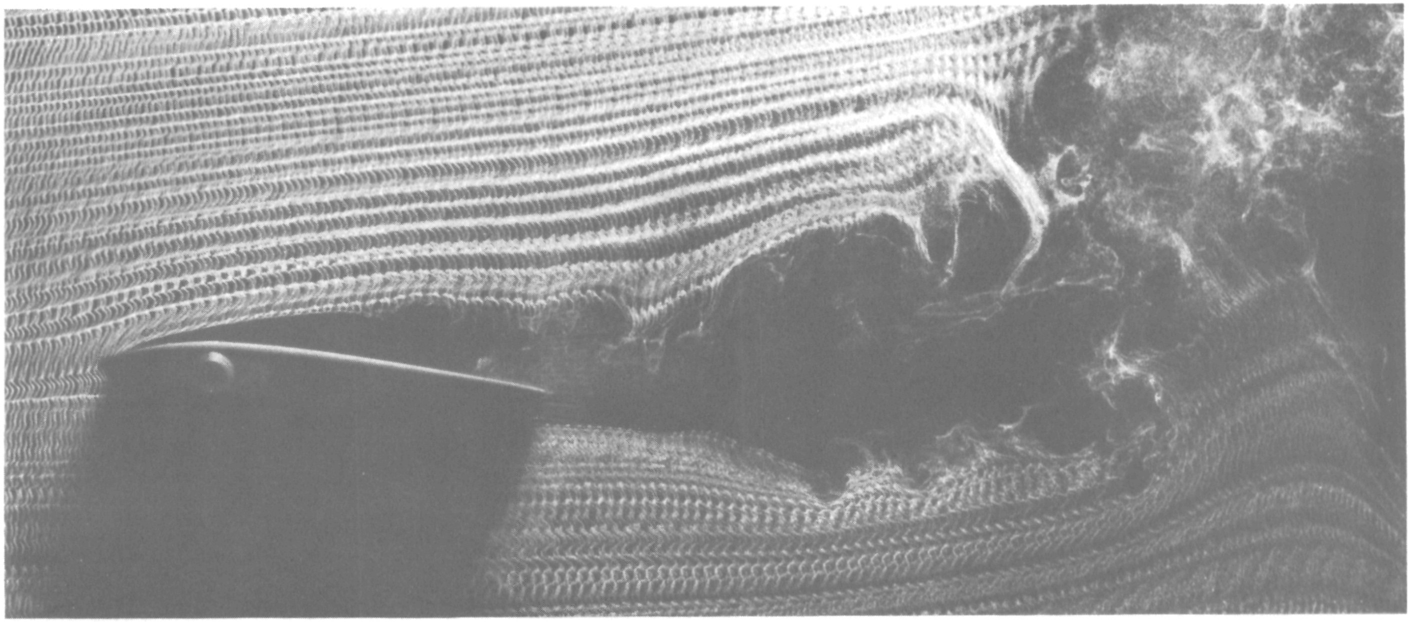

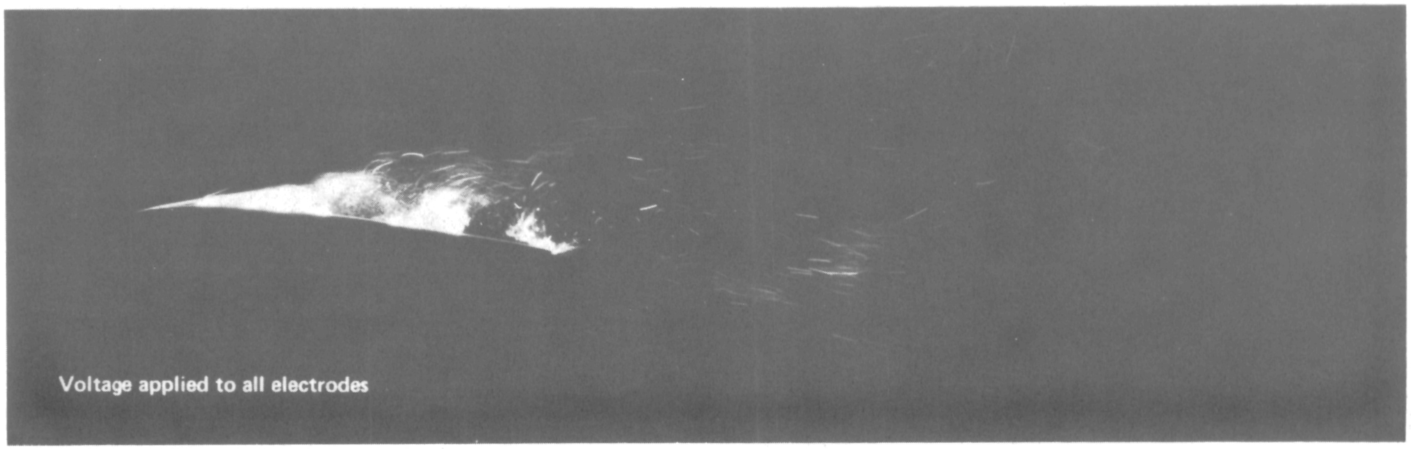

(u) $\omega t = 210°$ ($\alpha = 5.0°$)

Figure 11.- Continued.

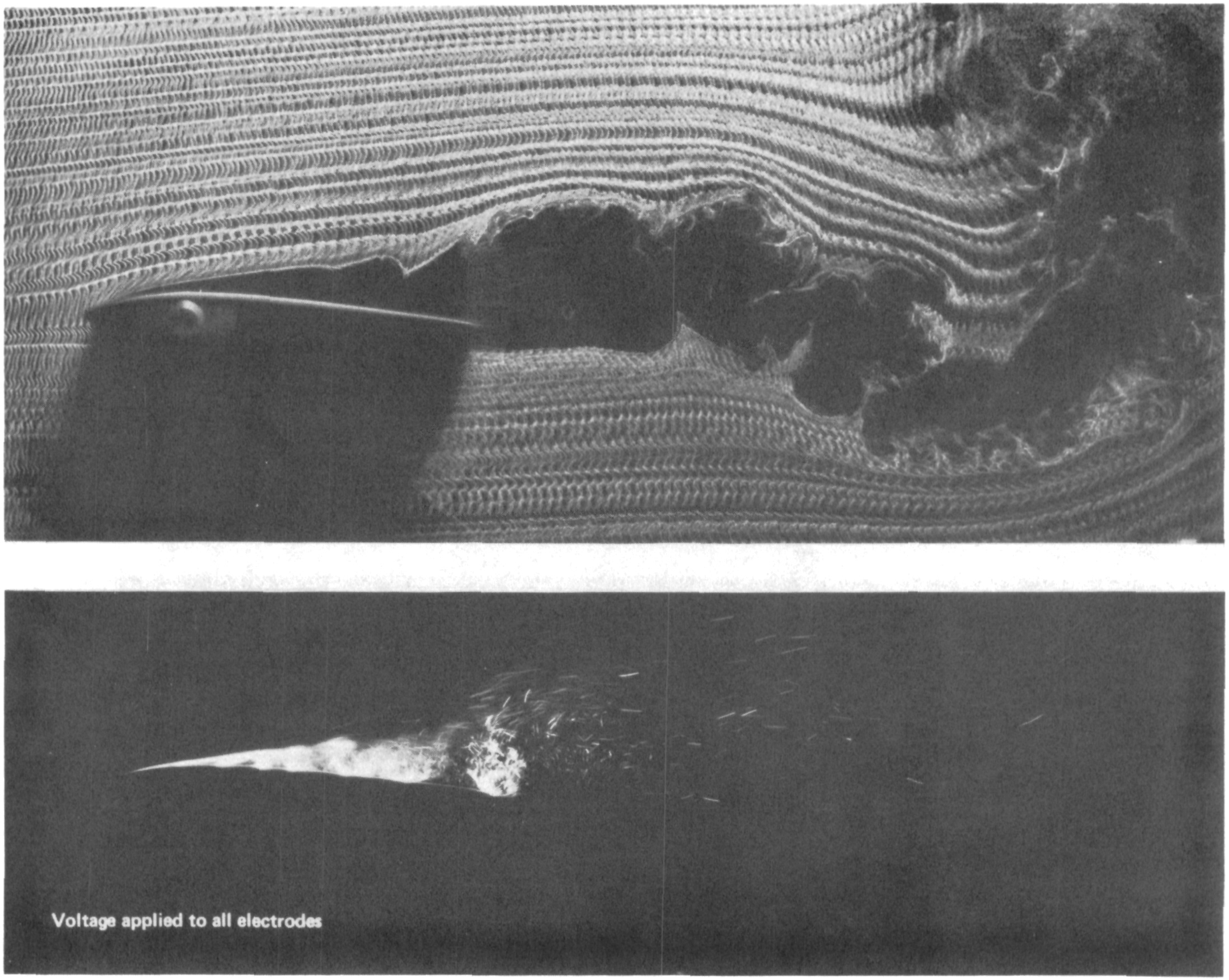

(v) $\omega t = 225°$ ($\alpha = 2.9°$)

Figure 11.- Continued.

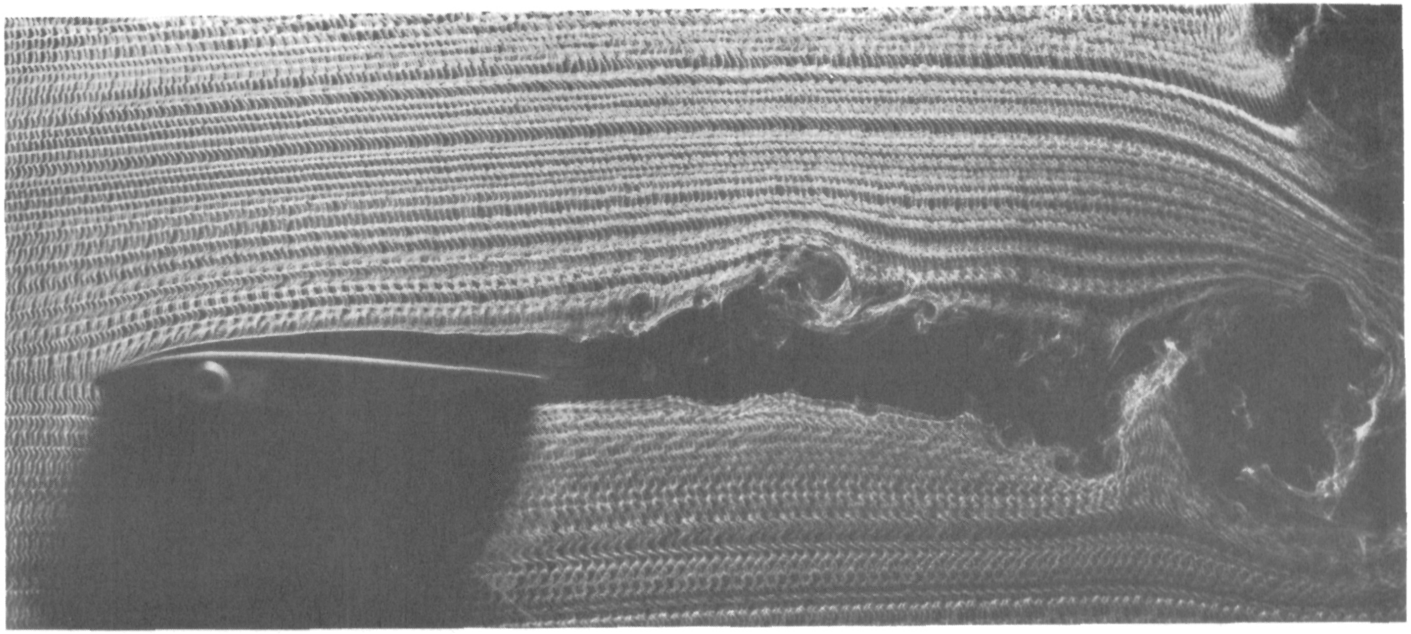

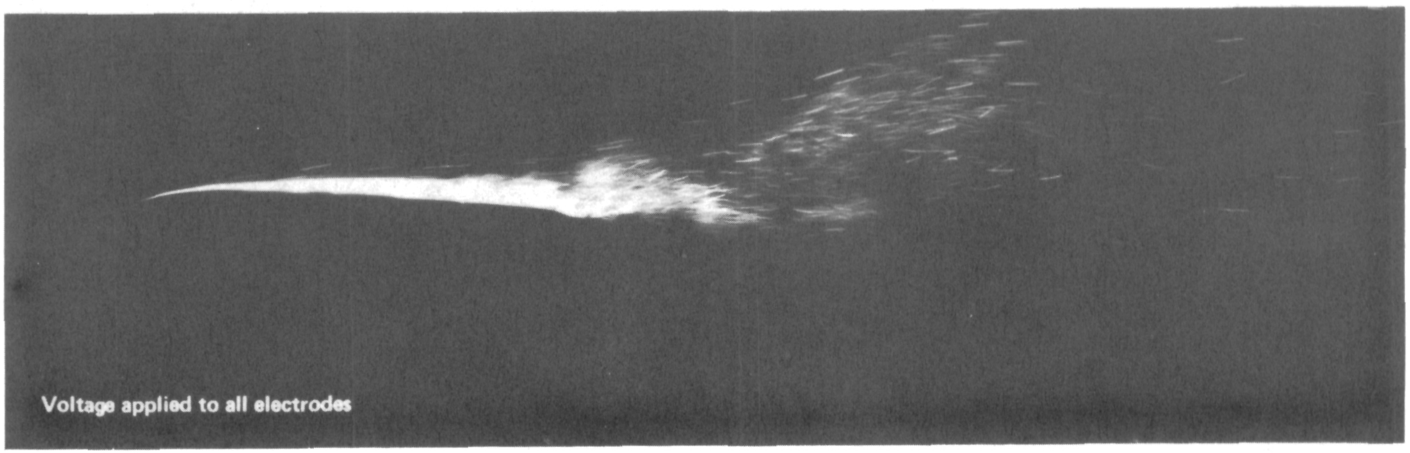

(w) $\omega t = 240°$ ($\alpha = 1.3°$)

Figure 11.- Continued.

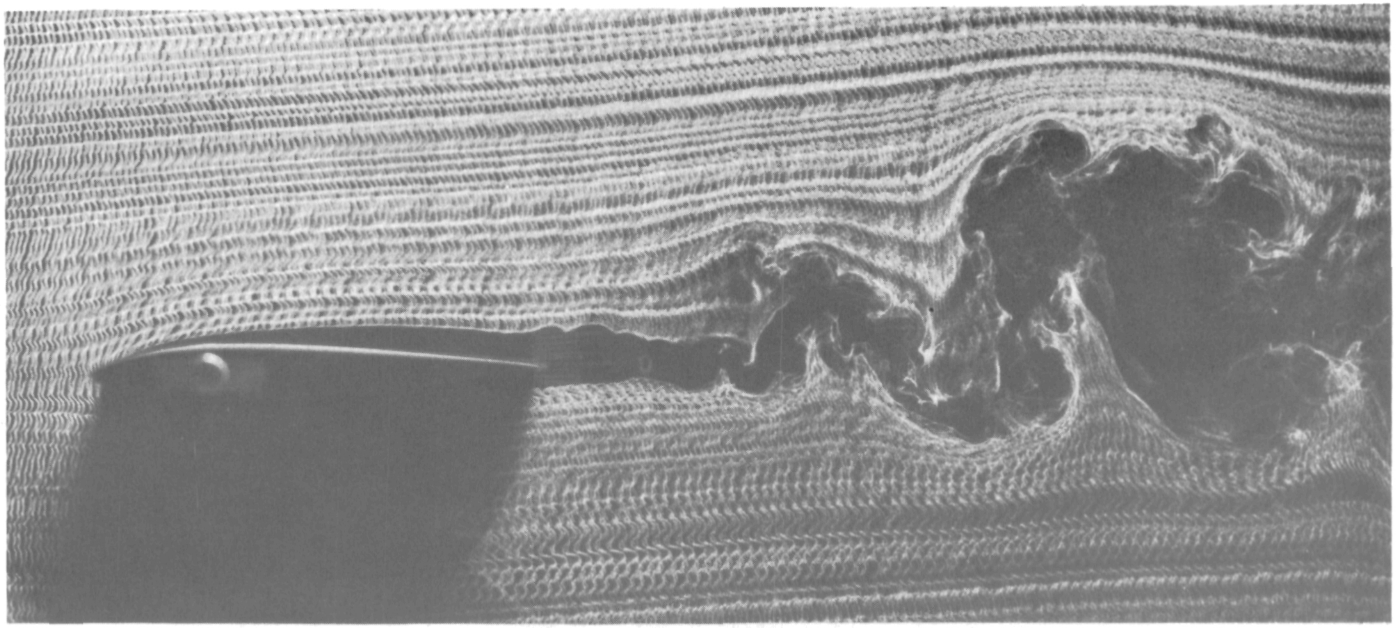

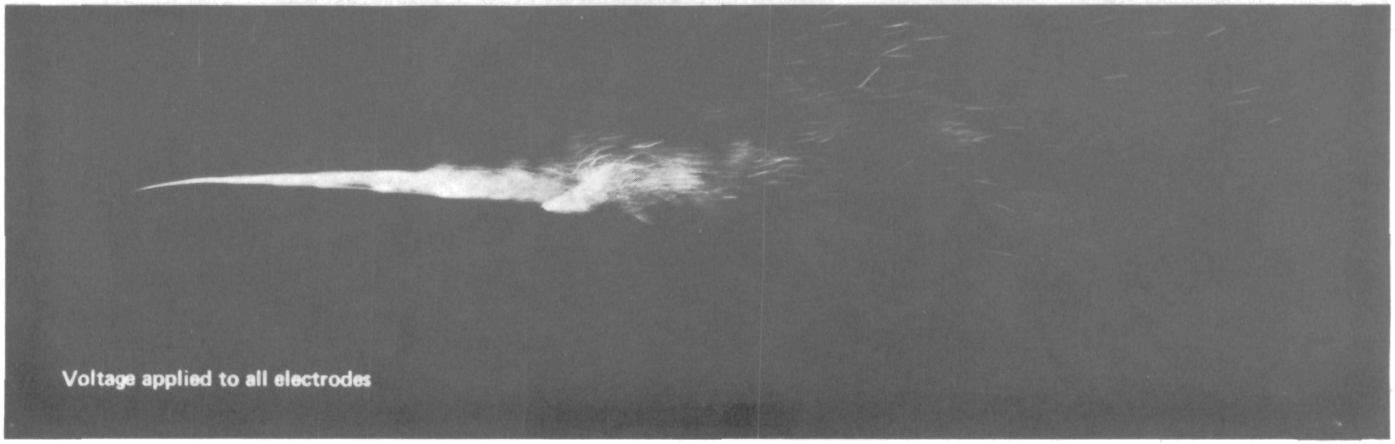

(x) $\omega t = 255°$ ($\alpha = 0.3°$)

Figure 11.- Concluded.

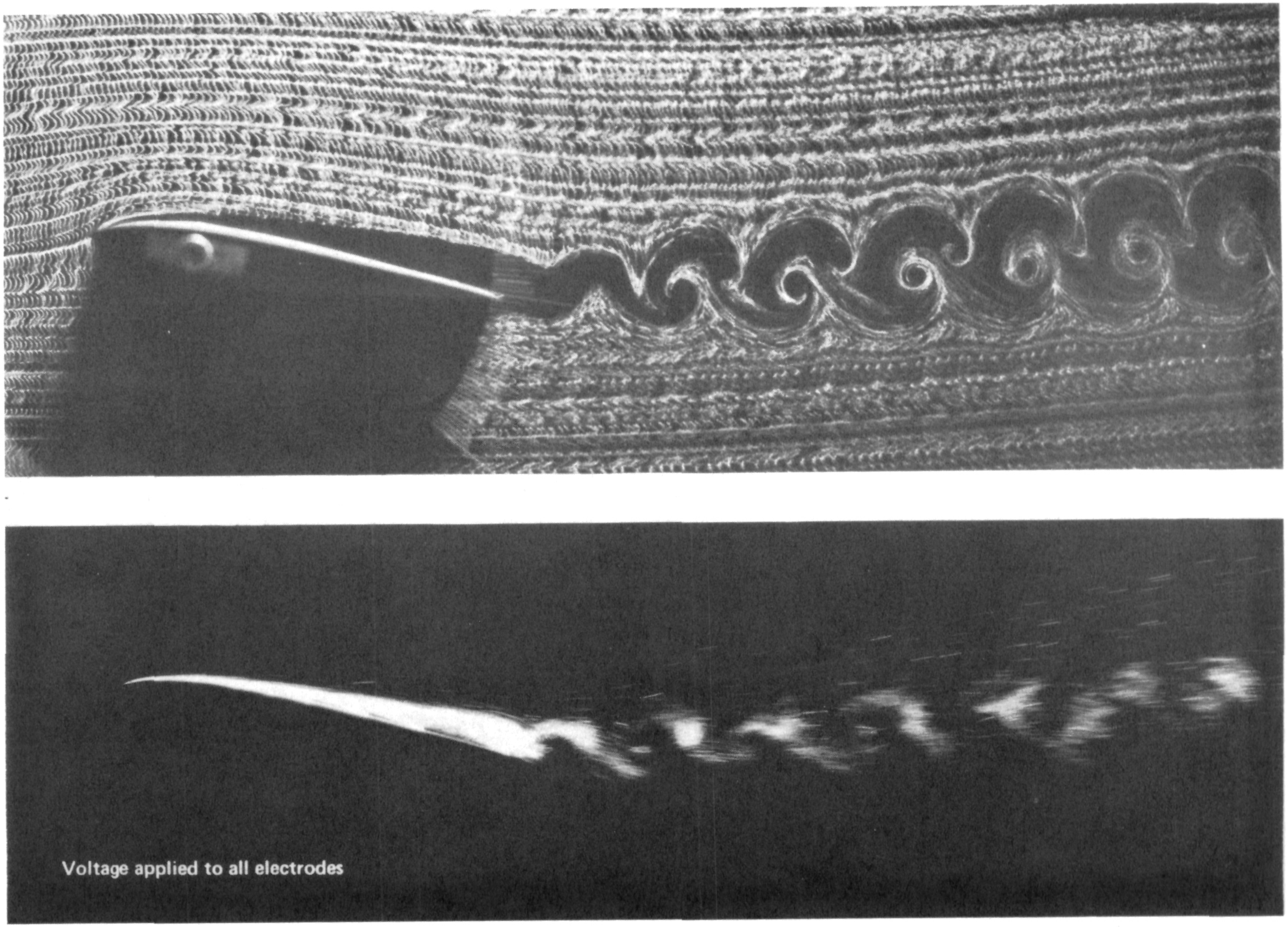

(a) $\omega t = 0°$ ($\alpha = 10.0°$)

Figure 12.- Detailed flow patterns every 4° of azimuth during the period of dynamic stall.

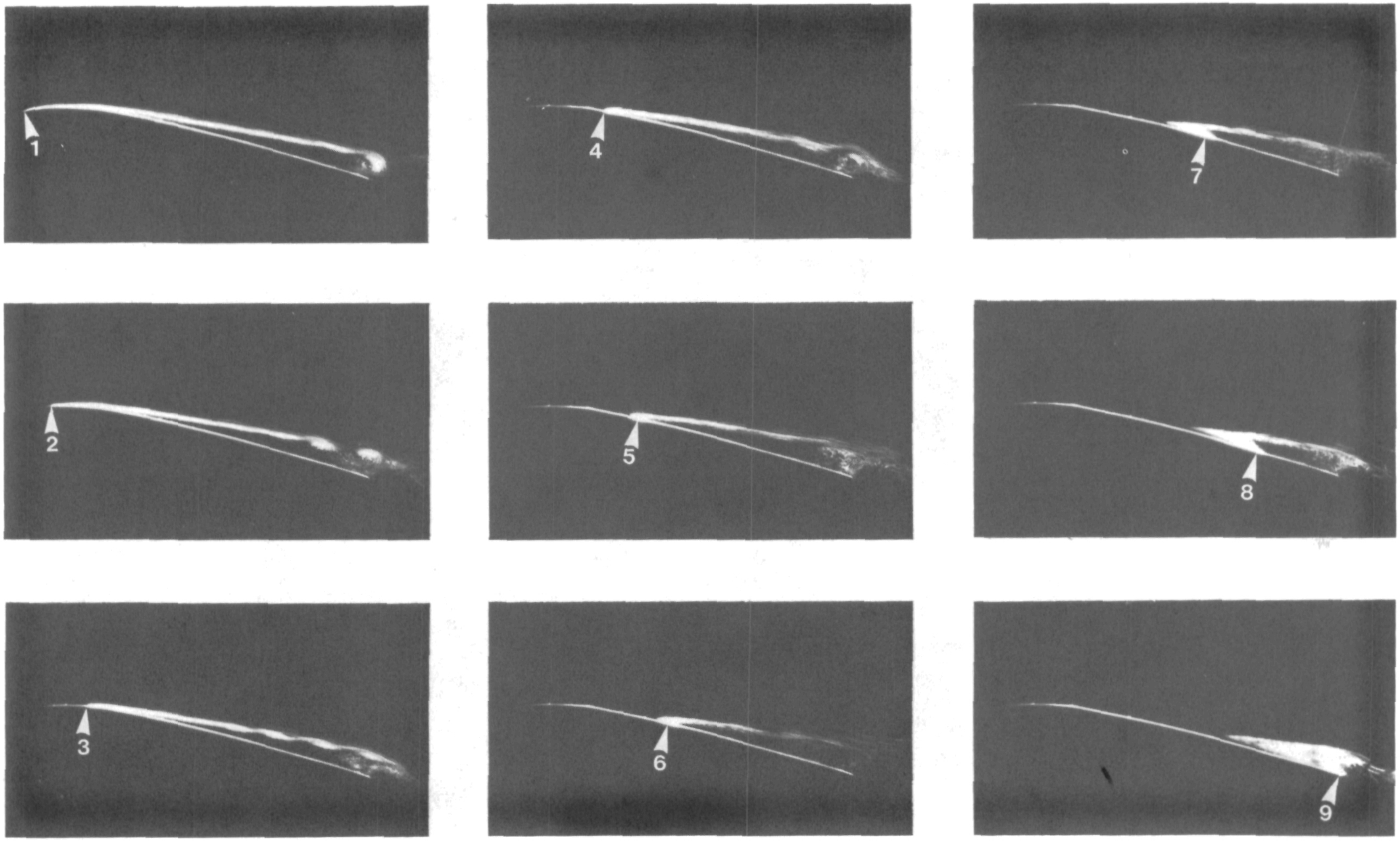

(a) Concluded.

Figure 12.- Continued.

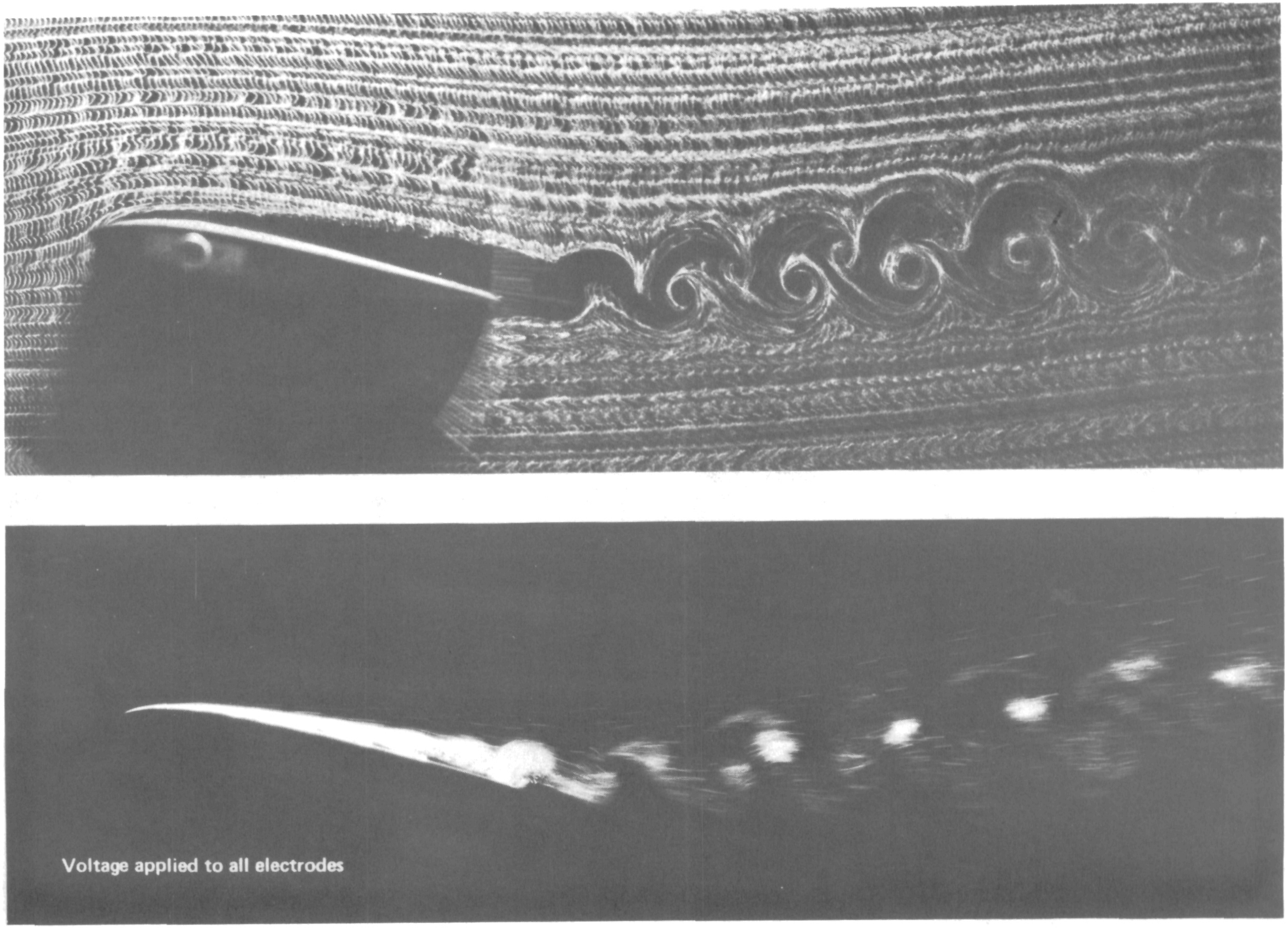

(b) $\omega t = 4°$ ($\alpha = 10.7°$)

Figure 12.- Continued.

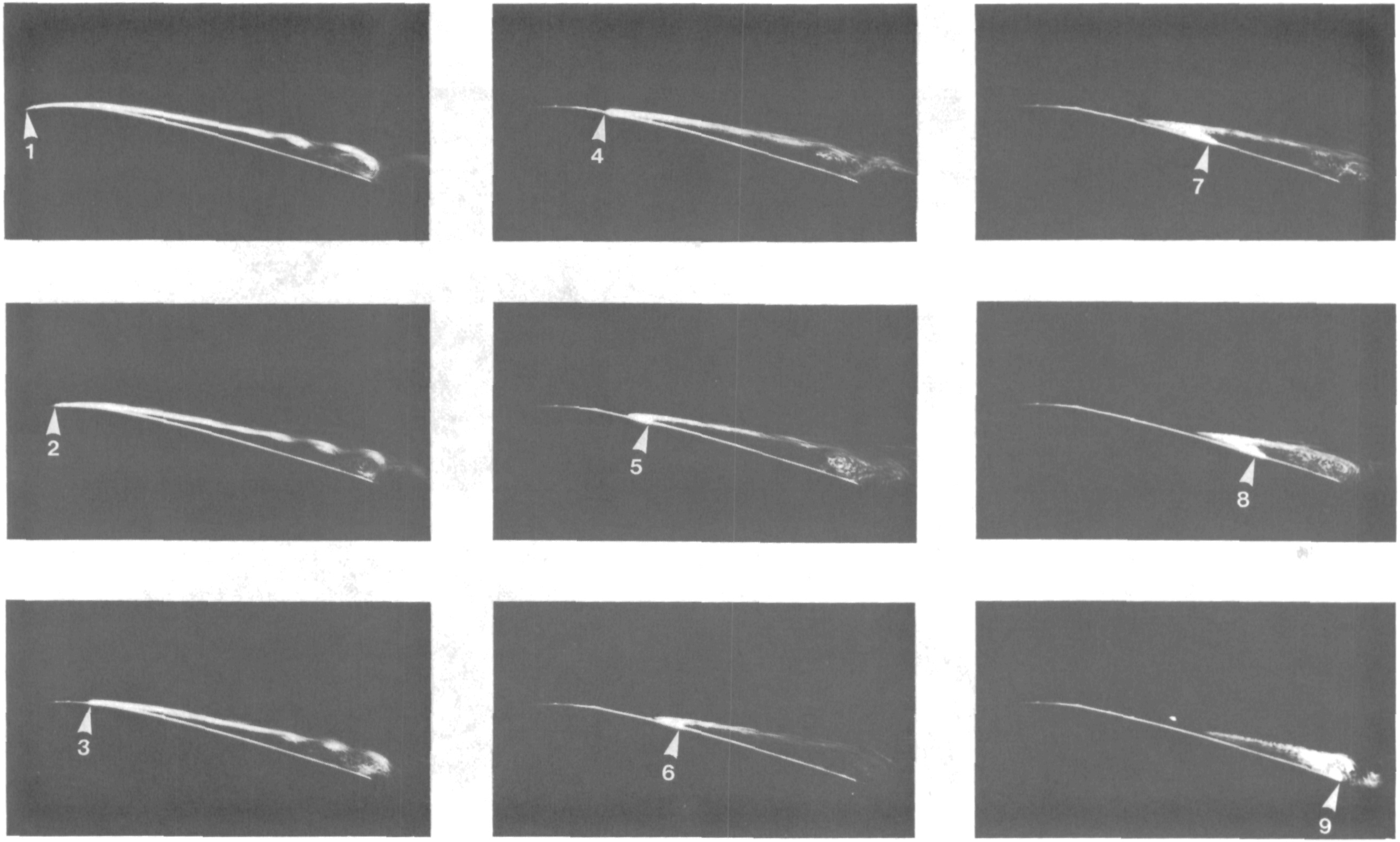

(b) Concluded.

Figure 12.- Continued.

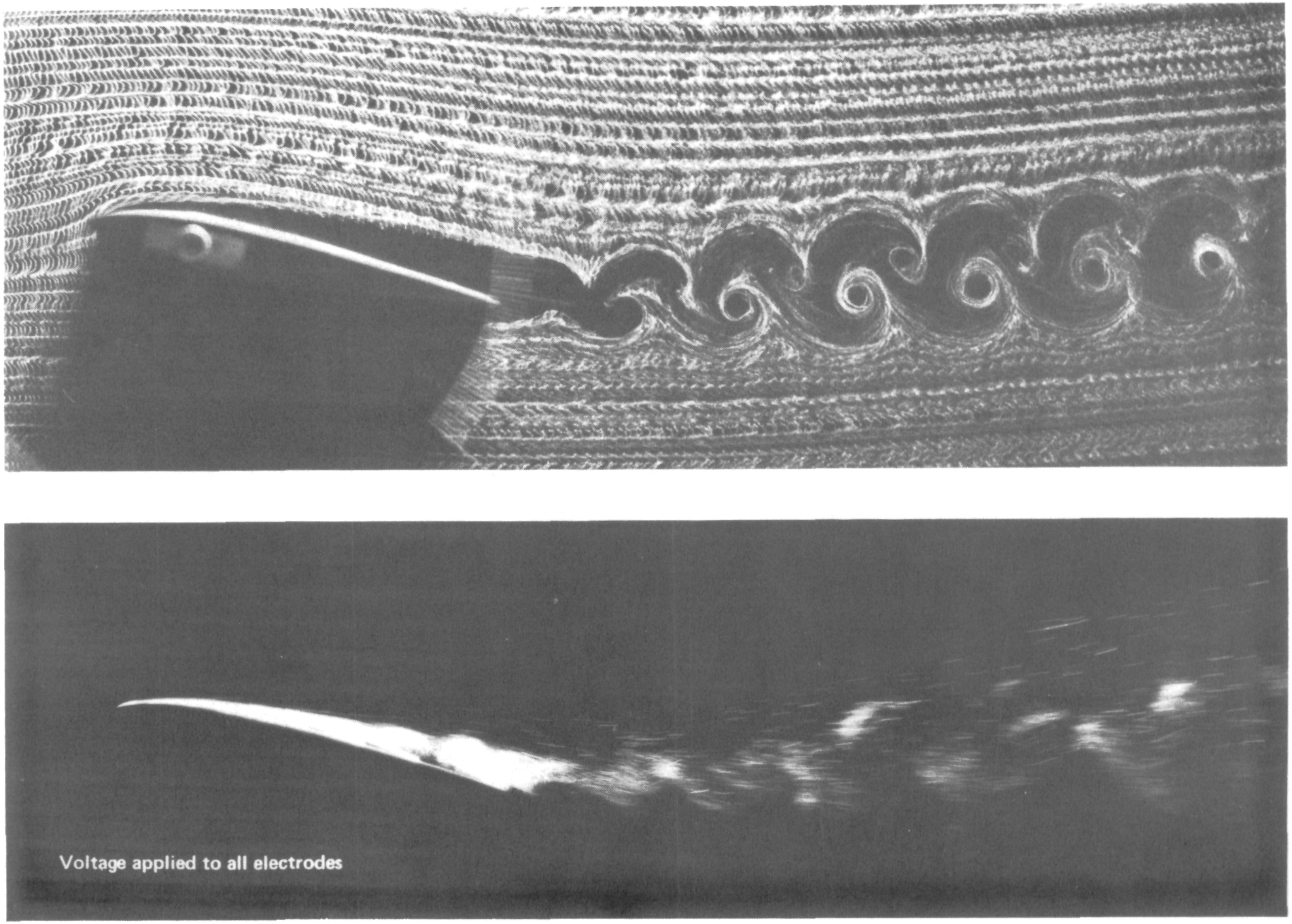

(c) $\omega t = 8°$ ($\alpha = 11.4°$)

Figure 12.- Continued.

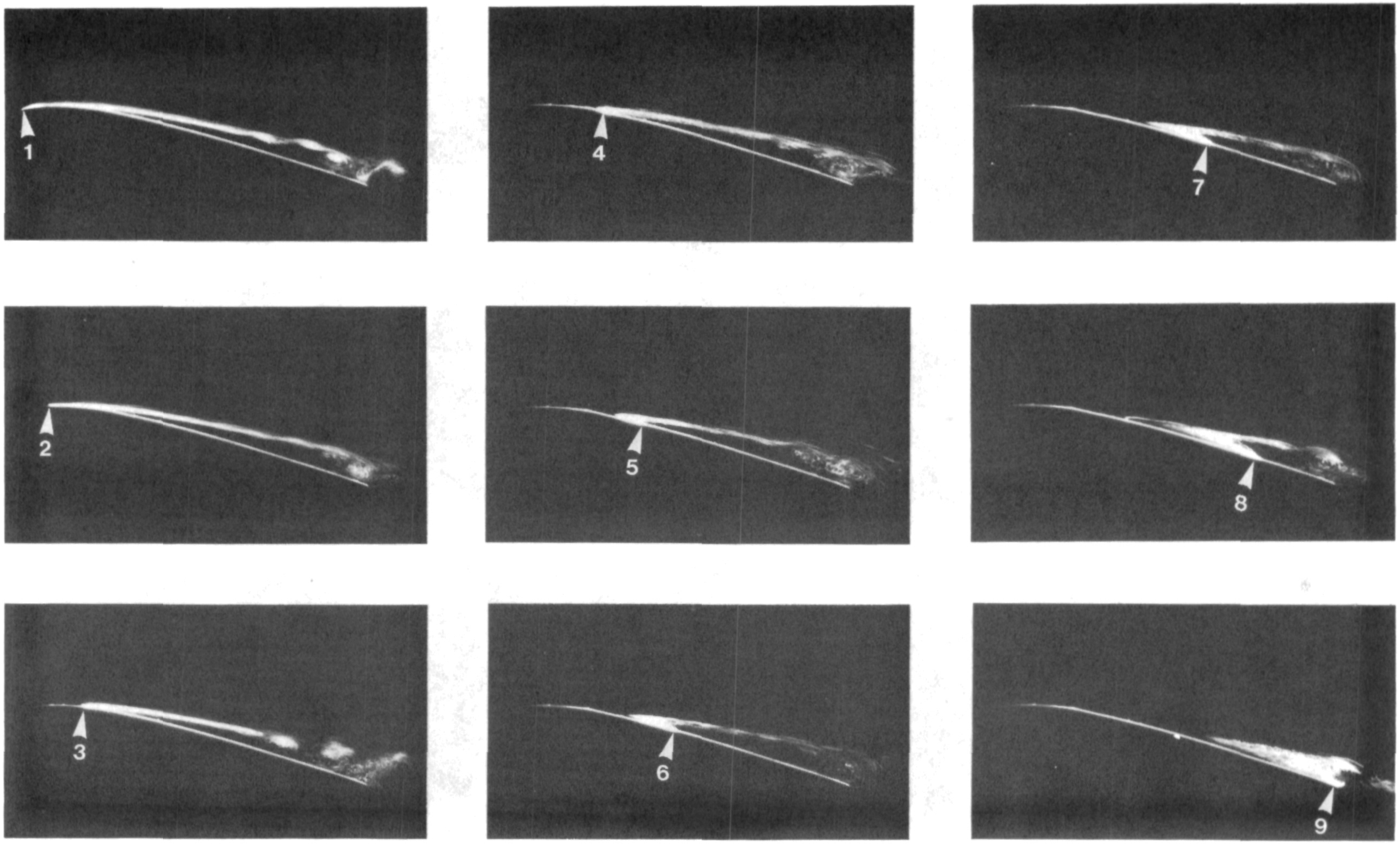

(c) Concluded.

Figure 12.- Continued.

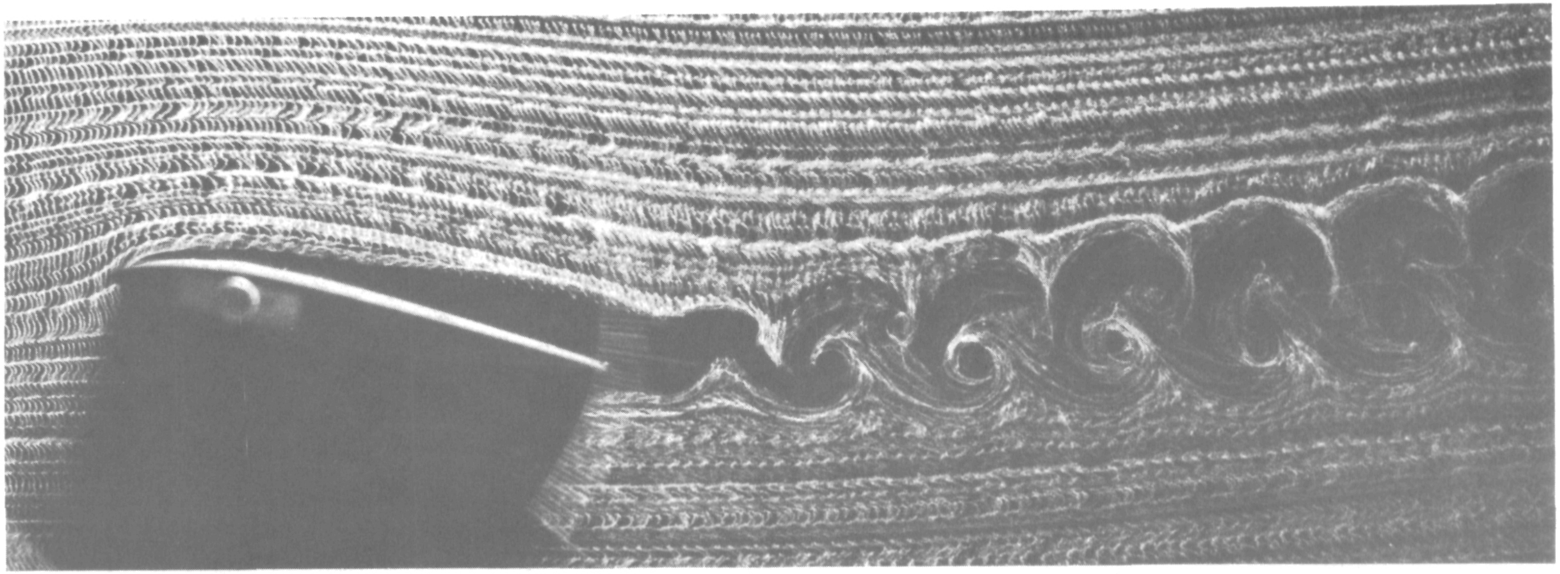

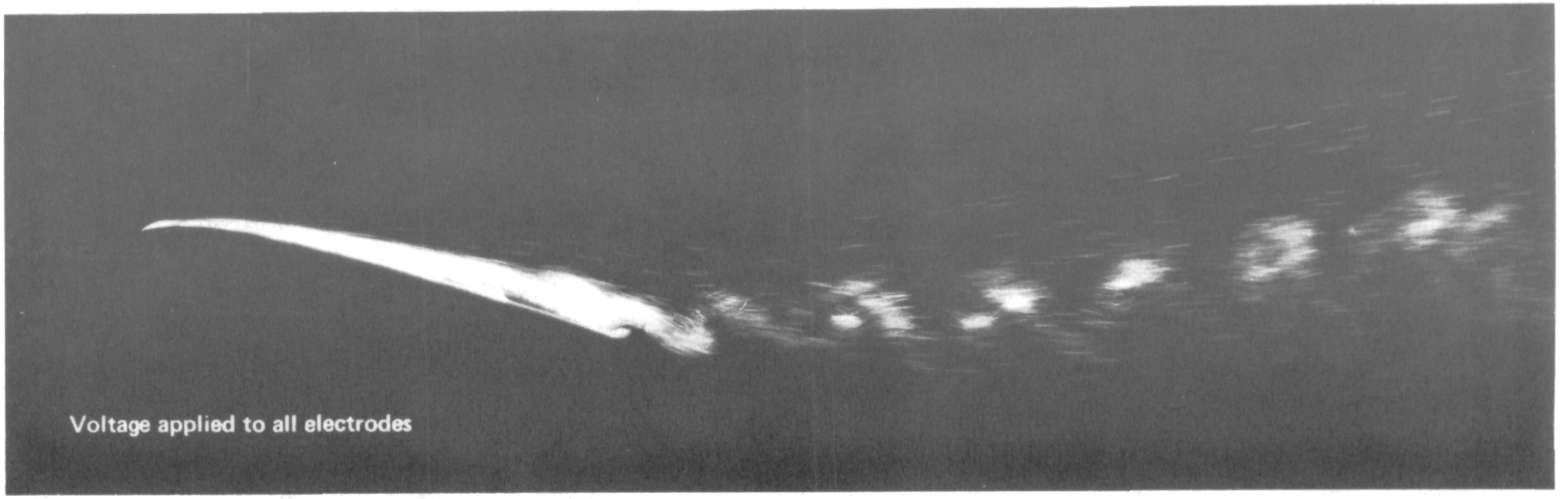

(d) ωt = 12° (α = 12.1°)

Figure 12.- Continued.

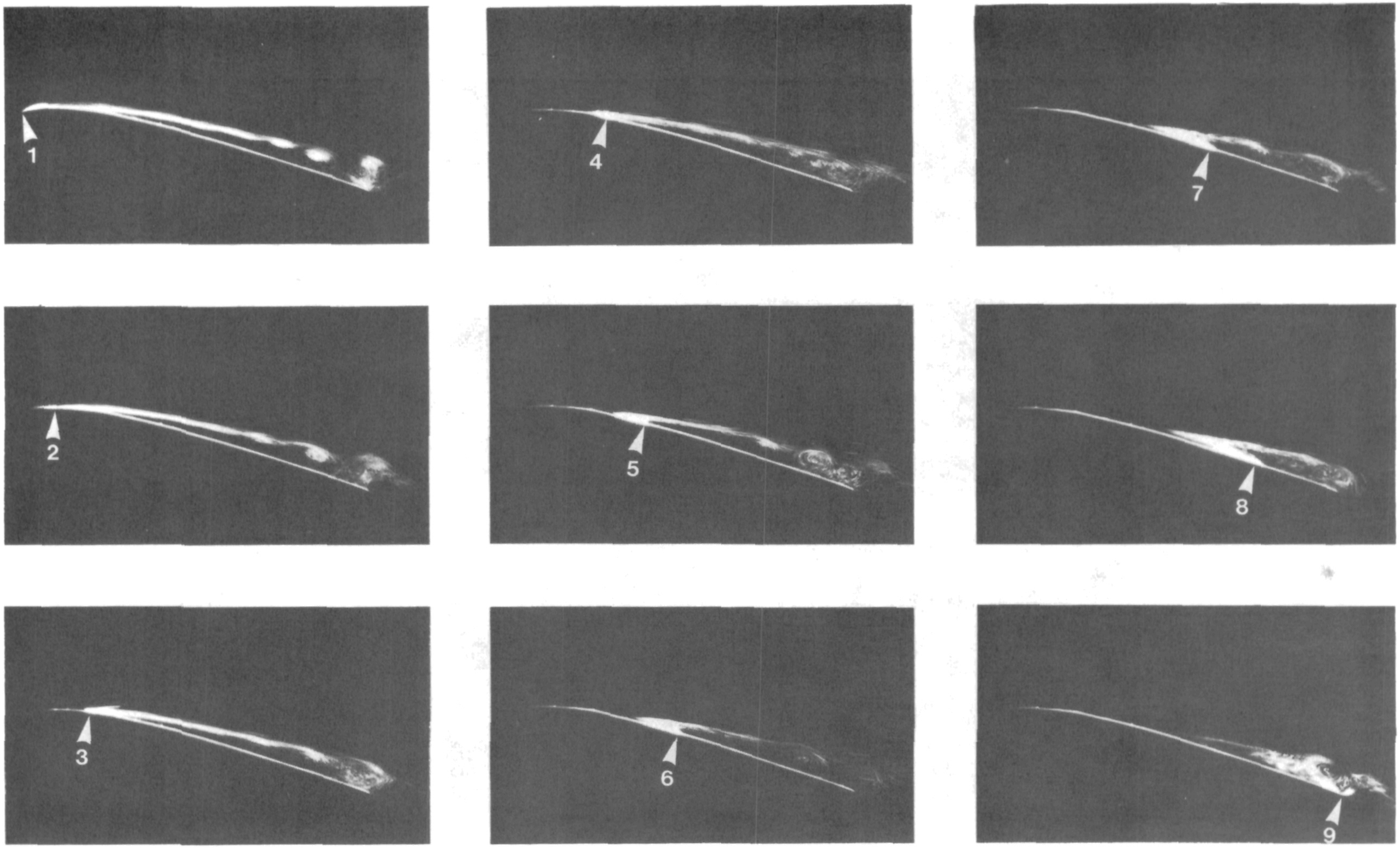

(d) Concluded.

Figure 12.- Continued.

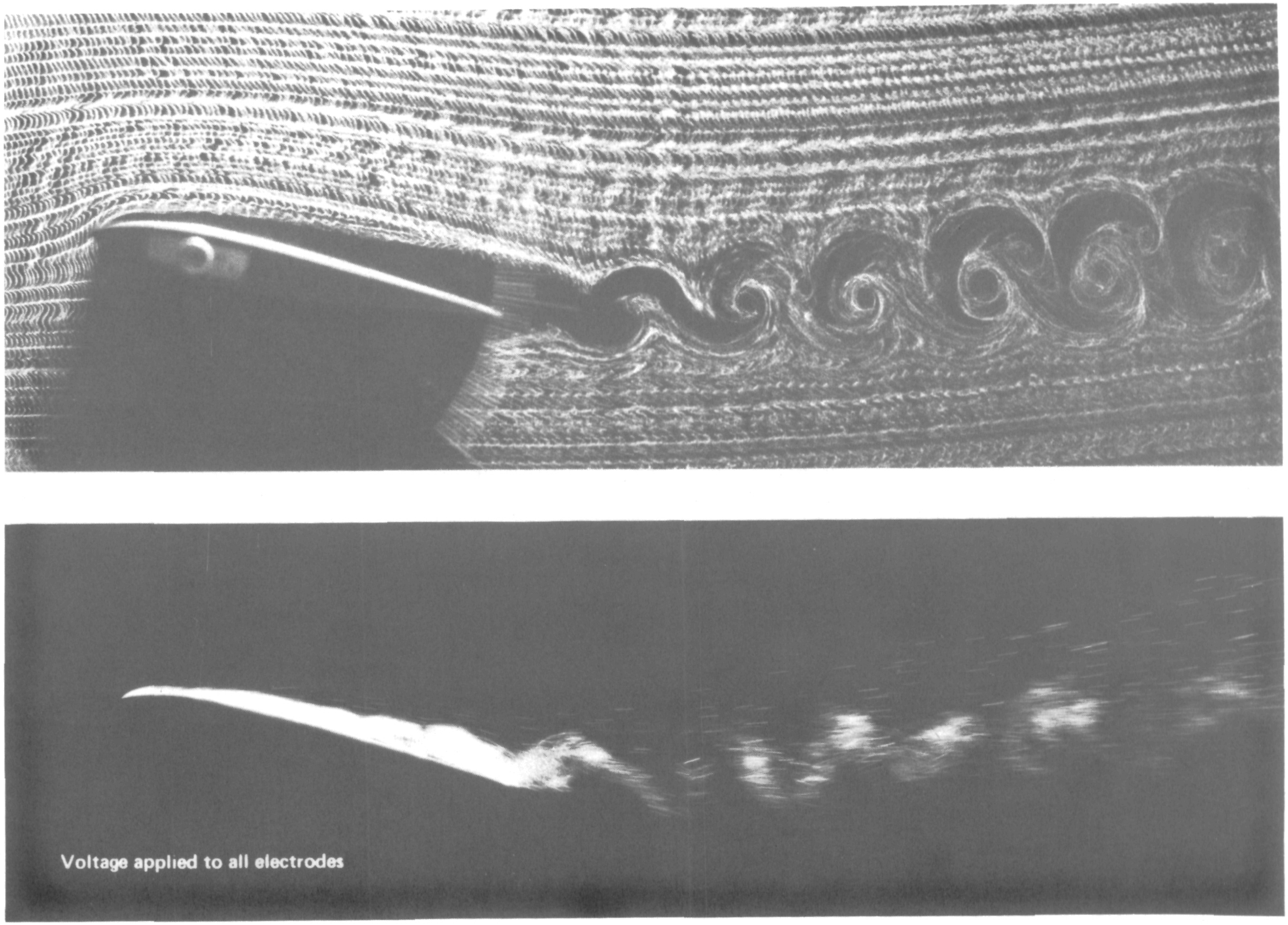

(e) $\omega t = 16°$ ($\alpha = 12.8°$)

Figure 12.- Continued.

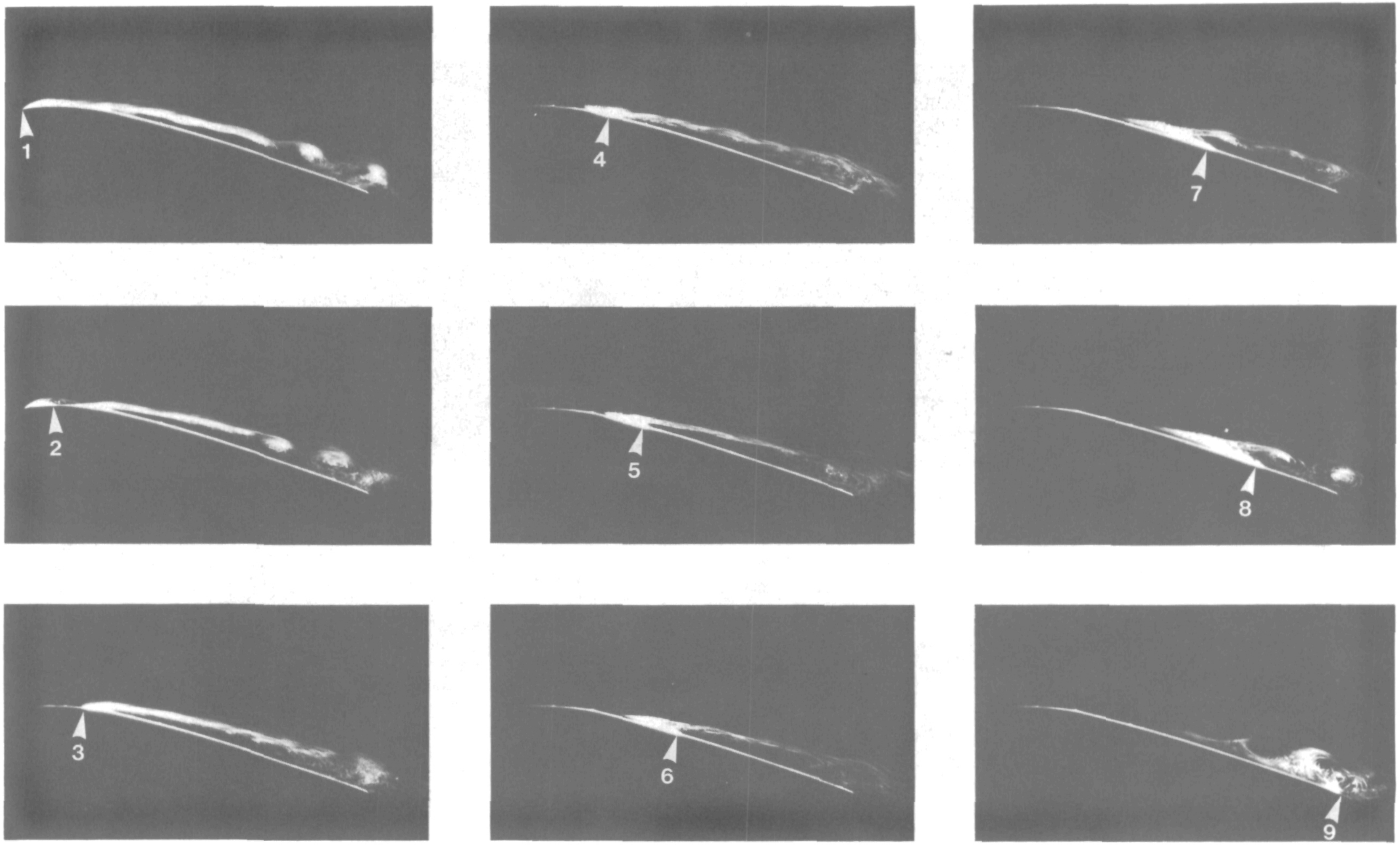

(e) Concluded.

Figure 12.- Continued.

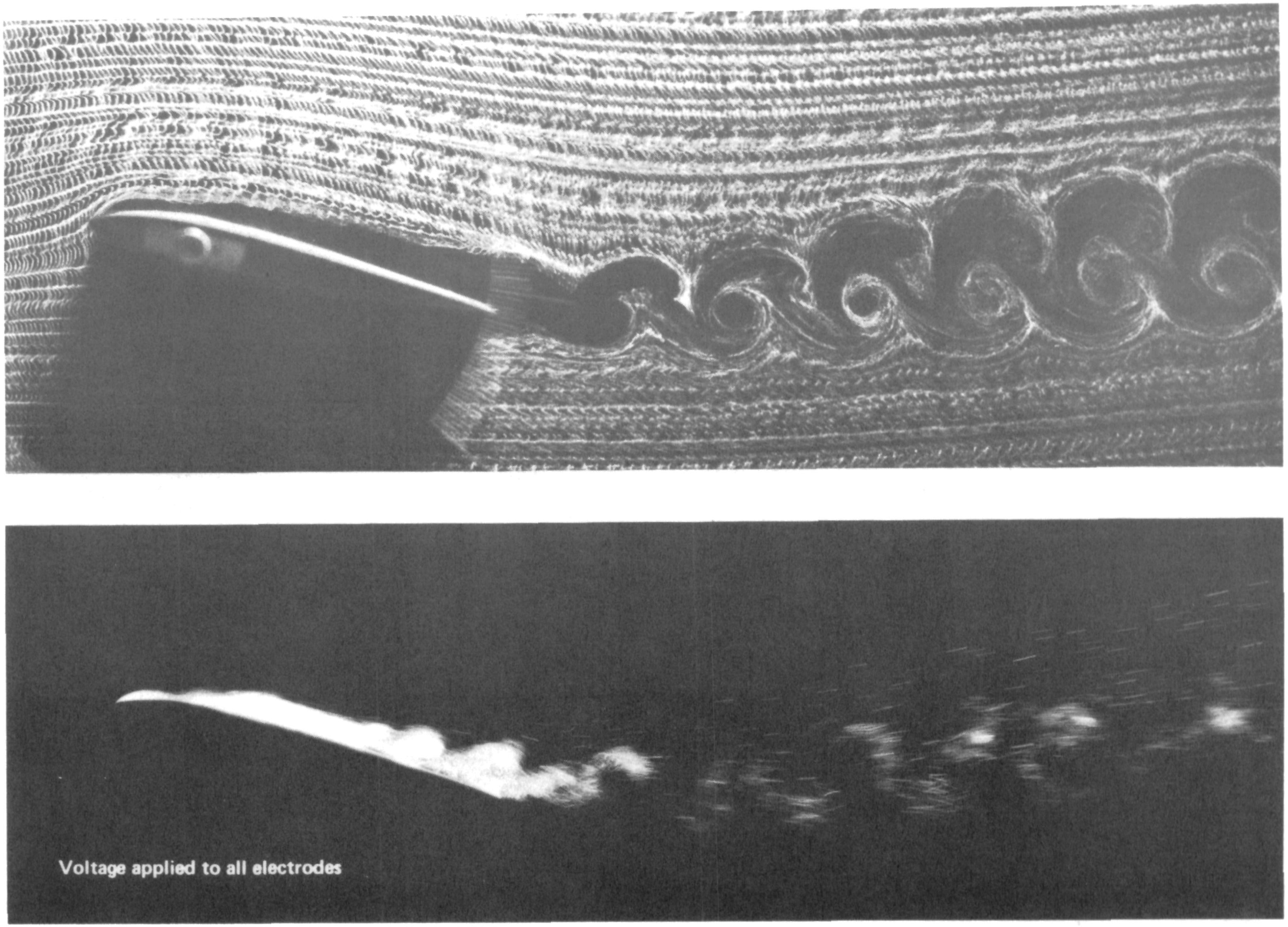

(f) $\omega t = 20°$ ($\alpha = 13.4°$)

Figure 12.- Continued.

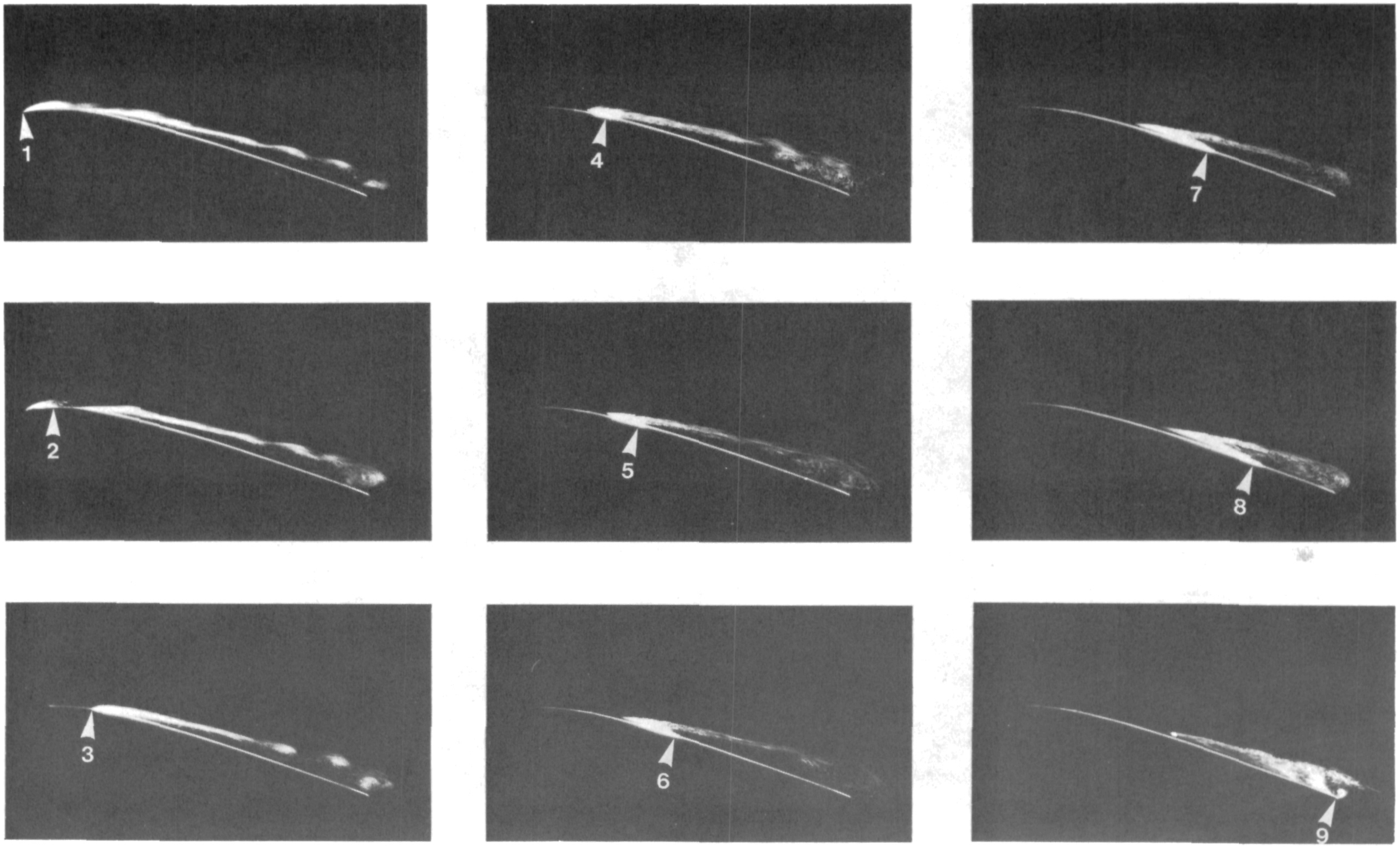

(f) Concluded.

Figure 12.- Continued.

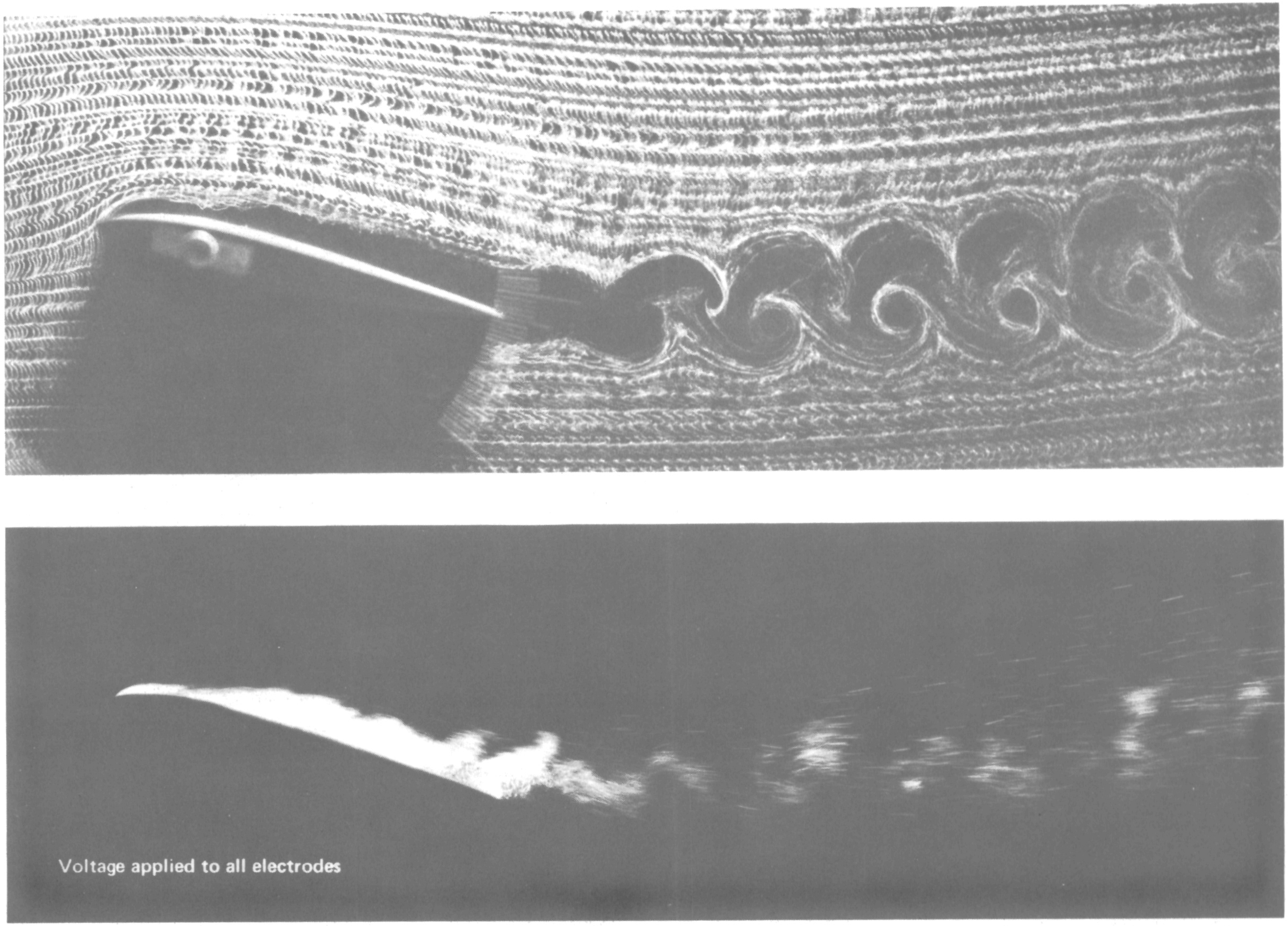

(g) $\omega t = 24°$ ($\alpha = 14.1°$)

Figure 12.- Continued.

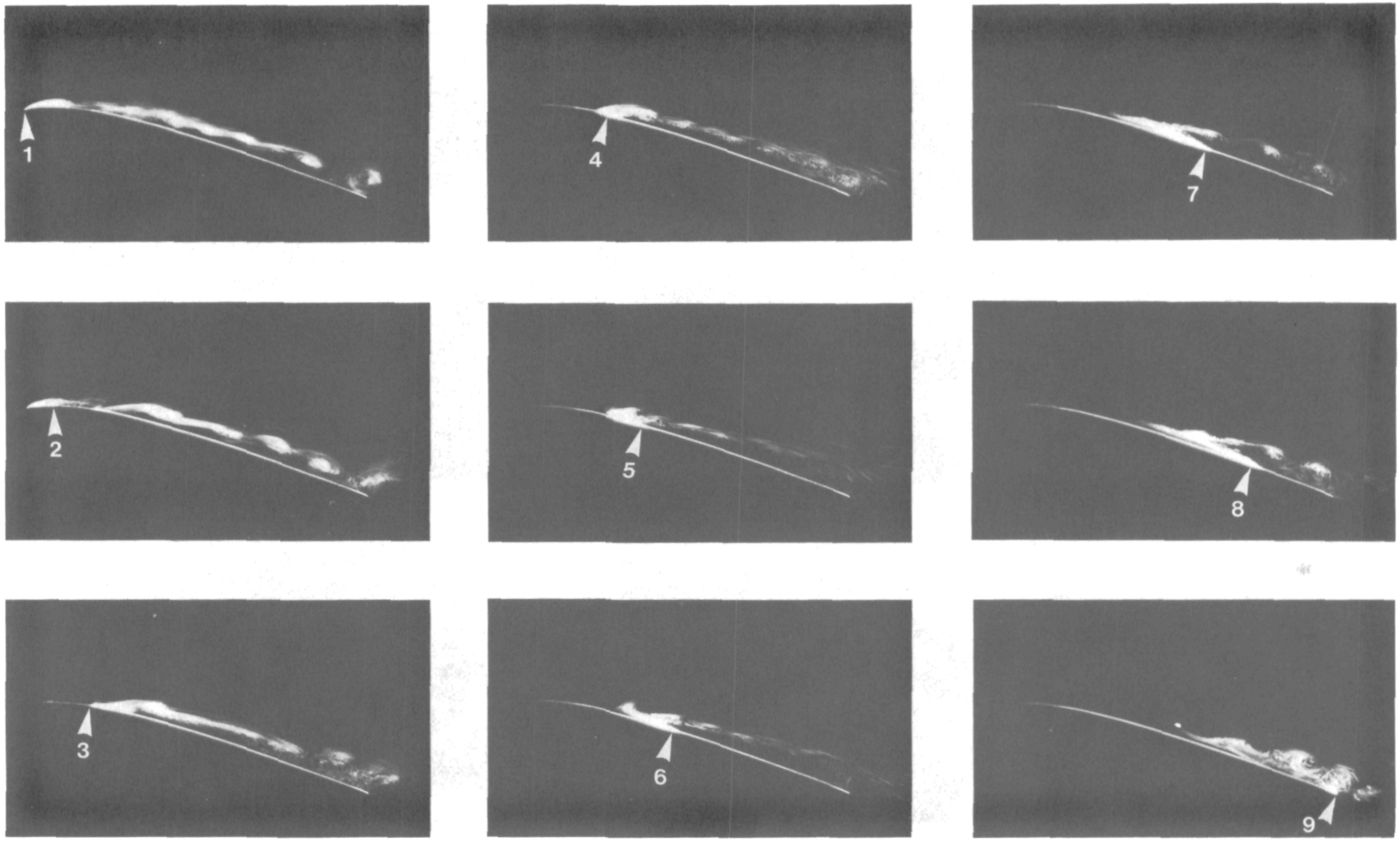

(g) Concluded.

Figure 12.- Continued.

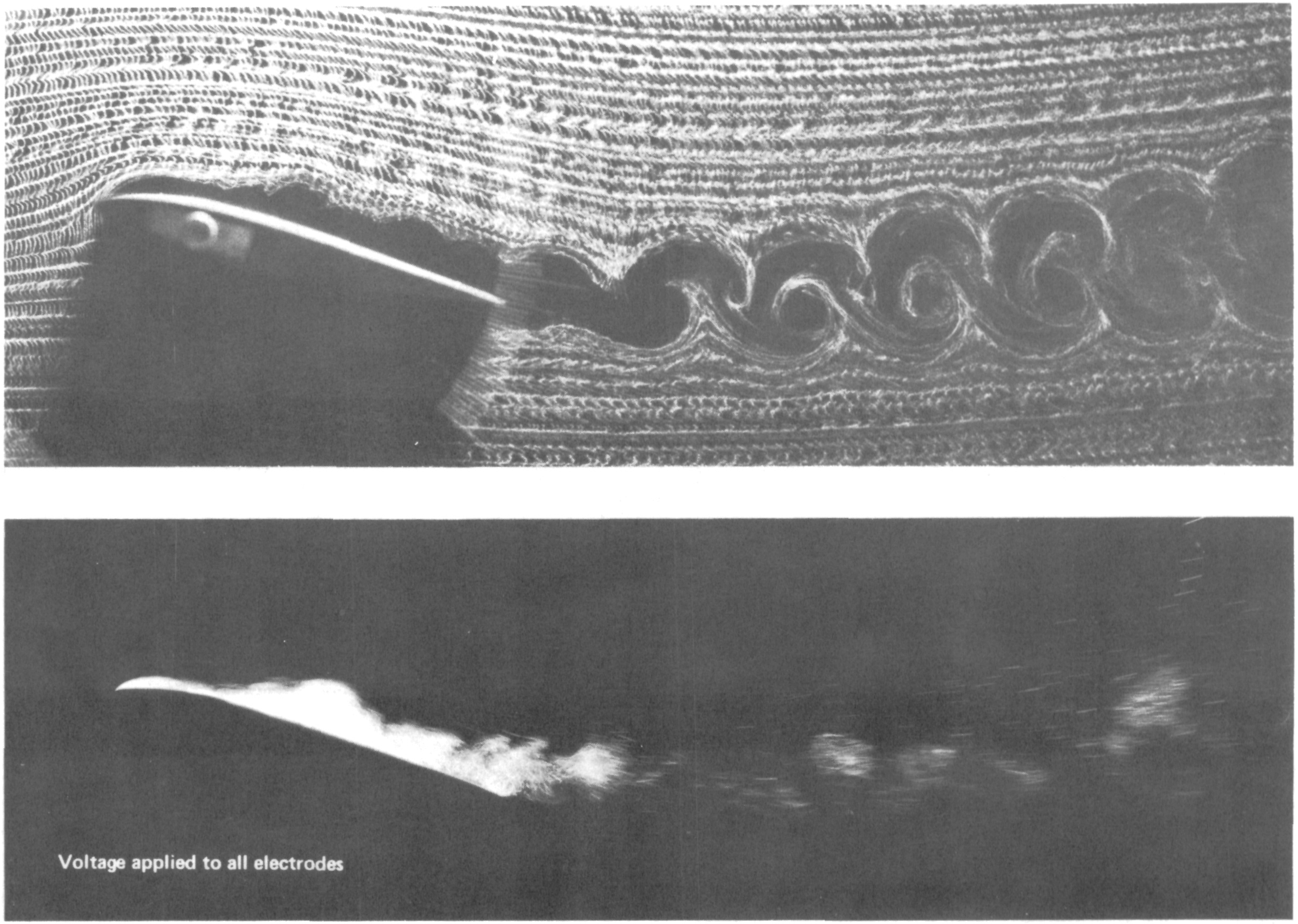

(h) $\omega t = 28°$ ($\alpha = 14.7°$)

Figure 12.- Continued.

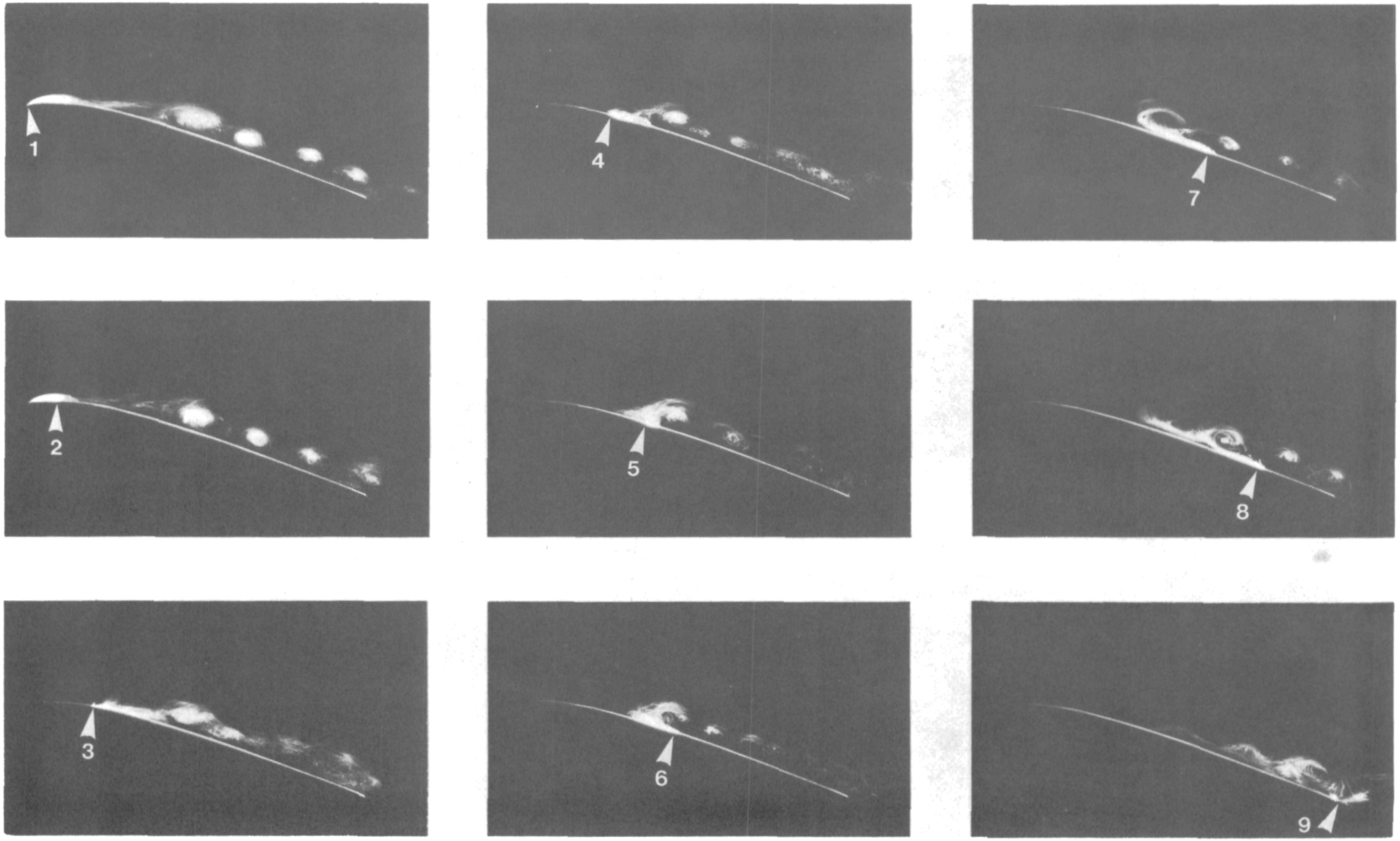

(h) Concluded.

Figure 12.- Continued.

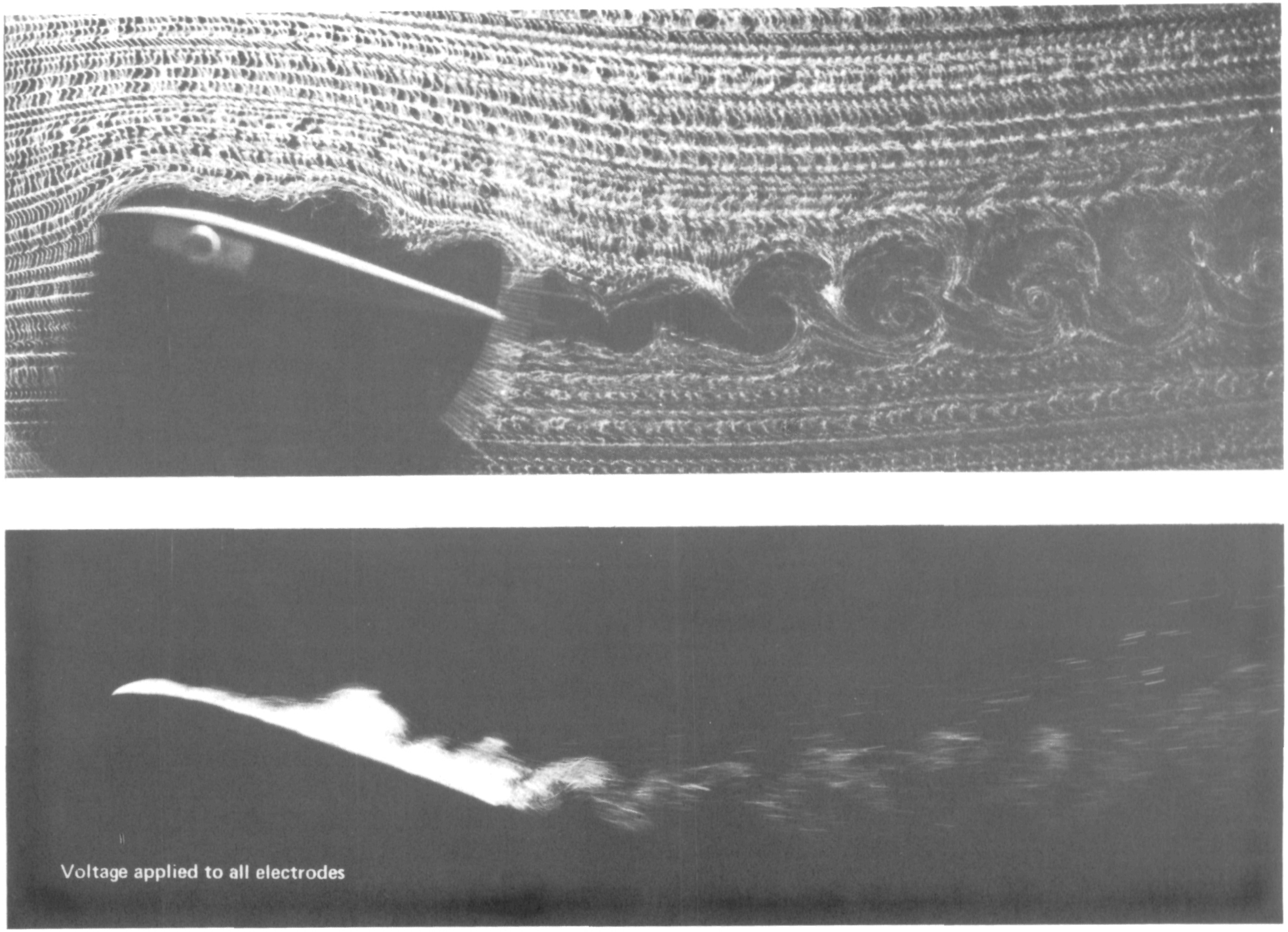

(i) $\omega t = 32°$ ($\alpha = 15.3°$)

Figure 12.- Continued.

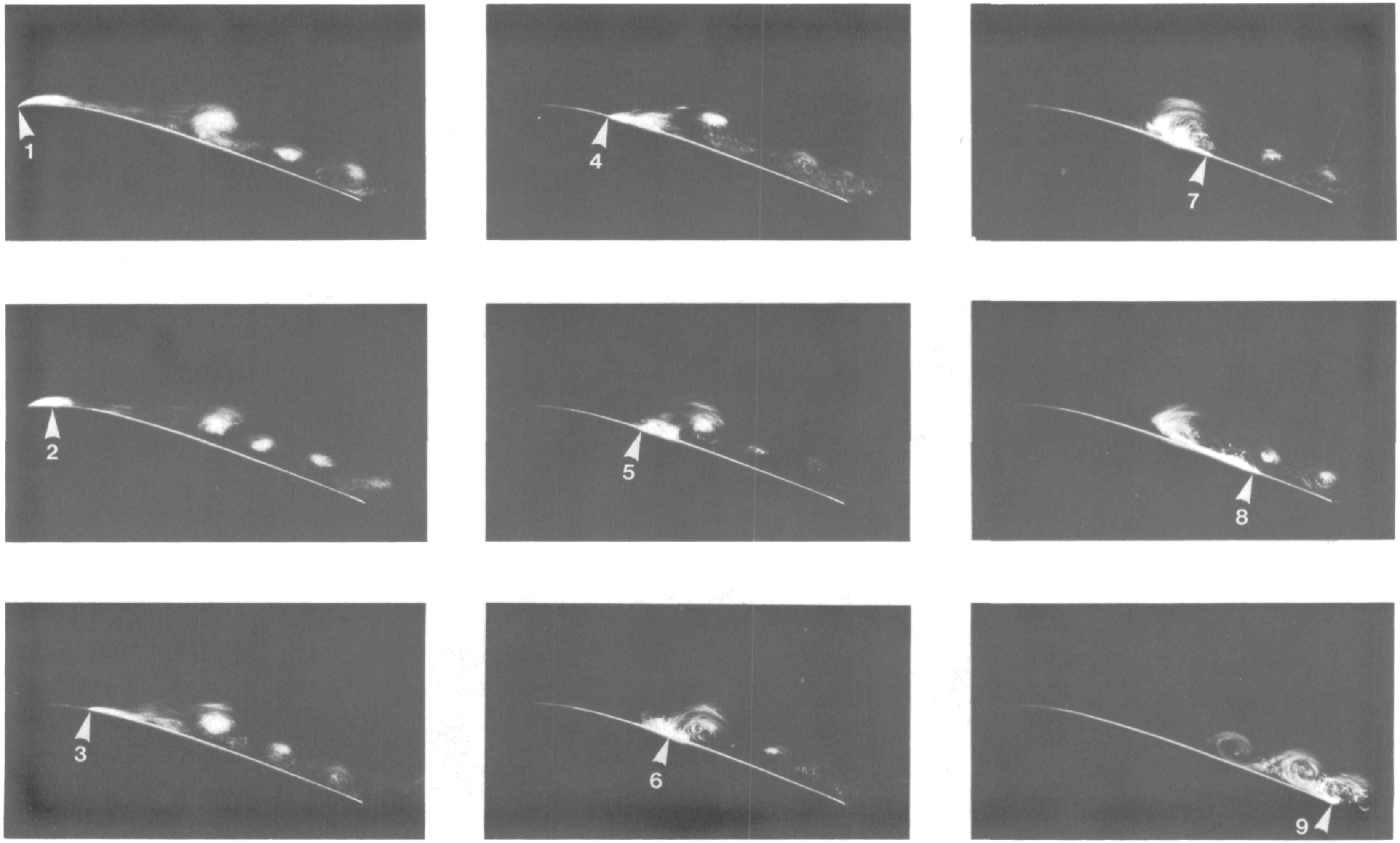

(i) Concluded.

Figure 12.- Continued.

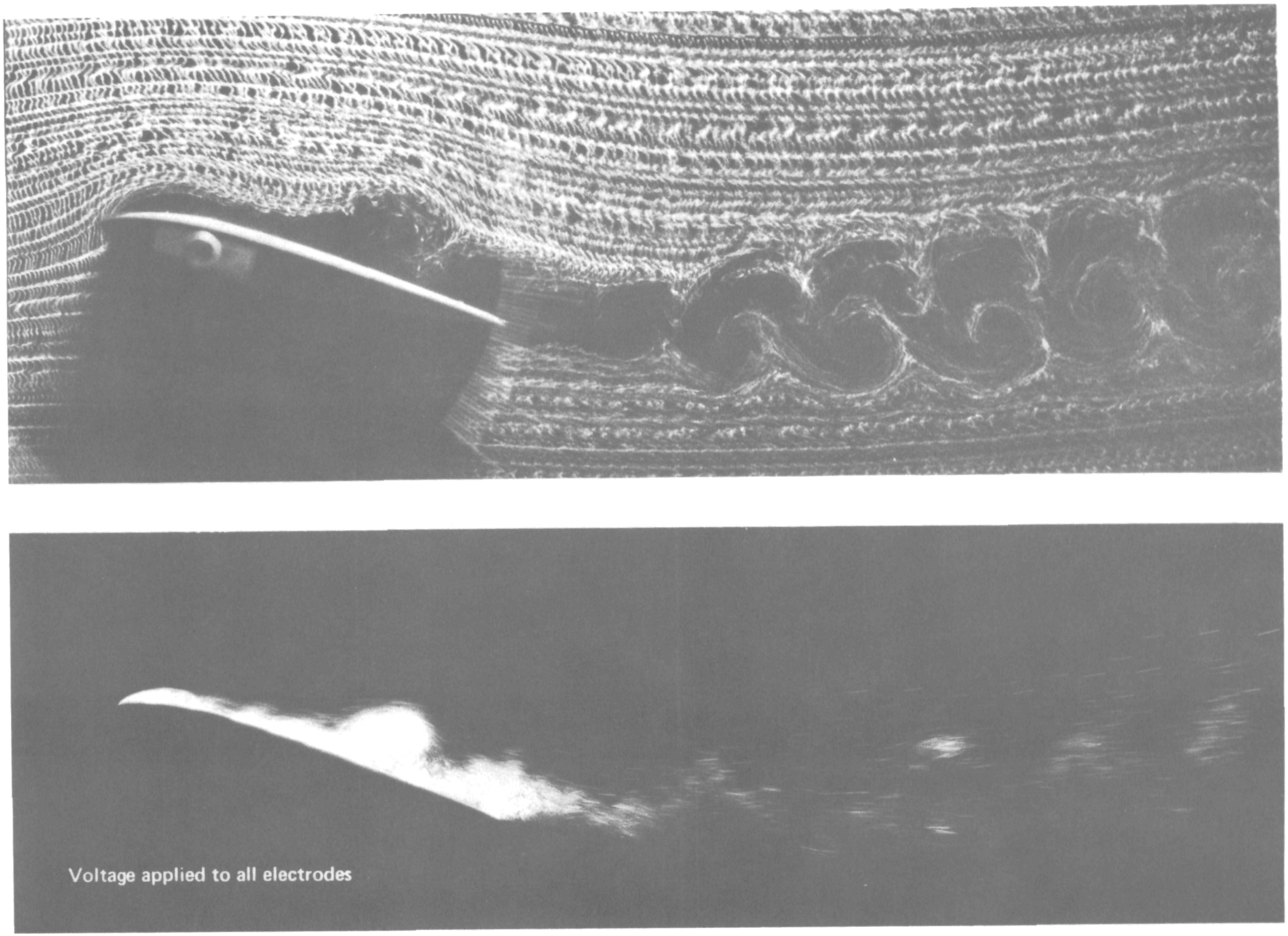

(j) $\omega t = 36°$ ($\alpha = 15.9°$)

Figure 12.- Continued.

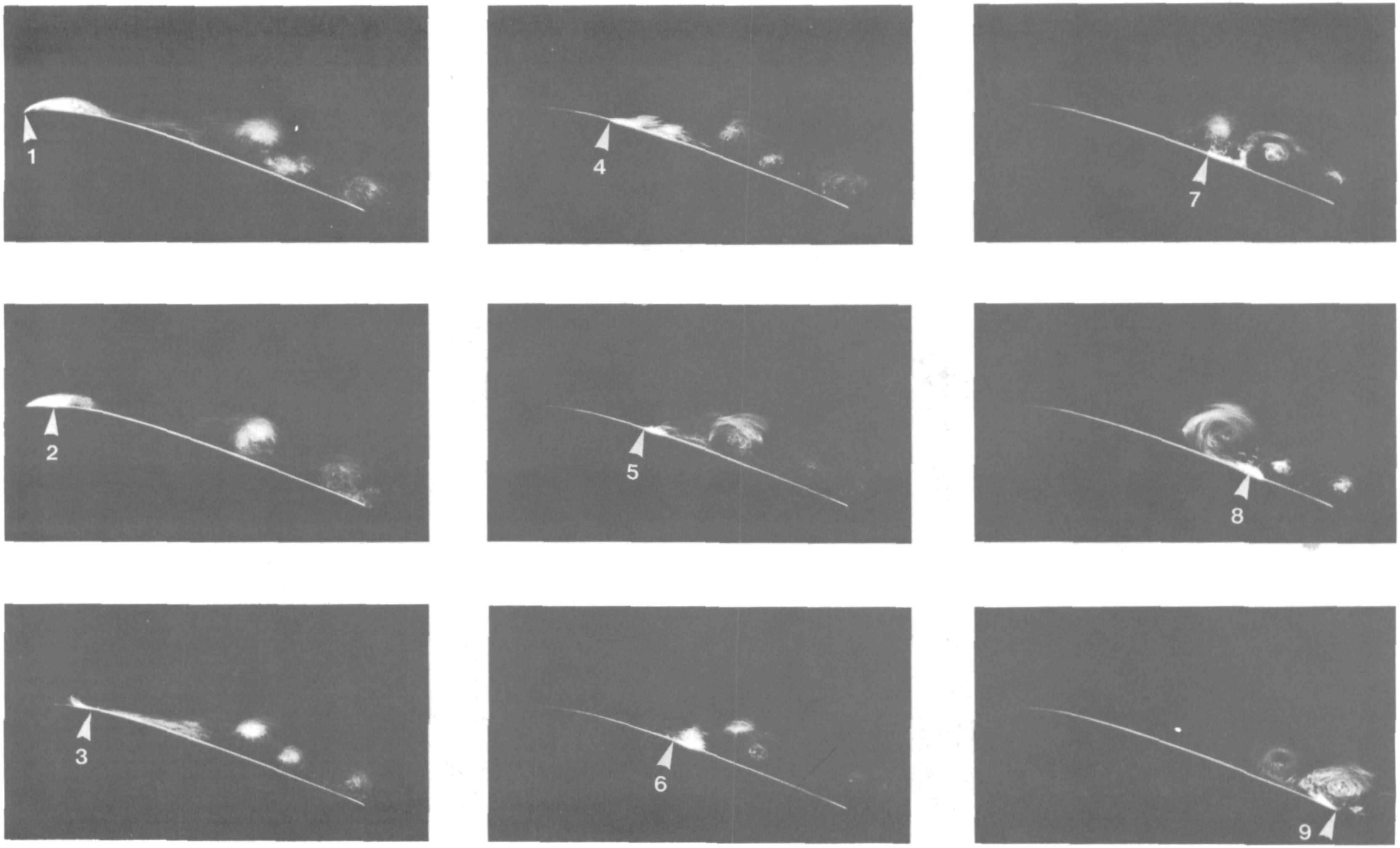

(j) Concluded.

Figure 12.- Concluded.

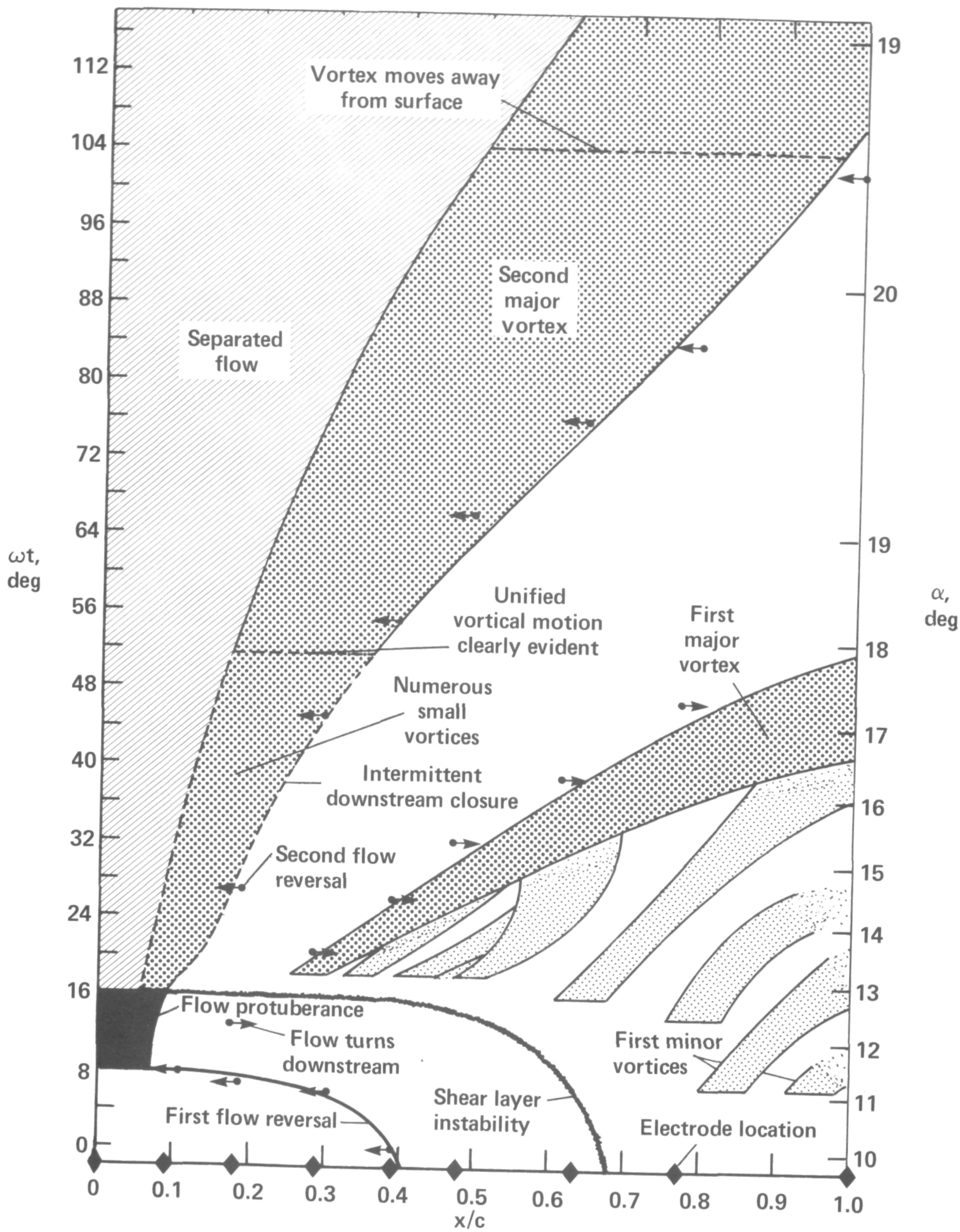

Figure 13.- Chronology of events during stall onset.

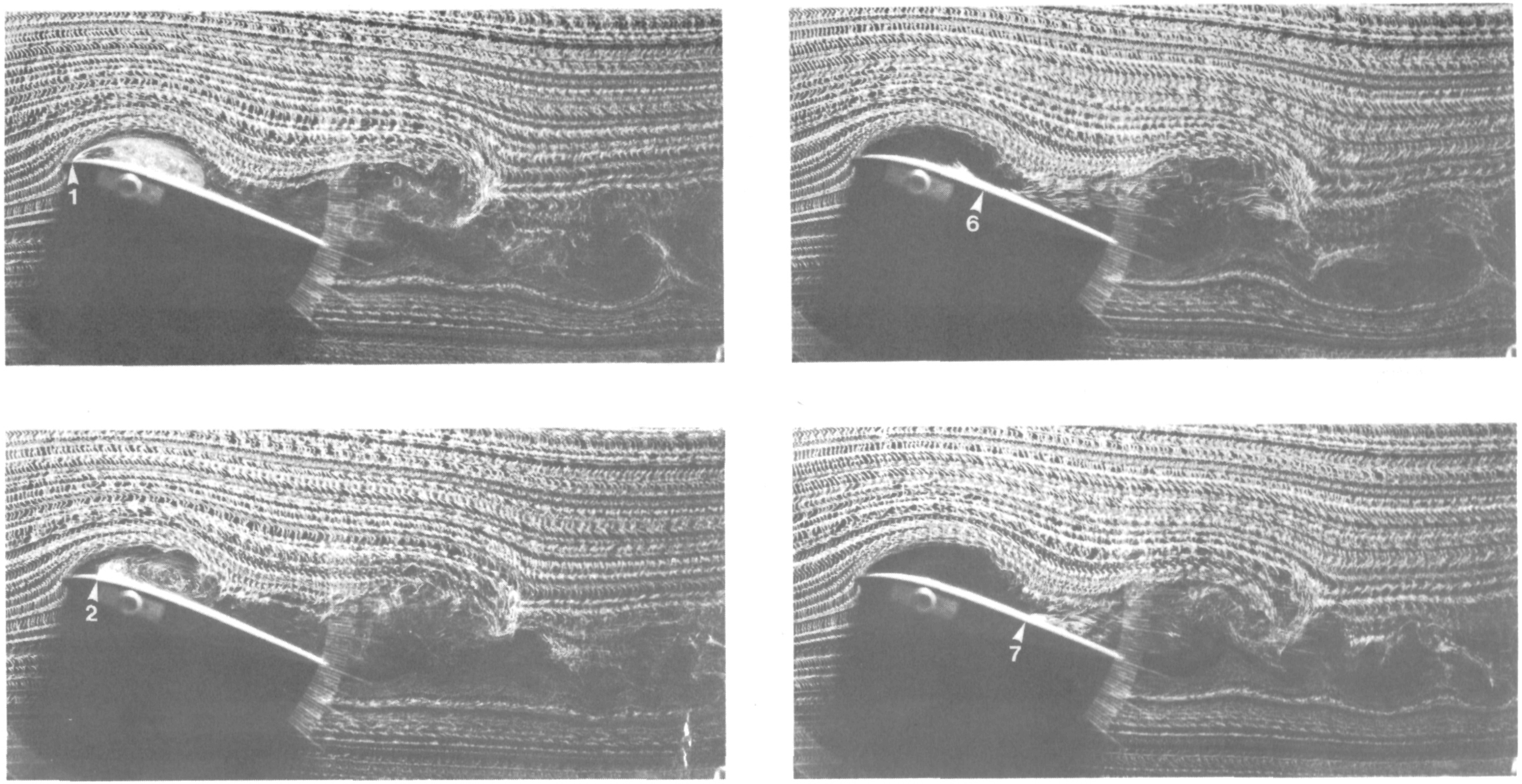

Figure 14.- Free-stream development at $\omega t = 60°$ ($\alpha = 18.7°$) superimposed on paths of particles once located at specific chord locations.

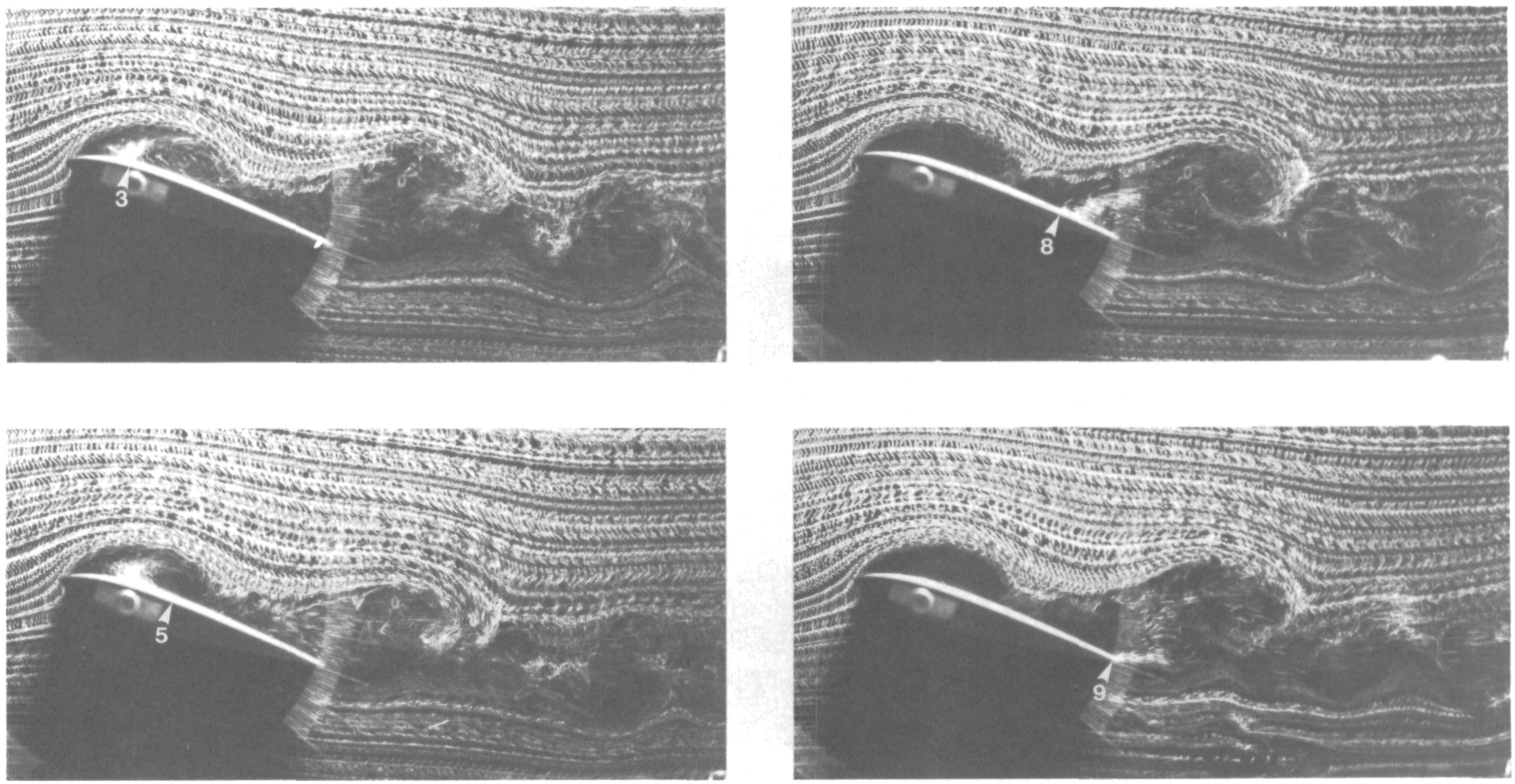

Figure 14.- Concluded.

1. Report No.	2. Government Accession No.	3. Recipient's Catalog No.
NASA TM-78,446		

4. Title and Subtitle	5. Report Date
WATER-TUNNEL EXPERIMENTS ON AN OSCILLATING AIRFOIL AT Re = 21,000	March 1978
	6. Performing Organization Code
7. Author(s)	8. Performing Organization Report No.
Kenneth W. McAlister and Lawrence W. Carr	A-7232
	10. Work Unit No.
9. Performing Organization Name and Address	505-06
Ames Research Center, NASA, and Aeromechanics Laboratory, U.S. Army Aviation R & D Command, Moffett Field, Calif. 94035	11. Contract or Grant No.
	13. Type of Report and Period Covered
12. Sponsoring Agency Name and Address	Technical Memorandum
National Aeronautics and Space Administration Washington, D. C. 20546	14. Sponsoring Agency Code

15. Supplementary Notes

16. Abstract

Flow visualization experiments were performed in a water tunnel on a modified NACA 0012 airfoil undergoing large-amplitude harmonic oscillations in pitch. The motion of the airfoil was governed by $\alpha = 10° + 10° \sin \omega t$ at $k = 0.25$. Hydrogen bubbles were used to (1) create a conveniently striated and well-preserved set of inviscid flow markers; and (2) to expose the succession of events occurring within the viscous domain during the onset of dynamic stall.

Unsteady effects are shown to have an important influence on the progression of flow reversal along the airfoil surface prior to stall. More importantly, a region of reversed flow underlying a free-shear layer is found to momentarily exist over the entire upper surface without any appreciable disturbance of the viscous-inviscid boundary. A flow protuberance, which is not the classical laminar separation bubble that occurs at higher Reynolds numbers, is observed to develop near the leading edge, while minor vortices evolve from an expanding instability of the free-shear layer over the rear portion of the airfoil. The complete breakdown of this shear layer culminates in the successive formation of two dominant vortices.

17. Key Words (Suggested by Author(s))	18. Distribution Statement
Airfoil dynamic stall Vortex shedding Unsteady separation Hydrogen bubble flow visualization	Unlimited STAR Category - 02

19. Security Classif. (of this report)	20. Security Classif. (of this page)	21. No. of Pages	22. Price*
Unclassified	Unclassified	82	$5.00

*For sale by the National Technical Information Service, Springfield, Virginia 22161

NASA-Langley, 1978

National Aeronautics and
Space Administration

Washington, D.C.
20546

Official Business
Penalty for Private Use, $300

THIRD-CLASS BULK RATE

Postage and Fees Paid
National Aeronautics and
Space Administration
NASA-451

U.S. MAIL

[redacted]

S

NASA

POSTMASTER: If Undeliverable (Section 158 Postal Manual) Do Not Return